INCORPORATION OF ALKYLAMINE INTO METAL-ORGANIC FRAMEWORKS FOR CARBON DIOXIDE CAPTURE

A Dissertation

by

HAO LI

Submitted to the Office of Graduate and Professional Studies of
Texas A&M University
in partial fulfillment of the requirements for the degree of

DOCTOR OF PHILOSOPHY

Chair of Committee,	Hong-Cai Zhou
Committee Members,	Marcetta Darensbourg
	James Batteas
	Hong Liang
Head of Department,	Simon North

August 2017

Major Subject: Chemistry

ABSTRACT

The escalating atmospheric CO_2 concentration is one of the most urgent environmental concerns of our age. To effectively capture CO_2, various materials have been studied, such as aqueous alkanolamine solutions, zeolites, activated carbons. However, none of these materials fulfill all the crucial performance parameters for CO_2 capture materials, including but not limited to, high CO_2 selectivity, reasonable regeneration cost, and stability under the operational conditions. Metal-organic frameworks (MOFs) are an emerging class of porous materials constructed from metal-containing nodes and organic linkers. Owing to their high porosity, high surface area, and tunable functionality, MOFs have been investigated extensively to date as promising candidates to be applied in real-world CO_2 capture scenarios. Among them, alkylamine-modified MOFs exhibit significantly improved CO_2 selectivity because of the chemical interaction between the surface functionalities of MOFs and CO_2 molecules.

In most cases, alkylamine molecules are integrated into MOFs via the coordination bonds formed between open metal sites (OMSs) and amine groups. Thus, the alkylamine density as well as the corresponding CO_2 uptake in MOFs are severely restricted by the density of OMSs. To overcome this limit, other approaches to incorporating alkylamine into MOFs are highly desired. Therefore, a new method based on the Brønsted acid-base reaction between MOFs and alkylamine was explored for alkylamine grafting. The pristine MOF utilized is Cr-MIL-101-SO_3H (MIL = Materials of Institute Lavoisier), which has a high density of inherent sulfonic acid groups to interact with amine groups. A systematic optimization of the

experimental conditions involved in alkylamine tethering was conducted to maximize the CO_2 uptakes of the obtained modified MOFs. The study reveals that experimental factors, such as alkylamine structure and solvent species, play an important role in determining the alkylamine loading amount in MOFs and their accompanying CO_2 capacities. This conclusion was further applied in the case of Cr-MIL-101. With judiciously selected alkylamine and solvent species, the CO_2 uptake of the alkylamine-functionalized Cr-MIL-101 was dramatically enhanced compared with the previously reported results. The improvement was rationalized from a thermodynamic perspective.

DEDICATION

To my families and friends

For their love and support

ACKNOWLEDGEMENTS

First, I would like to thank my graduate advisor, Dr. Hong-Cai Zhou for giving me a lot of guidance in my research over the past five years. I would also like to express my appreciation to my committee members, Dr. Marcetta Darensbourg, Dr. James Batteas, and Dr. Hong Liang for providing me valuable advice in my studies and my career plan. Our department members, Ms. Sandy Horton, Ms. Lizzie West and Ms. Carrie Frederiksen, have made my time at Texas A&M University an enjoyable experience.

My fellow lab mates have been incredible to work with. I would especially like to thank my research mentor Dr. Dawei Feng. He led me into the chemistry of metal-organic frameworks and taught me how to think critically and creatively. I would also like to thank Mr. Kecheng Wang who helped me a great deal in project design and experimental skills, Dr. Jihye Park who showed me how to conduct experiments in a carefully organized and efficient way and how to present results professionally, and Dr. Ying-Pin Chen who were always willing to help me and give me encouragement. Many thanks to Mr. Wolfgang Verdegaal, Prof. Dr. Dan Zhao and Dr. Zhigang Hu for the supportive collaboration.

Last but not the least, my families certainly deserve an acknowledgement for their emotional and financial support all these years. Without their companionship and encouragement, I would not have been able to make my way so far. My friends have been so great, especially during those very trying times in my life. I would really like to thank you all so much!

CONTRIBUTORS AND FUNDING SOURCES

Contributors

This work was supervised by a dissertation committee consisting of Professor Hong-Cai Zhou [advisor], Professor Marcetta Darensbourg, Professor James Batteas of the Department of Chemistry [Home Department] and Professor Hong Liang of the Department of Mechanical Engineering [Outside Department].

The Langmuir fitting of the CO_2 adsorption isotherms and the calculation of isosteric heat of CO_2 adsorption in Chapter II were conducted by Mr. Wolfgang Verdegaal. The breakthrough experiments and relevant calculations in Chapter III were performed by Dr. Zhigang Hu and Prof. Dr. Dan Zhao of the Department of Chemical and Biomolecular Engineering in National University of Singapore. All the other work in this dissertation was completed by the student independently.

Funding Sources

This work was supported as part of the Center for Gas Separations Relevant to Clean Energy Technologies, an Energy Frontier Research Center funded by the U.S. Department of Energy, Office of Science, Basic Energy Sciences under Award Number DE-SC0001015, by U.S. Department of Energy, Office of Fossil Energy, National Energy Technology Laboratory under Award Number DE-FE0026472, and by Welch Endowed Chair to HJZ under A-0030. The FE-SEM acquisition was supported by the NSF grant DBI-0116835, the VP for Research Office, and the TX Eng. Exp. Station.

NOMENCLATURE

MOF	metal-organic framework
OMS	open metal site
MIL	Materials of Institute Lavoisier
DMF	*N*, *N*-dimethylformamide
EA	elemental analysis
EDX	energy dispersive X-ray spectroscopy
FTIR	Fourier transform infrared spectroscopy
MeOH	methanol
DCM	dichloromethane
THF	tetrahydrofuran
CH	cyclohexane
MS	mass spectroscopy
NMR	nuclear magnetic resonance
PXRD	powder X-ray diffraction
en	ethylenediamine
DETA	diethylenetriamine
TETA	triethylenetetramine
TEPA	tetraethylenepentamine
PEHA	pentaethylenehexamine
TAEA	tris(2-aminoethyl)amine
$-Q_{st}$	isosteric heat of adsorption

RT	room temperature
DRIFTS	diffuse reflectance infrared Fourier transform spectroscopy
ATR	attenuated total reflectance
SALC	symmetry-adapted linear combination

TABLE OF CONTENTS

LIST OF FIGURES

LIST OF TABLES

LIST OF SCHEMES

CHAPTER I

INTRODUCTION

Human society has developed into a stage where economic prosperity is predominantly dependent on the exploitation of fossil fuels, which are the main energy sources. However, combustion of fossil fuels for power has inevitably brought the emission of large amounts of CO_2 into the atmosphere and led to global warming.[1] Therefore, it is urgent to develop materials that can effectively remove CO_2 from gas mixtures. Current CO_2 scrubbers are mostly aqueous alkanolamine solutions, which suffer from high regeneration energy due to the large portions of water in their composition.[1] This propels the investigation of solid sorbents that have low heat capacities as new materials for CO_2 separation. As a new class of porous solids, MOFs are considered promising materials to perform CO_2 separation. MOFs are primarily utilized as sorbents to achieve CO_2 separation. This is based on differences in interaction between gas species and frameworks and the consequent selective adsorption of target gas. In recent years, a growing number of explorations have also been done to fabricate membranes with MOFs for CO_2 separation, which rely on differences in either the diffusion rates of gas molecules within membranes or their molecular sizes.[2, 3] There are generally four types of CO_2 capture that can be performed using MOFs, namely post-combustion capture, pre-combustion capture, oxy-fuel combustion, and direct capture from air.[1, 4]

1.1 Post-Combustion Capture

The flue gas generated in current power plants is mainly comprised of N_2 (73-77%) and CO_2 (15-16%), with a total pressure of approximately 1 bar. After removal of

SO_x, the flue gas is anticipated to interact with the CO_2 scrubber at temperatures between 40 and 60 °C.[1] Thus, post-combustion capture is aimed at separating CO_2 from N_2 at 40 °C or higher, with CO_2 partial pressure equivalent to 0.15 bar.

In the context of sorbent-based separation, Mg-MOF-74 (CPO-27-Mg) is notable for its high CO_2 uptakes at low pressure under dry conditions (5.28 mmol/g at 40 °C and 0.15 bar), which stem primarily from the high density of open metal sites (OMSs).[5-7] OMSs have strong interaction with CO_2 molecules, but are occupied more preferably by H_2O. This leads to a dramatically decreased CO_2 uptake of Mg-MOF-74 when it is exposed to moisture. Considering the measurable amount of water vapor (5-7%) in flue gas, it is definitely necessary to develop methods to endow MOFs with good selectivity towards CO_2 even in the presence of water.[1] Attempts were made by introducing alkylamines into MOFs to mimic the chemisorption of CO_2 in alkanolamine solutions.[8-10] In 2012, Long and coworkers reported functionalizing Mg_2(dobpdc) (H_4dobpdc = 4,4′-dihydroxy-3,3′-biphenyldicarboxylic acid) with *N*,*N'*-dimethylethylenediamine (mmen) via the coordination bonds formed between the OMSs on Mg_2(dobpdc) and amine groups.[9] For each mmen molecule, one end is coordinated to an unsaturated Mg center, while the other end is dangling in the channel to capture CO_2 in a chemisorptive manner (**Figure 1a**). The high density of amine groups in mmen-Mg_2(dobpdc) results in its good selectivity for CO_2 even in the presence of moisture.[11] Its CO_2 uptake is 3.5 mmol/g at 40 °C and 0.15 bar (**Table 1**). Particularly, a steep step is observed in the low-pressure region of the isotherm. Spectroscopic and diffraction measurements indicate that the unique step in the CO_2 isotherm of mmen-M_2(dobpdc) is attributed to a cooperative CO_2 insertion mechanism that involves a phase-change in the capture process (**Figure 1b**). The CO_2 pressure at which the phase-change occurs can be tuned by altering temperature and the metal species in mmen-M_2(dobpdc). For a specific mmen-M_2(dobpdc), the phase-change pressure would increase from below 0.15 bar to above 1 bar when the temperature is elevated approximately 50 °C.[11] Thus, a large working capacity can be achieved with only a small temperature swing when the adsorption and desorption temperatures are tuned to make the phase-change pressures in the two isotherms right before the adsorption pressure and after the desorption pressure, respectively (**Figure 1c**). Moreover, the identity of the metal species in mmen-M_2(dobpdc) affects the bond strength of mmen-M, and influences the phase-change temperature accordingly. Compared with regular MOF sorbents, the adjustable phase-change step in the CO_2 isotherm of mmen-M_2(dobpdc) help it successfully circumvent the disadvantage of large temperature swings in regeneration (**Figure 1d**), making it extremely favorable for industrial CO_2 capture.

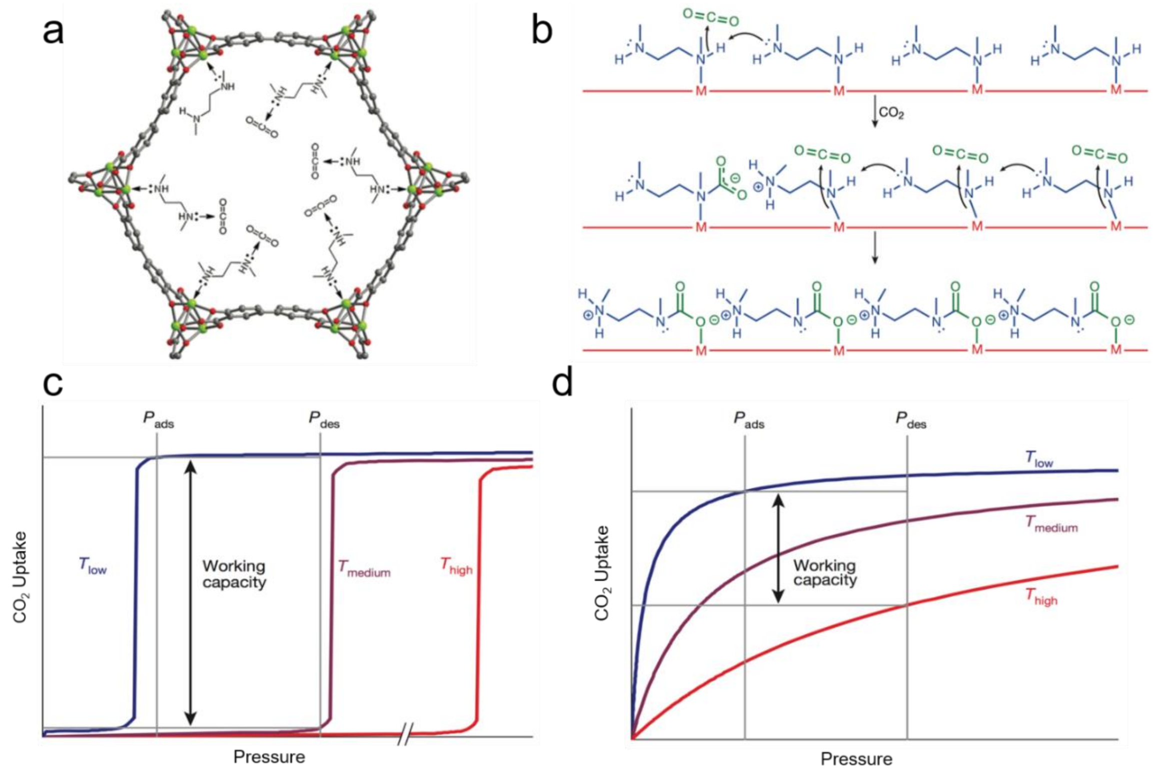

Figure 1. (a) Structure of the amine-appended CO_2 adsorbent mmen-Mg_2(dobpdc). Atom color legend: gray (carbon), red (oxygen), and green (magnesium). Reprinted with permission from ref. [9]. Copyright 2012 American Chemical Society. (b) Illustration of the cooperative insertion mechanism for CO_2 adsorption in mmen-M_2(dobpdc). Comparison of the idealized CO_2 adsorption isotherms of (c) a phase-change adsorbent and (d) a classical microporous adsorbent at varied temperatures. Reprinted with permission from ref. [11]. Copyright 2015 Nature Publishing Group.

Works on integrating other alkylamines into Mg_2(dobpdc) were also reported subsequently, such as dmen-Mg_2(dobpdc) (dmen = *N*,*N*-dimethylethylenediamine),[12] en-Mg_2(dobpdc) (en = ethylenediamine),[13, 14] men-Mg_2(dobpdc) (men = 1-methylethylenediamine),[14] and den-Mg_2(dobpdc) (den = 1,1-dimethylethylenediamine).[14] These works mainly focus tuning the alkylamine structure to optimize the performance of the functionalized MOF in terms of its working capacity, regeneration energy, recyclability, water stability, etc.

Table 1. CO_2 uptakes of selected MOFs. Data are all extracted from CO_2 adsorption isotherms.

Compounds	CO_2 uptake (mmol/g)	Temperature (°C)	Pressure (mbar)	Ref.
Mg-MOF-74	5.28	40	150	6
mmen-Mg_2(dobpdc)	3.5[a]	40	150	11
	3.0[a]	25	0.4	
dmen-Mg_2(dobpdc)	3.1[a]	40	150	12
en-Mg_2(dobpdc)	3.53	40	150	14
	2.83	25	0.39	13
men-Mg_2(dobpdc)	3.6	40	150	14
den-Mg_2(dobpdc)	2.55[a]	40	150	14
Cr-MIL-101-SO_3H-TAEA[b]	2.28	40	150	15
	1.12	20	0.4	
$[Mg_2(dobdc)(N_2H_4)_{1.8}]$	4.9[a]	40	150	16
	3.89	25	0.4	
SIFSIX-3-Zn	2.3[a]	45	150	17
SIFSIX-3-Cu	2.4[a]	45	150	18
	1.24	25	0.4	
SIFSIX-3-Ni	2.2[a]	45	150	19

[a] Estimations are made from CO_2 adsorption isotherms in cases where specific values were not reported.

[b] TAEA = tris(2-aminoethyl)amine.

The foregoing examples all concern alkylamine modification on Mg_2(dobpdc), an expanded variant of Mg-MOF-74, because the sizes of the alkylamines molecules necessitate an isostructure with larger channels to avoid steric hindrance or intermolecular hydrogen bond formation. Nevertheless, amine functionalization was still achieved in Mg-MOF-74 in 2016 by introducing hydrazine into the framework.[16] Consequently, an ultrahigh density of free amine groups (6.01 mmol/g) was attained in the generated new material [$Mg_2(dobdc)(N_2H_4)_{1.8}$] ($H_4dobdc$ = 2,5-dihydroxy-1,4-benzenedicarboxylic acid), which exhibited exceptionally high CO_2 uptakes in both single- or multi-component gas adsorption tests.

Apart from utilizing OMSs in MOFs to tether amines to enhance the affinity towards CO_2, other functional moieties can also be employed to achieve this goal. For example, the Brønsted acidic sites in MOFs, like sulfonic acid groups, can be harnessed to fix amine through a Brønsted acid-base reaction for CO_2 capture.[15] In addition, monodentate hydroxide is also demonstrated to have strong yet reversible interaction with CO_2 in [$Co^{II}Co^{III}(OH)Cl_2(bbta)$] (MAF-X27ox, H_2bbta = 1*H*, 5*H*-benzo(1,2- *d*:4,5-*d'*)bistriazole, MAF = metal azolate framework) via the formation and decomposition of bicarbonate.[20] It enables the framework to selectively adsorb CO_2 from gas mixtures even at humid conditions. Some MOFs, such as SIFSIX-3-M (M = Cu, Zn, Ni), are designed with suitable pore sizes and favorable arrays of inorganic anions to afford enhanced CO_2 binding affinity. Although the interaction between CO_2 and these MOFs are physical interaction, SIFSIX-3-M still exhibit good selectivity for CO_2 at humid conditions.[17-19]

Explorations were also made in the realm of MOF-derived membranes for post-combustion CO_2 capture.[2, 21-24] Compared with synthesizing MOF adsorbents, developing MOF membranes to separate CO_2 from N_2 is more effortful. The main difficulty lies in the comparable kinetic diameters of CO_2 (3.30 Å) and N_2 (3.64 Å), making it challenging to prepare a MOF-derived membrane with simultaneous high permeance and high CO_2/N_2 selectivity.

1.2 Pre-Combustion Capture

Pre-combustion CO_2 capture requires the decarbonation of fuels into H_2 and concomitant CO_2. CO_2 is to be separated from high-pressure (5-40 bar) gas mixtures for the purpose of emitting zero CO_2 during the subsequent combustion step.[1] Because of the evident difference between the kinetic diameters of H_2 (2.89 Å) and CO_2 (3.30 Å),[1] separating the two species based on their distinctive sizes using molecular sieve membranes are mechanistically favorable. However, there exists a long-term bottleneck in the fabrication of membranes with evenly distributed and uniformly sized pores. In 2014, a breakthrough was made by Li, Yang and coworkers in this area.[3] They successfully prepared molecular sieve nanosheets from a layered MOF, $Zn_2(bIm)_4$ (bIm^- = benzimidazolate), by wet ball milling and exfoliation. The apertures on a single-layered $Zn_2(bIm)_4$ sheet are estimated to be 2.9 Å, which would function as channels for small-sized H_2 but also as filters to impede the passage of CO_2. In addition to the good CO_2/H_2 selectivity, the straightforward apertures, constructed from four flat bIm molecules, would also facilitate the fast transport of passing H_2 for a high H_2 permeance. Besides these inherent structural advantages, the temperature under which $Zn_2(bIm)_4$ nanosheets were coated onto α-Al_2O_3 support was fine tuned to minimize ordered restacking between the nanosheets because lamellar restacking would block the pathway for H_2 and significantly affect its permeance. Accordingly, the generated membrane achieves a simultaneous high H_2 permeance (2700 GPU) and high H_2/CO_2 selectivity (291) in the binary CO_2/H_2 separation test.[3] It successfully overcomes the Robeson's upper limit on previous MOF membranes whose separation effects rely upon the different diffusion rates of the gas species.[25-28]

This MOF-derived membrane serves as a good example to illustrate the advantages of membrane-based separation, such as simple separating procedure, energy economy, and high productivity. By contrast, there is scarce experimental research concerning pre-combustion CO_2 capture with MOF sorbents.[29-32] In fact, high CO_2/H_2 selectivity can be achieved in most aforementioned MOFs in post-combustion CO_2 capture section. The restrictions in this area do not exist in CO_2/H_2 separation itself but in the expensive large-scale gasification of fuels. Nevertheless, this field still holds promise if the drawbacks can be overcome.

1.3 Oxy-Fuel Combustion

Oxy-fuel combustion is the ignition of fossil fuels in nearly pure O_2. The flue gas generated is thus almost completely CO_2 after removal of water, rendering a more facile capture step of CO_2.[1] In this approach, the separation target is transformed into producing pure O_2 from air. Traditional cryogenic distillation requires a large energy input, which fails to be a viable solution if CO_2 capture from oxy-fuel combustion is to be implemented extensively.[1] Therefore, alternative strategies that consume less energy but still separate O_2/N_2 effectively is highly desired.

Membrane-based separation would not be feasible in this scenario, because the kinetic diameters of O_2 (3.46 Å) and N_2 (3.64 Å) are extremely close.[1] In the context of sorbent-based separation, selective adsorption of one gas species with an absolute physisorption mechanism is also not applicable, due to the strong resemblance between the physical properties of O_2 and N_2 (such as quadruple moment and polarizability). In contrast, separation that harnesses the different chemisorptive behaviors of the two gases would be very effective. Because O_2 has a high propensity to accept electrons from redox-active metal sites, while N_2 is not endowed with such a feature.[1] Much progress has been made in this aspect to date.

Cr^{2+} and Fe^{2+} are metal species with relatively strong reducing ability. With these unsaturated redox-active metal centers, $Cr_3(btc)_2$ (H_3btc = 1,3,5-benzenetricarboxylic acid), Cr-BTT (H_3BTT = 1,3,5-Tris(2*H*-tetrazol-5-yl)benzene), and $Fe_2(dobdc)$ have the tendency to donate electrons to O_2 to have strong O_2 affinity and marked O_2/N_2 selectivity.[33-35] However, Cr^{II}-MOFs display gradual decreases in O_2 capacity over multiple cycles,[34, 35] while $Fe_2(dobdc)$ would lose its recyclability at temperatures above 222 K for irreversible oxidation.[33] Subsequently, more explorations were made with Co^{II}-MOFs. Unlike previous Co-MOFs built with weak-field carboxylate-terminated ligands, strong-field N-donor ligands are adopted in the cases of Co-BTTri (H_3BTTri = 1,3,5-tri(1*H*-1,2,3-triazol-5-yl)benzene) and Co-BDTriP ($H_3BDTriP$ = 5,5'-(5-(1*H*-pyrazol-4-yl)-1,3-phenylene)bis(1*H*-1,2,3-triazole)) (**Figure 2a** and **2b**).[36] The σ-orbitals in $BTTri^{3-}$ and $BDTriP^{3-}$ are higher in energy compared with those in weak-field ligands. Upon their formation of molecular orbitals with d orbitals from the metal, e_g* orbitals would be lifted to a higher energy level, making the electrons in these elevated e_g* orbitals have a stronger inclination to transfer to O_2 (**Figure 3**). This gives rise to stronger O_2 binding and a higher O_2/N_2 selectivity in MOFs. Consequently, Co-BTTri has an O_2 loading of 3.3 mmol/g at 0.21 bar and 195 K, with an IAST (IAST = ideal adsorbed solution theory) selectivity of

41 at the same temperature (**Figure 2c**).[36] Its isostructure, Co-BDTriP, in which one triazolate terminal is replaced by a more electron-donating pyrazolate group, exhibits greater O_2/N_2 selectivities at temperatures between 195 and 240 K (**Figure 2d**). This further demonstrates the fact that a coordination environment created by stronger-field ligands around the metal center would lead to a MOF with higher O_2 affinity. In addition to the enhanced selectivities, Co^{II}-MOFs also have good recyclability and water stability, which are also important criteria to consider for the design of future O_2 adsorbents.

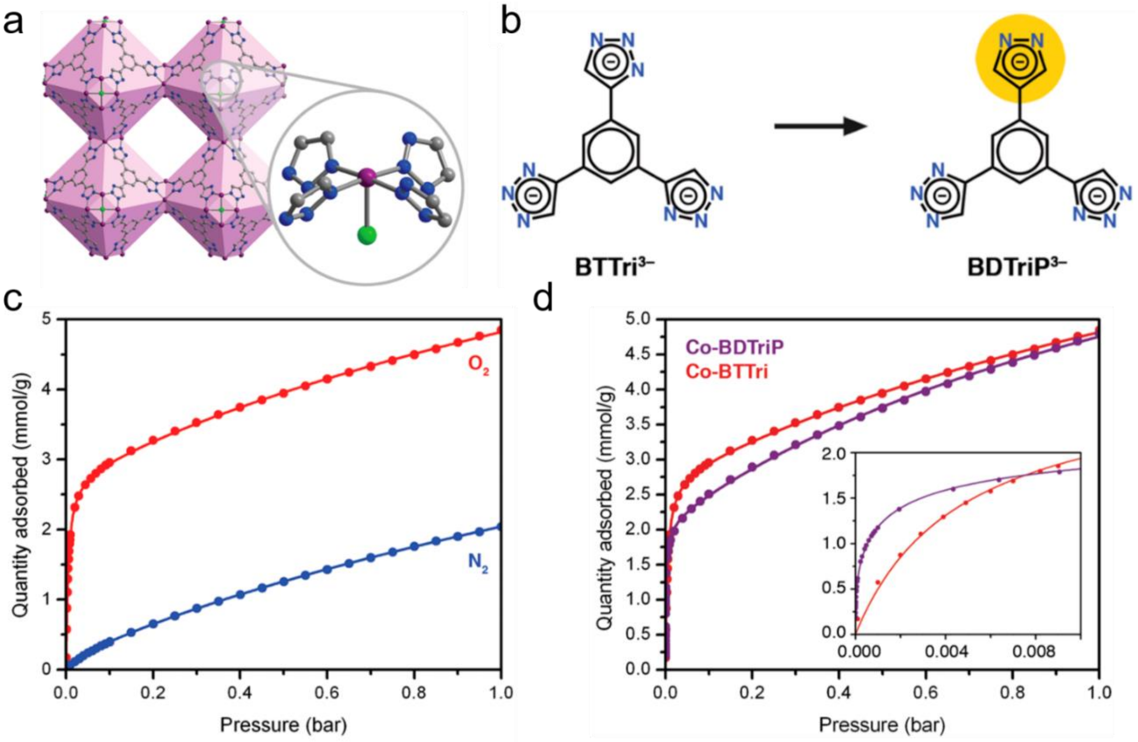

Figure 2. (a) Structure of Co-BTTri. Atom color legend: purple (cobalt), gray (carbon), blue (nitrogen), green (chlorine). (b) Molecular structures of $BTTri^{3-}$ and $BDTriP^{3-}$. (c) O_2 and N_2 adsorption isotherms of Co-BTTri at 195 K. Solid lines represent corresponding dual-site Langmuir fit curves. (d) O_2 adsorption isotherms of Co-BDTriP and Co-BTTri at 195 K. Solid lines represent corresponding Langmuir fits. Reprinted with permission from ref. [36]. Copyright 2016 American Chemical Society.

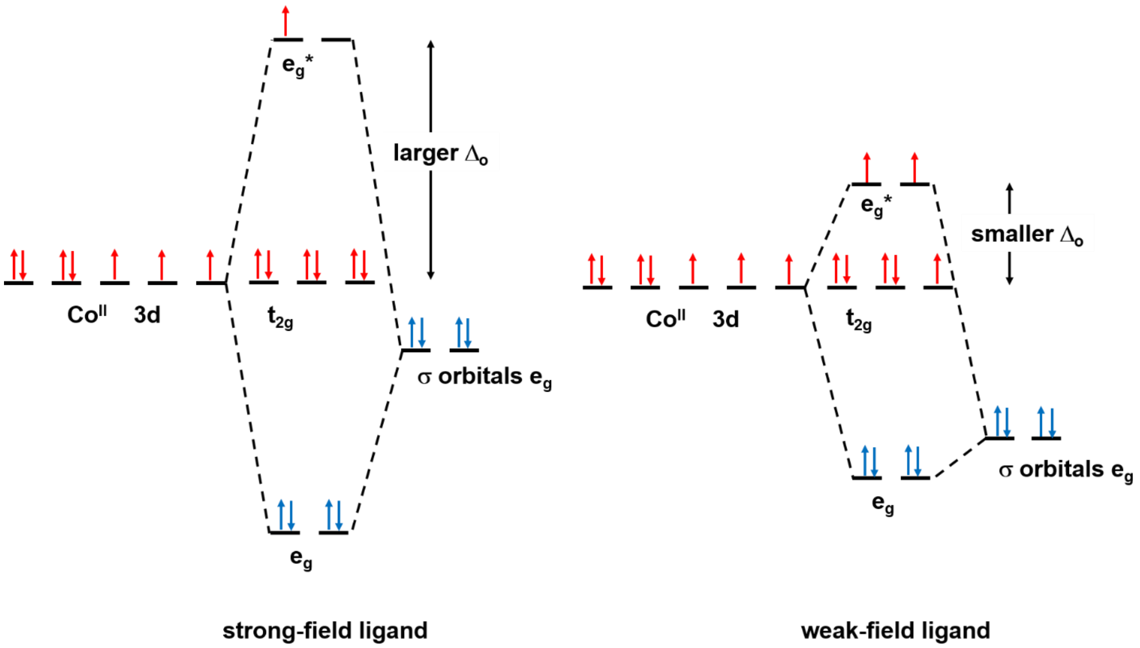

Figure 3. σ-bond molecular orbital diagrams of Co^{2+} coordinated by strong- (left) and weak-field ligands (right) in O_h symmetry. The coordination sphere around Co^{2+} is simplified into O_h symmetry for easy illustration. Only σ-orbitals of SALCs (SALC = symmetry-adapted linear combination) with e_g symmetry are shown for clarity.

1.4 Direct Capture from Air

All the previous scenarios are CO_2 capture from stationary point sources, which are intended for slowing the increasing rate of atmospheric CO_2 concentration. To scavenge the CO_2 that has already been released into air, a concept called "negative carbon technology" was recently put forward, which necessitates the practice of direct CO_2 capture from air (or direct air capture, DAC).[4] In addition, DAC can also contribute to maintaining a low CO_2 level in submarines or spacecraft, so that a habitable environment can be guaranteed in these confined spaces.[4] The current atmospheric CO_2 level is 400 ppm, so the operational condition of DAC is 0.4 mbar and 25 °C.[1, 4] The methods to endow MOFs with the ability to scavenge CO_2 at extremely low pressure are similar to those discussed in the section of post-combustion capture, including but not limited to, incorporating functional groups that have strong yet reversible chemical interaction with CO_2, and rational tailoring of the size and shape of internal pores for enhanced physical interaction between MOFs and CO_2. The DAC performance of some notable MOFs is summarized in **Table 1**. As for DAC with MOF-derived membranes, few examples have been reported. The similar molecular sizes of CO_2, N_2 and O_2, extremely low atmospheric CO_2 concentration, and complex air composition all make this research area very challenging.

Considering the current status in the development of MOF materials for CO_2 separation, this work focuses on the study of alkylamine-functionalized MOFs as adsorbents for post-combustion CO_2 capture and direct CO_2 capture from air.

CHAPTER II

INCORPORATION OF ALKYLAMINE INTO METAL-ORGANIC FRAMEWORKS THROUGH A BRØNSTED ACID-BASE REACTION FOR CO_2 CAPTURE [*]

2.1 Introduction

Carbon capture has become increasingly important for the pressing need to curb the climbing concentration of atmospheric CO_2, which could cause severe global warming.[37, 38] It is also necessary to capture CO_2 directly from air for some applications, such as the removal of CO_2 from in the controlled atmospheres of submarines or aircraft.[39, 40] Tremendous effort has been devoted to studying various materials for CO_2 capture.[1, 39, 41-48] Among them, metal-organic frameworks (MOFs) are considered to be promising candidates for their high porosity, tunable structure, and low heat capacity.[5, 17, 18, 49-59] In most cases, CO_2 is physically adsorbed in MOFs.[60-62] This leads to very low selectivity of CO_2 over the coexisting species in flue gas or air with higher polarity, such as H_2O,[1, 63, 64] which severely restrict the CO_2 adsorption capacity of MOFs under moist conditions. The problem can be solved by introducing alkylamines into the frameworks,[9-13, 65] because the amine groups can specifically chemisorb CO_2 from gas mixtures through reversible chemical reactions.[1] So far, alkylamines are mainly incorporated via the coordination bonds between amine groups and open metal sites (OMSs).[9, 11-13, 65, 66] Although some alkylamine integrated MOFs with high CO_2 uptakes have been obtained through this

---

[*] Reprinted with permission from ref. 15. H. Li, K. Wang, D. Feng, Y.-P. Chen, W. Verdegaal and H.-C. Zhou, Incorporation of Alkylamine into Metal–Organic Frameworks through a Brønsted Acid–Base Reaction for CO2 Capture. *ChemSusChem*, 2016, **9**, 2832-2840. Copyright 2016 John Wiley and Sons.

approach, intrinsic disadvantages of this method still exist. Firstly, high density of OMSs in MOFs is greatly desired in this method to achieve a large alkylamine loading amount, which is a prerequisite for high CO_2 uptake in MOFs. However, the OMS density in a MOF is restricted by the inherent structures of inorganic nodes and organic linkers. They inevitably set an upper limit on alkylamine density and corresponding CO_2 uptake in MOFs. Secondly, the method is only applicable to MOFs with OMSs. Thus it excludes many MOFs,[67-69] covalent organic frameworks (COFs),[70] and porous polymer networks (PPNs),[42, 71] which have no OMSs but retain high chemical stability to probably survive in alkylamine tethering conditions. Therefore, introducing other amine grafting sites can not only overcome the upper limit of alkylamine density in MOFs, but also expand the range of material candidates for amine incorporation, which is of great importance to advance the development of CO_2 adsorbents.

Herein, by employing the Brønsted acid sites in a highly stable MOF, Cr-MIL-101-SO_3H,[72, 73] we intend to integrated alkylamine into this mesoporous adsorbent through a Brønsted acid-base interaction. The experimental conditions in alkylamine tethering process are also to be investigated systematically to optimize the CO_2 capture performance of the resulting material.

2.2 Experimental Section

2.2.1 Chemicals

Chromium (III) nitrate nonahydrate ($Cr(NO_3)_3 \cdot 9H_2O$), monosodium 2-sulfoterephthalic acid (H_2BDC-SO_3Na), hydrofluoric acid (HF), *N*,*N*-dimethylformamide (DMF), hydrochloric acid (HCl), methanol (MeOH), acetone, cyclohexane (CH), tetrahydrofuran (THF), dichloromethane (DCM), ethylenediamine (en), diethylenetriamine (DETA), triethylenetetramine (TETA), tetraethylenepentamine (TEPA), pentaethylenehexamine (PEHA), tris(2-aminoethyl)amine (TAEA) were purchased from VWR. All commercial chemicals were used without further purification unless otherwise mentioned.

2.2.2 Instruments

Powder X-ray diffraction (PXRD) was carried out with a BRUKER D8-Focus Bragg-Brentano X-ray Powder Diffractometer equipped with a Cu sealed tube (λ = 1.54178 Å) at 40 kV and 40 mA. Fourier transform infrared (FTIR) data were recorded on a SHIMADZU IR Affinity-1 instrument with diffuse reflectance attachment or attenuated total reflectance (ATR) attachment. Images and analyses of SEM/EDS were taken by FEI Quanta 600 FE-SEM. The Quanta 600 FEG is a field emission scanning electron microscope capable of generating and collecting high-resolution and low-vacuum images. It is equipped with a motorized x-y-z-tilt-rotate stage, providing the following movements: x = y = 150 mm (motorized); z = 65 mm (motorized); Tilt +70 degrees to –5 degrees (motorized); Source: Field emission gun assembly with Schottky emitter source. Voltage: 200 V to 30 kV. Beam Current: >100 nA. Equipment associated with the Quanta 600 includes: conventional Everhart-Thornley detector, back-scattered electron detector, IR-CCD chamber camera, Oxford EDS system equipped with X-ray mapping and digital imaging, HKL/Oxford EBSD system incl. geological phase database for phase ID, Gatan panchromatic cathodoluminescence detector with RGB filters and a Zyvex S100 nanomanipulator. N_2 and CO_2 adsorption-desorption isotherms were measured using a Micrometritics ASAP 2020 system at different temperatures.

2.2.3 Preparation of Cr-MIL-101-SO_3H

A mixture of $Cr(NO_3)_3.9H_2O$ (2.00g, 5 mmol), H_2BDC-SO_3Na (2.70g, 10 mmol), deionized water (30 mL), and HF (48-51 wt%, 0.3 mL) was heated at 463 K for 24 h.[72] The as-synthesized solid was washed with deionized water, DMF and acetone in sequence and was dried in air. The obtained green crystalline powder of Cr-MIL-101-SO_3Na(H) was post-synthetically acidified in 60 mL dilute HCl solution (0.08 M, the solution was prepared with 2 mL concentrated HCl, 150 mL deionized water and 150 mL MeOH) at 80 °C for 12h to give Cr-MIL-101-SO_3H.[73] The resultant green solid was washed ionized water and acetone in sequence and finally dried overnight at 130 °C under vacuum prior to further use.

2.2.4 Procedure of Tethering Alkylamine onto Cr-MIL-101-SO_3H

A sample of fully activated Cr-MIL-101-SO_3H (100 mg, 0.108 mmol) was added to a 40 mL vial full of anhydrous solution containing 2 equiv. alkylamine (en, DETA, TETA, TEPA, PEHA or TAEA).that has already been dispersed The aforementioned solvent was newly collected from solvent still (CH, THF, DCM or MeOH). The suspension was stirred at RT for 5 min before alkylamine modified Cr-MIL-101-SO_3H was separated from the solution. The solid was washed with anhydrous cyclohexane for three times, desiccated under Schlenk line and activated at 80 °C under vacuum before gas uptake measurements were taken. Note: 1 equiv. refers to the amount of a certain alkylamine if we assume all the sulfonic acid groups in Cr-MIL-101-SO_3H are to be consumed in a 1:1 ratio reaction with alkylamine. The volume of 1 equiv. respective alkylamine was calculated and listed in **Table 2**.

Table 2. Summary of the volume of 1 equiv. alkylamine for amine modification on Cr-MIL-101-SO_3H sample.

Alkylamine	Cr-MIL-101-SO_3H	1 equiv. alkylamine
en	100 mg, 0.108 mmol	21.7 uL
DETA	100 mg, 0.108 mmol	35.1 uL
TETA	100 mg, 0.108 mmol	48.4 uL
TEPA	100 mg, 0.108 mmol	61.9 uL
PEHA	100 mg, 0.108 mmol	79.5 uL
TAEA	100 mg, 0.108 mmol	48.6 uL

Note: 1 equiv. refers to the amount of a certain alkylamine if we assume all the sulfonic acid groups in Cr-MIL-101-SO_3H are to be consumed in a 1:1 ratio reaction with alkylamine.

2.2.5 Gas Sorption Measurement of Alkylamine-Modified Cr-MIL-101-SO_3H

The gas sorption isotherms were collected using Micrometritics ASAP 2020 system. N_2 uptakes were measured at 77 K, while CO_2 uptakes were measured at 0 °C, 20 °C, and 40 °C.

2.2.6 PXRD Measurement of Alkylamine-Modified Cr-MIL-101-SO_3H

The PXRD patterns of the samples were collected using a BRUKER D8-Focus Bragg-Brentano X-ray Powder Diffractometer equipped with a Cu sealed tube (λ = 1.54178 Å) at 40 kV and 40 mA. The ranges of 2θ are all set to be 2-35 degree.

2.2.7 EDX Measurement of Alkylamine-Modified Cr-MIL-101-SO_3H

The sample was first desiccated to remove moisture or solvent residues. After that, it is finely ground before being applied on a conductive tape which is adhered to the

EDX sample holder. After the sample was placed into the SEM/EDX instrument, the inner pressure was decreased below 10^{-6} torr before measurements were conducted. The scanning areas were all set to be approximately 40×40 μm^2 to detect the element species.

2.2.8 FTIR Measurement

The liquid TAEA was desiccated with molecular sieves at RT overnight to make anhydrous TAEA. The FTIR spectrum of the resulting TAEA was collected using a SHIMADZU IR Affinity-1 instrument with ATR attachment. The FTIR spectra of pristine Cr-MIL-101-SO_3H and Cr-MIL-101-SO_3H-TAEA were taken with the same equipment but with a diffuse reflectance attachment.

2.2.9 Calculation of Isosteric Heat of CO_2 Adsorption[*]

Isosteric heat of CO_2 adsorption of Cr-MIL-101-SO_3H-TAEA was calculated based on the CO_2 uptake data collected at 0 °C, 20 °C and 40 °C with a triple-site Langmuir model. The temperature dependence was introduced in the fit through the Arrhenius approach.

The used Langmuir model (i = A, B, C):

$$q = \sum_i q_{sat,i} \frac{b_i p}{1 + b_i p} \qquad \textbf{(Equation 1)}$$

$$b_i = b_{0,i} \exp\left(\frac{E_i}{RT}\right) \qquad \textbf{(Equation 2)}$$

---

[*] The Langmuir fitting of the CO_2 adsorption isotherms and the calculation of isosteric heat of CO_2 adsorption were conducted by Mr. Wolfgang Verdegaal.

We used the analytical function of the triple-site Langmuir fit and solved the Clausius-Clapeyron Equation which describes the isosteric heat of adsorption as partial gradient of the logarithmic pressure over the temperature at constant adsorption loading.

$$Q_{st} = RT^2 \left(\frac{\partial \ln p}{\partial T} \right)_q \qquad \textbf{(Equation 3)}$$

2.3 Results and Discussion

2.3.1 Synthesis and Characterization of Cr-MIL-101-SO_3H

Due to the strong electron donating ability of N atoms in amine groups, alkylamine is not only a good ligand to coordinate onto OMSs, but also a strong base, which is able to form ionic bonds with acid. Therefore, an alternative approach to introducing alkylamine into MOFs is to utilize Brønsted acid sites. Since Brønsted acid groups can be integrated into many types of organic linkers conveniently,[74, 75] this approach can enormously increase the number of MOF candidates for CO_2 capture. In order to test our hypothesis, we chose Cr-MIL-101-SO_3H (**Figure 4-5**) as the pristine MOF to fix alkylamines for the following reasons. Firstly, Cr-MIL-101 is well-known for its ultrastability under harsh environments,[76] which allows the framework to remain intact in alkylamine solution during the postsynthetic treatment. Secondly, as a strong Brønsted acid, sulfonic acid group can easily form ionic bonds with amine groups, by which alkylamines can also be immobilized in MOFs. In Cr-MIL-101-SO_3H, the density of sulfonic acid groups is 3.25 mmol/g, which is even higher than that of OMSs (2.17 mmol/g).[72] This provides Cr-MIL-101-SO_3H with the potential to tether more alkylamine molecules than Cr-MIL-101 and therefore have a higher CO_2 uptake. Thirdly, Cr-MIL-

101-SO_3H is mesoporous.[76] The favorable pore volume permits the incorporation of large alkylamines with more amine groups in a single molecule and thus promises a higher amine group density than that of MOFs only modified with small alkylamines. Last but not the least, the organic ligand to synthesize Cr-MIL-101-SO_3H, namely monosodium 2-sulfoterephthalic acid (BDC-SO_3Na(H)), is commercially available. This is extremely important because large-scale production of the absorbent is definitely necessary for industrial application. The synthesized Cr-MIL-101-SO_3H exhibit good porosity and crystallinity (**Figure 6-7**). Based on the EDX measurement, most Na ions in the framework were replaced by protons (**Figure 8-13** and **Table 3-6**), which ensures sufficient sulfonic acid groups in Cr-MIL-101-SO_3H to interact with alkylamine molecules.

Figure 4. Appearance of Cr-MIL-101-SO_3H.

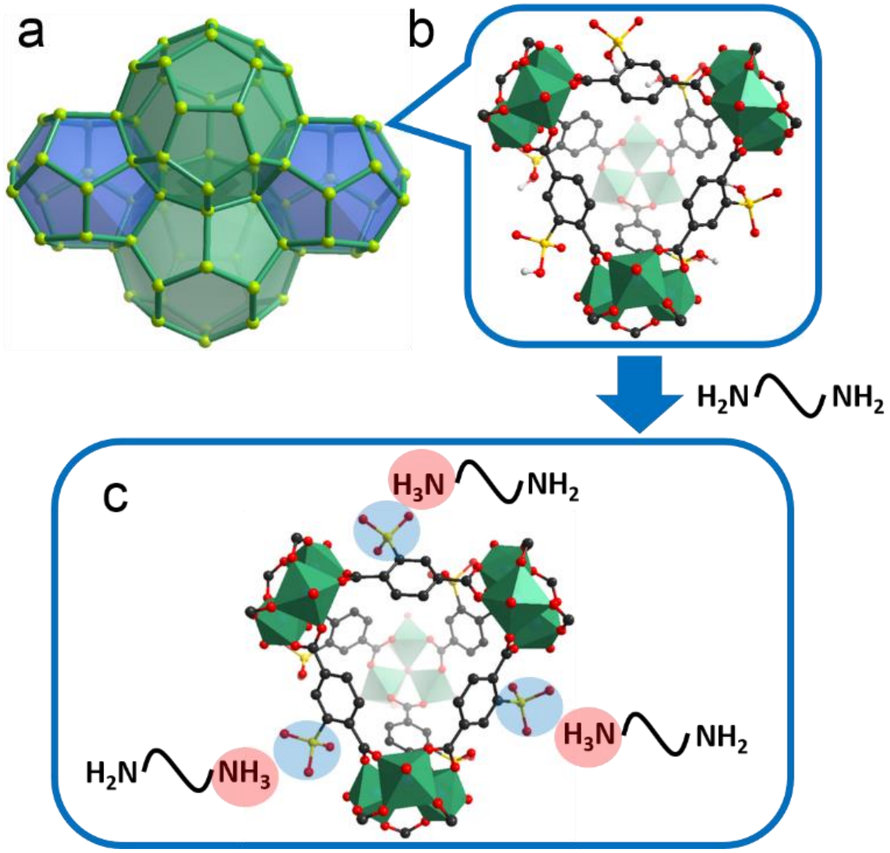

Figure 5. (a) Cr-MIL-101-SO_3H topology. Each lime ball represents a supertetrahedron unit, and green and blue polyhedra represent two types of cages. (b) Supertetrahedron unit in Cr-MIL-101-SO_3H. Atom color legend: black (carbon), grey (hydrogen), yellow (sulfur), red (oxygen). (c) Illustration of electrostatic interaction between sulfonate groups and ammonium groups after proton transfer from sulfonic acid groups to amine groups.

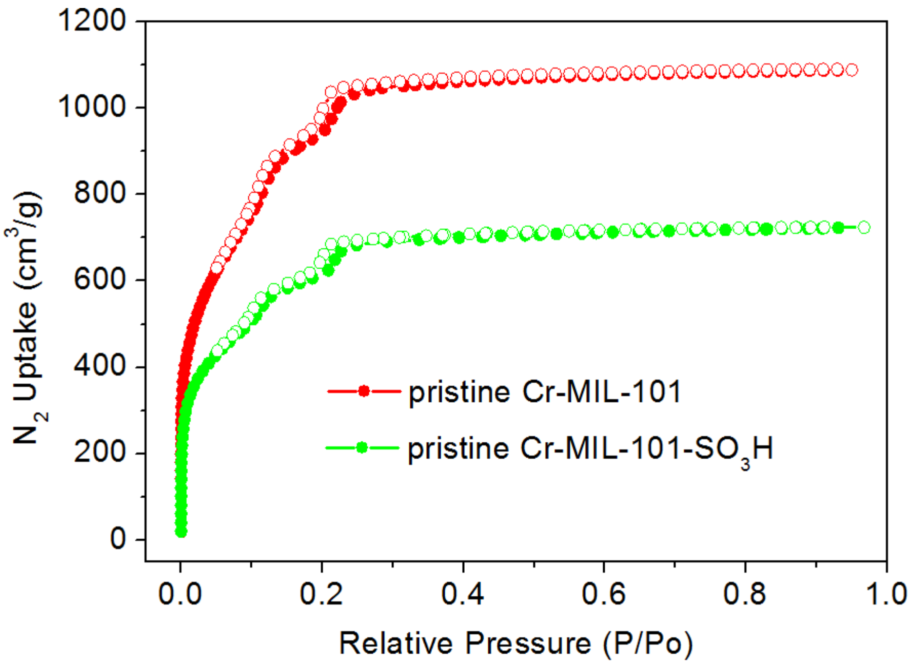

Figure 6. N_2 adsorption/desorption isotherms at 77K of Cr-MIL-101-SO_3H and Cr-MIL-101 samples.

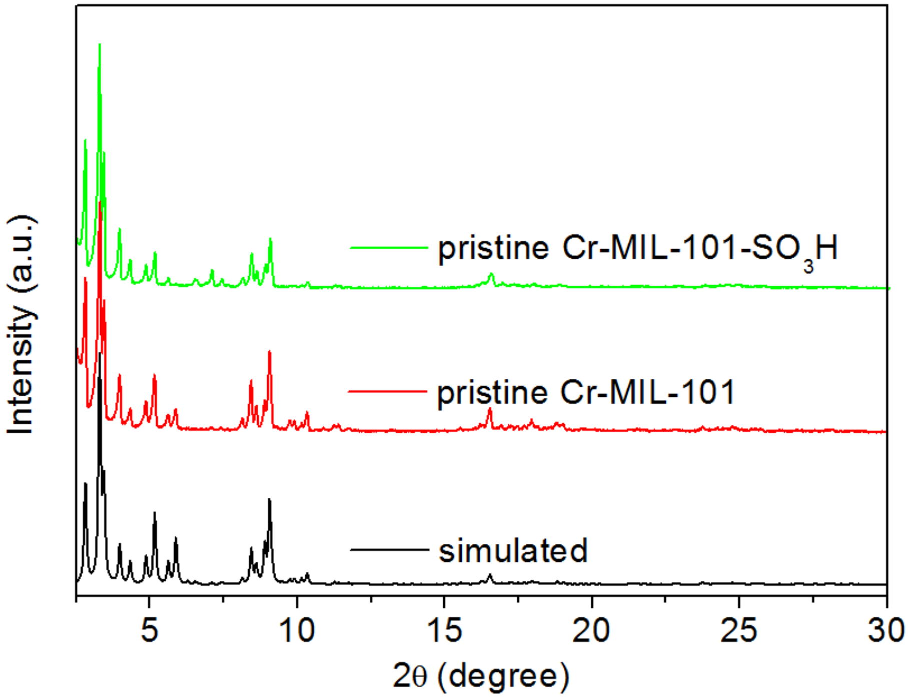

Figure 7. PXRD patterns of Cr-MIL-101-SO_3H and Cr-MIL-101 in comparison with the simulated pattern of Cr-MIL-101.

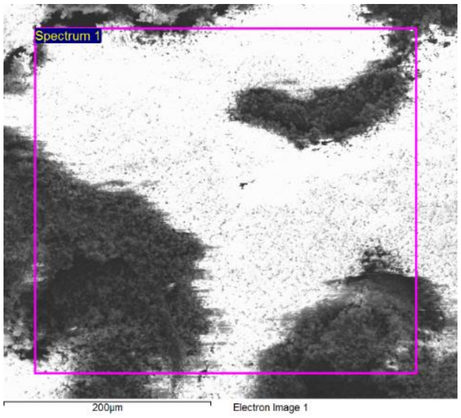

Figure 8. SEM image of Cr-MIL-101-SO_3H sample (1st measurement).

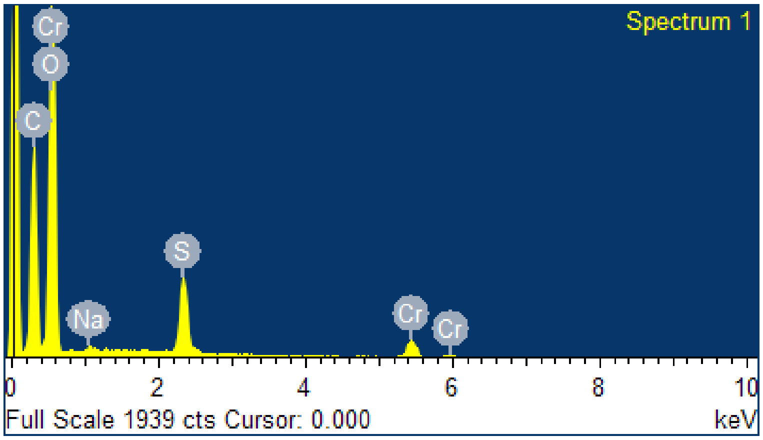

Figure 9. EDX spectrum of Cr-MIL-101-SO_3H sample (1st measurement).

Table 3. EDX data for Cr-MIL-101-SO_3H sample (1st measurement).

Element	Weight%	Atomic%
C K	29.57	44.63
O K	36.94	41.84
Na K	0.30	0.24
S K	7.98	4.51
Cr L	25.22	8.79
Totals	100.00	

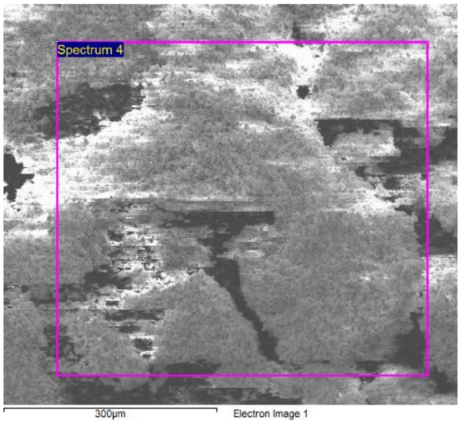

Figure 10. SEM image of Cr-MIL-101-SO_3H sample (2nd measurement).

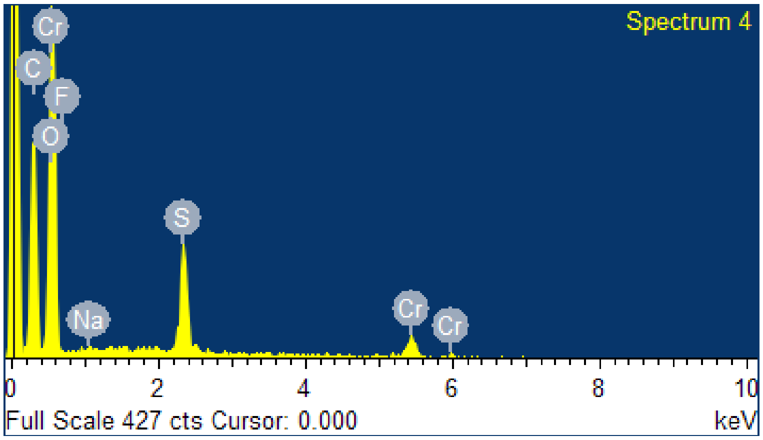

Figure 11. EDX spectrum of Cr-MIL-101-SO_3H sample (2nd measurement).

Table 4. EDX data for Cr-MIL-101-SO_3H sample (2nd measurement).

Element	Weight%	Atomic%
C K	28.18	45.80
O K	29.05	35.45
F K	0.73	0.76
Na K	0.23	0.19
S K	9.02	5.49
Cr L	32.79	12.31
Totals	100.00	

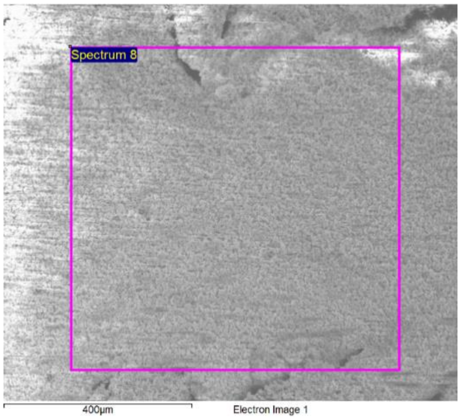

Figure 12. SEM image of Cr-MIL-101-SO$_3$H sample (3rd measurement).

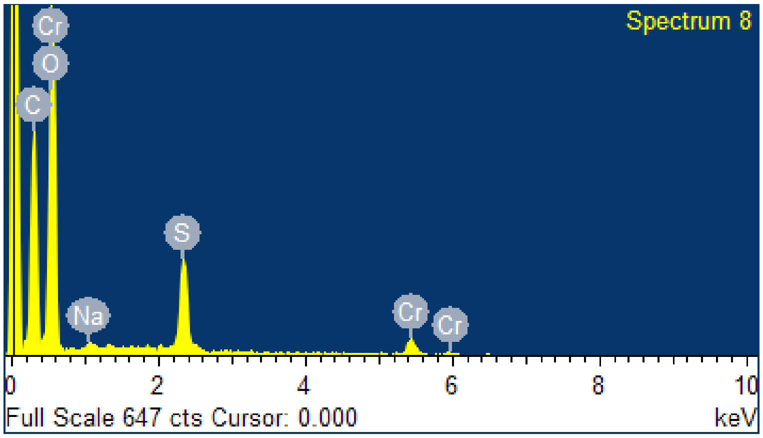

Figure 13. EDX spectrum of Cr-MIL-101-SO$_3$H sample (3rd measurement).

Table 5. EDX data for Cr-MIL-101-SO$_3$H sample (3rd measuremenet).

Element	Weight%	Atomic%
C K	33.15	47.72
O K	37.27	40.28
Na K	0.37	0.28
S K	9.77	5.26
Cr L	19.44	6.46
Totals	100.00	

Table 6. Summary of the EDX data of Cr-MIL-101-SO_3H sample.

	Na Atomic%	S Atomic%
1st measurement	0.24	4.51
2nd measurement	0.19	5.49
3rd measurement	0.28	5.26
Average	0.24	5.09

Na/S molar ratio = Na Atomic% / S Atomic% = 0.24% / 5.09% = 0.047 < 5%

In order to discover the most suitable alkylamine tethering condition for Cr-MIL-101-SO_3H to generate an adsorbent with the possibly highest CO_2 uptake for this material, we systematically studied experimental factors like alkylamine structure, alkylamine quantity, time and temperature, and solvent, and rationalized the results from a thermodynamic perspective.

2.3.2 Alkylamine Structure

As alkylamine structure significantly affects the CO_2 capture ability of the amine functionalized MOFs according to the reported examples,[9, 12, 13, 66] the effect of alkylamine structure was first studied by conducting control experiments using a variety of alkylamines (**Scheme 1**). Fully activated Cr-MIL-101-SO_3H samples were added to five different CH solutions containing 2 equiv. ethylene diamine (en), diethylenetriamine (DETA), triethylenetetramine (TETA), tetraethylenepentamine (TEPA), pentaethylenehexamine (PEHA) respectively. These suspensions were stirred at RT for 5 min before the modified MOFs (Cr-MIL-101-SO_3H-X, X = en, DETA, TETA, TEPA or PEHA) were separated from the solutions. The MOFs were washed with anhydrous CH, and were activated before the measurements of their gas uptakes (**Figure 14**).

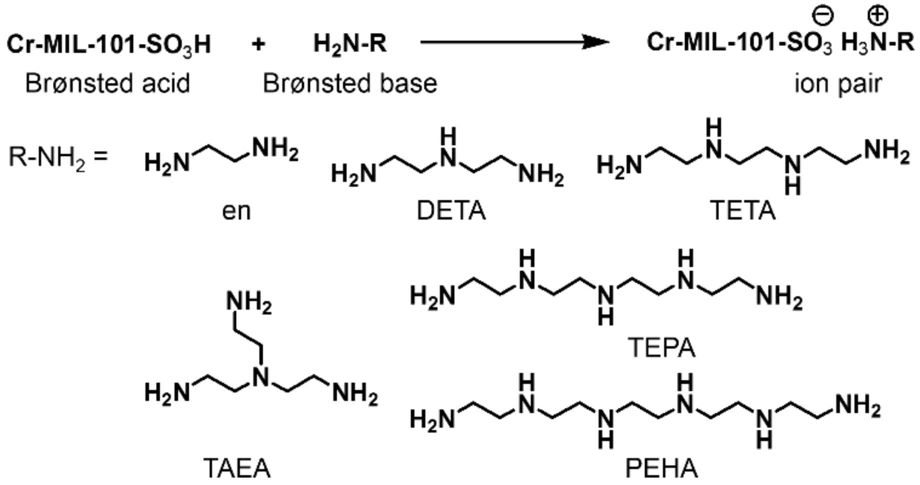

Scheme 1. Chemical structures of the alkylamine molecules and schematic illustration of their electrostatic interaction with Cr-MIL-101-SO_3H.

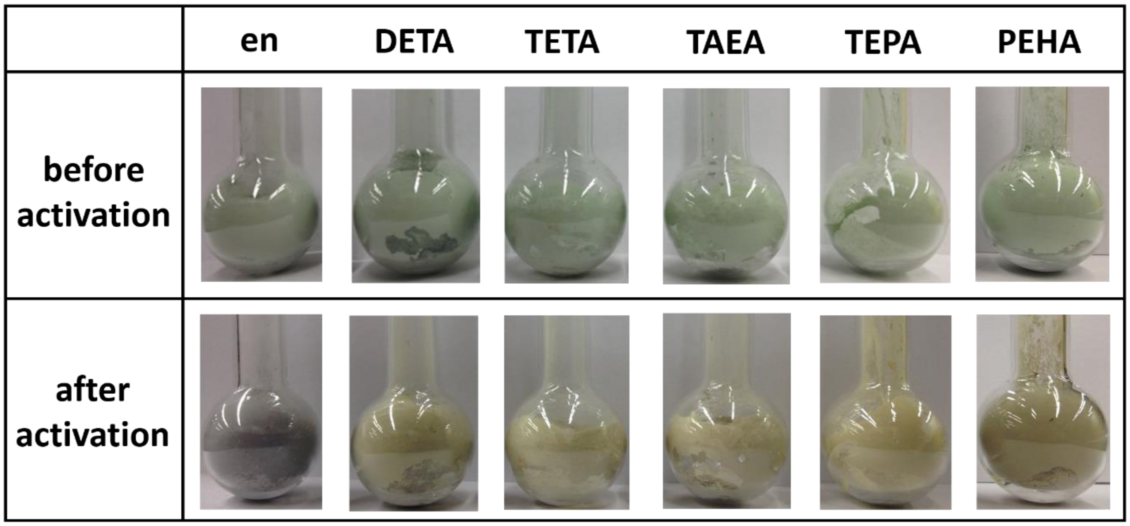

Figure 14. Colors of the different alkylamine modified Cr-MIL-101-SO_3H before and after activation at 80 °C under vacuum.

As the molecular weight of alkylamine increases from en to DETA, the CO_2 uptakes of alkylamine modified MOFs increase from 0.79 mmol/g to 2.23 mmol/g. (The data are provided at 150 mbar and 20 °C; unless otherwise mentioned, all the other CO_2 adsorption data in the text are given at the same pressure and temperature.) When the amine weight further increases from TETA to PEHA, the CO_2 uptake decreases from 1.94 mmol/g to 1.33 mmol/g. The maximum value occurs when DETA or TETA is applied (**Figure 15**). We propose that the result is related to the amine group density in the modified MOFs, which is determined by the number of amine groups in a single alkylamine molecule and the amount of alkylamine actually incorporated into the MOF. Small molecules like en are able to reach most of the amine grafting sites in Cr-MIL-101-SO_3H, including those located in very small pores. This leads to a large alkylamine loading amount in Cr-MIL-101-SO_3H-en. However, the advantage is dramatically offset by the number of amine groups in each en molecule. Therefore, the overall amine group density in Cr-MIL-101-SO_3H-en is rather limited. For large alkylamines like TEPA, PEHA, though each alkylamine molecule can bring more amine groups into the framework, the bulky structures severely hamper their access to the amine grafting sites. This gives rise to a low overall amine group density in Cr-MIL-101-SO_3H-TEPA or Cr-MIL-101-SO_3H-PEHA as well. DETA and TETA might be two alkylamines that strike a balance between the number of amine group in a single molecule and the amount of alkylamine incorporated into the MOF. Thus, they excel among the other linear alkylamines among the series and produce the modified MOFs with the highest amine group densities and highest CO_2 uptakes. Our explanation is well supported by the N/S atomic ratio in elemental analysis (**Table 7**).

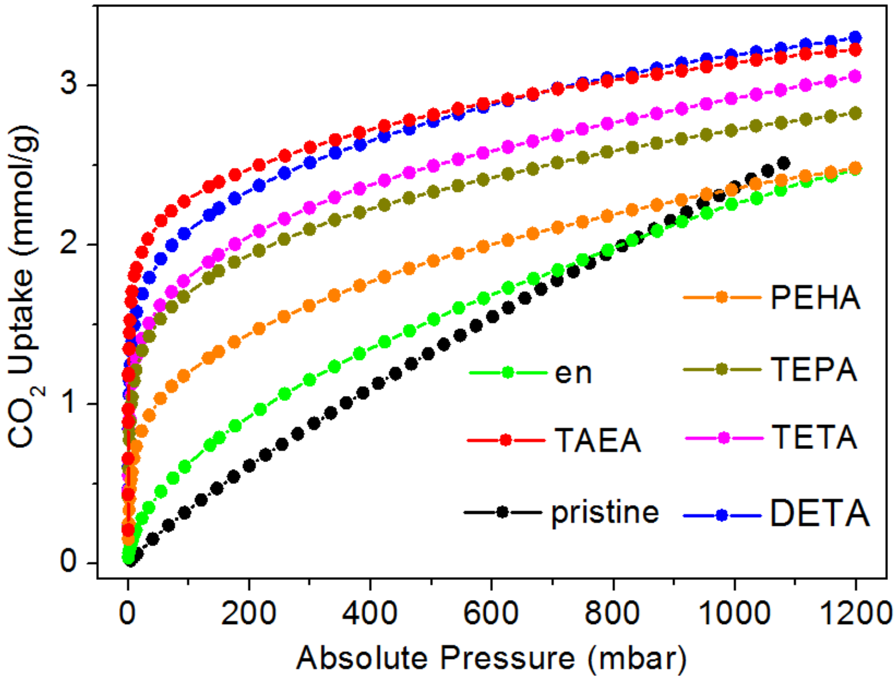

Figure 15. CO$_2$ uptakes at 20 °C of Cr-MIL-101-SO$_3$H modified with 2 equiv. different alkylamines. Control experiments were designed with alkylamine structure as the only variable. The other experimental factors are as follows: alkylamine quantity (2 equiv.), reaction time (5 min), reaction temperature (RT), and solvent (CH).

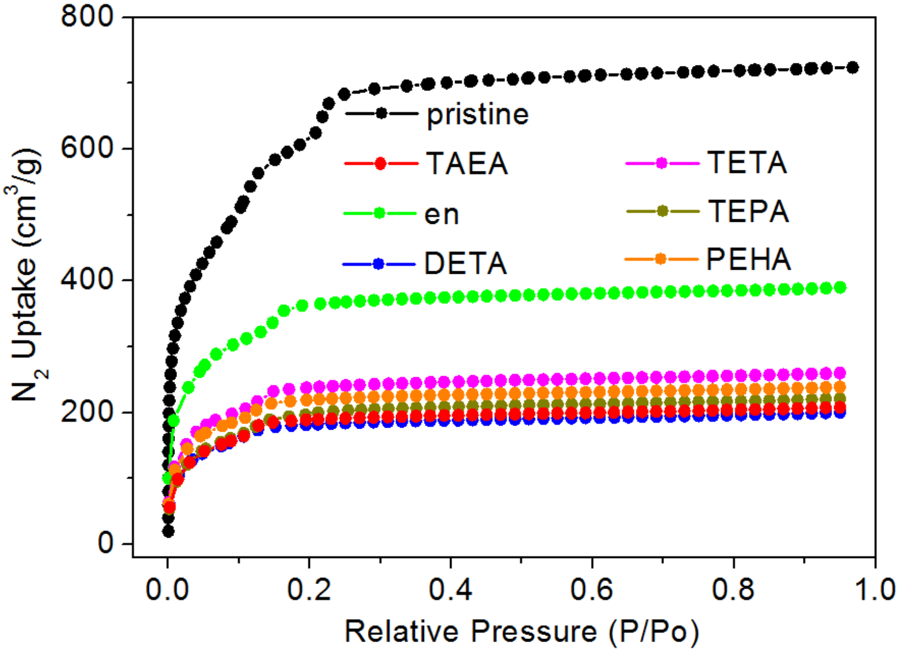

Figure 16. N_2 uptakes at 77 K of Cr-MIL-101-SO_3H modified with 2 equiv. different alkylamines. Control experiments were designed with alkylamine structure as the only variable. The other experimental factors are as follows: alkylamine quantity (2 equiv.), reaction time (5 min), reaction temperature (RT), and solvent (CH).

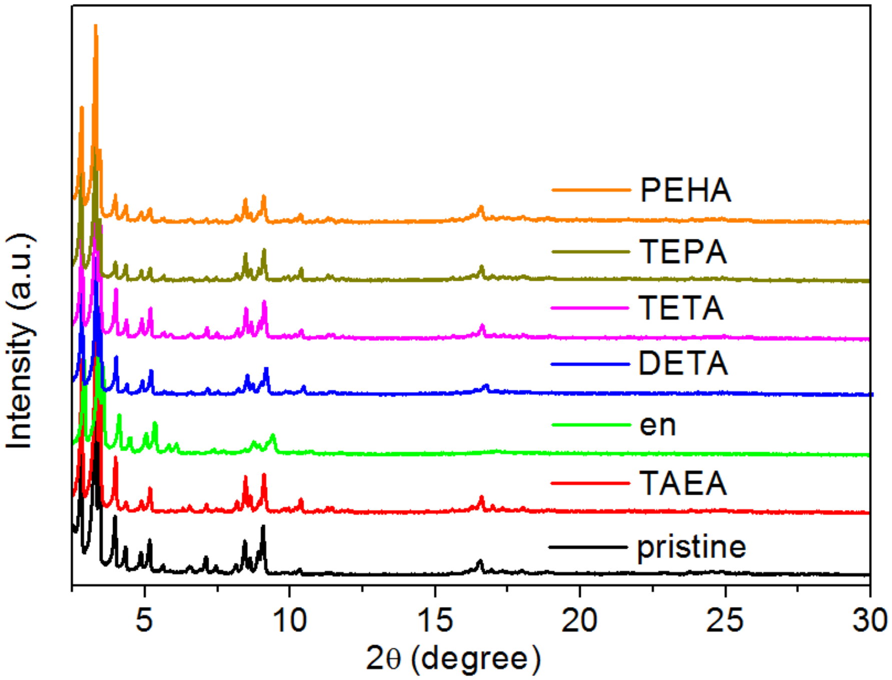

Figure 17. PXRD patterns of Cr-MIL-101-SO_3H modified with 2 equiv. different alkylamines. Control experiments were designed with alkylamine structure as the only variable. The other experimental factors are as follows: alkylamine quantity (2 equiv.), reaction time (5 min), reaction temperature (RT), and solvent (CH).

Table 7. Summary of the N/S atomic ratios of Cr-MIL-101-SO_3H modified with 2 equiv. different alkylamines. Control experiments were designed with alkylamine structure as the only variable. The other experimental factors are as follows: alkylamine quantity (2 equiv.), reaction time (5 min), reaction temperature (RT), and solvent (CH). The data were obtained by EA.

Alkylamine structure	N weight%	S weight%	N/S atomic ratio
en	10.03	6.92	3.31
DETA	13.26	5.85	5.18
TETA	11.34	5.07	5.11
TEPA	10.98	5.04	4.98
PEHA	10.80	5.57	4.43
TAEA	12.19	5.25	5.31

We also tethered TAEA, the isomer of TETA, into Cr-MIL-101-SO_3H, because these two alkylamines have the same number of amine groups in a molecule. Therefore, a high CO_2 uptake might also occur in the case of Cr-MIL-101-SO_3H-TAEA. It turns out that the CO_2 uptake of TAEA modified Cr-MIL-101-SO_3H (2.39 mmol/g) is even higher than those of TETA (1.94 mmol/g) and DETA (2.23 mmol/g) counterparts. We propose that the branched geometry of TAEA is more compact than the linear one of TETA, making TAEA migrate into Cr-MIL-101-SO_3H and have access to the amine grafting sites more easily than TETA. Thus the larger alkylamine loading amount in Cr-MIL-101-SO_3H-TAEA leads to its higher amine group density (**Table 7**), and higher CO_2 uptake. Based on the aforementioned, TAEA was chosen to be the optimal alkylamine to incorporate into Cr-MIL-101-SO_3H.

2.3.3 Alkylamine Quantity

Pore volume distribution indicates that the population of mesopores in Cr-MIL-101-SO_3H-TAEA significantly decreases (**Figure 16** and **Figure 18**), while its PXRD pattern suggests there is no collapse or phase change of the framework (**Figure 17**). These reveal the successful incorporation of TAEA into the cages of the framework. To probe the chemical nature of the captured TAEA in Cr-MIL-101-SO_3H-TAEA, IR spectra of Cr-MIL-101-SO_3H, Cr-MIL-101-SO_3H-TAEA and anhydrous TAEA were collected (**Figure 19-22**). Cr-MIL-101-SO_3H-TAEA exhibits two new peaks at 3234 and 3147 cm^{-1}, which are attributed to the stretching vibrations of $–NH_3^+$.[77] This suggests the proton transfer from $–SO_3H$ to $–NH_2$ and the formation of ammonium, which is consistent with our hypothesis.

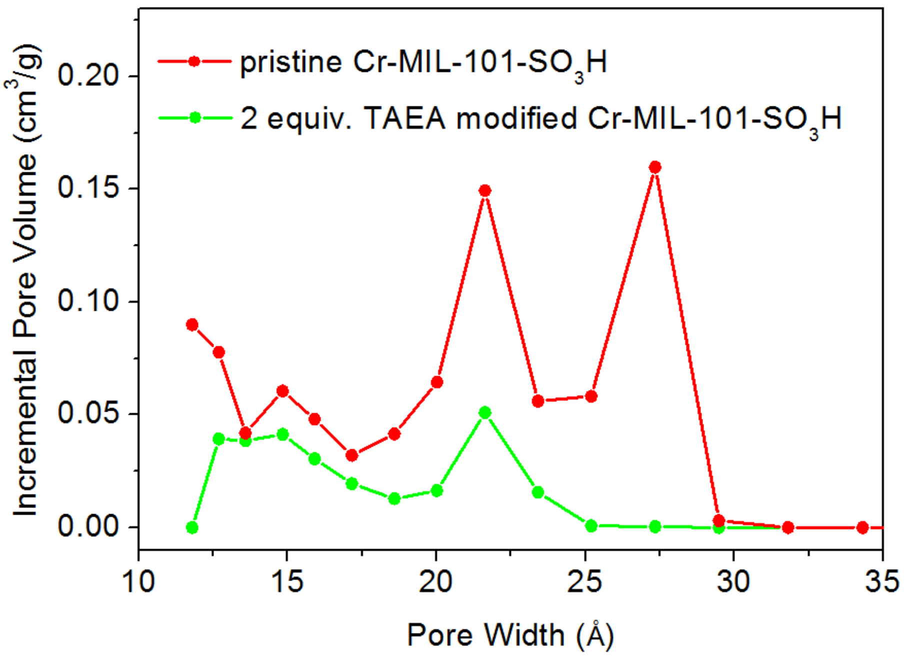

Figure 18. Incremental pore size distribution diagram of Cr-MIL-101-SO_3H-TAEA (modified by 2 equiv. TAEA) in comparison with that of the pristine Cr-MIL-101-SO_3H.

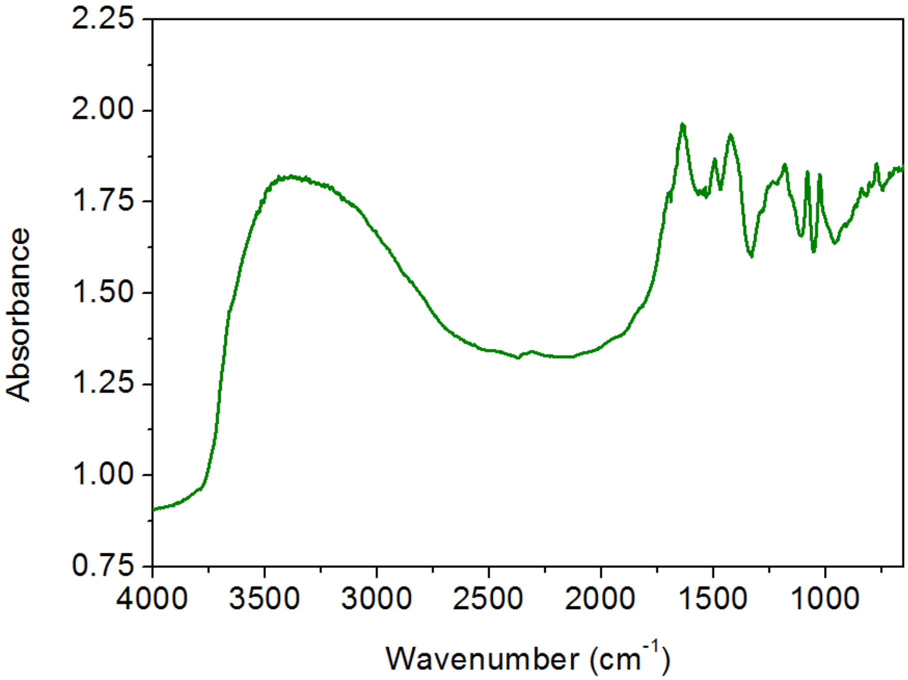

Figure 19. DRIFT spectrum of Cr-MIL-101-SO_3H under N_2 atmosphere.

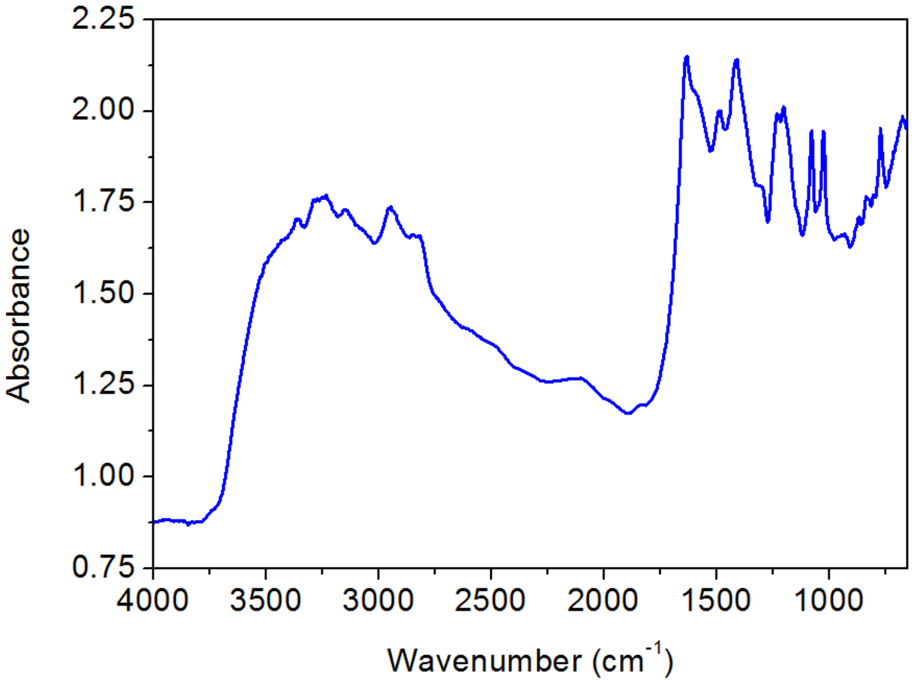

Figure 20. DRIFT spectrum of Cr-MIL-101-SO_3H-TAEA under N_2 atmosphere.

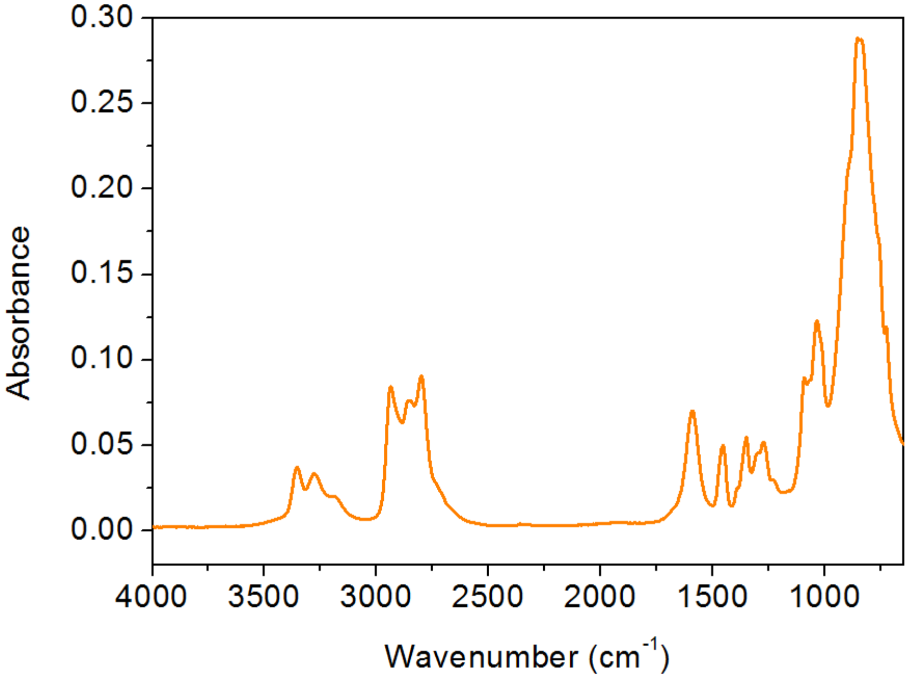

Figure 21. ATR-IR spectrum of anhydrous TAEA under N_2 atmosphere.

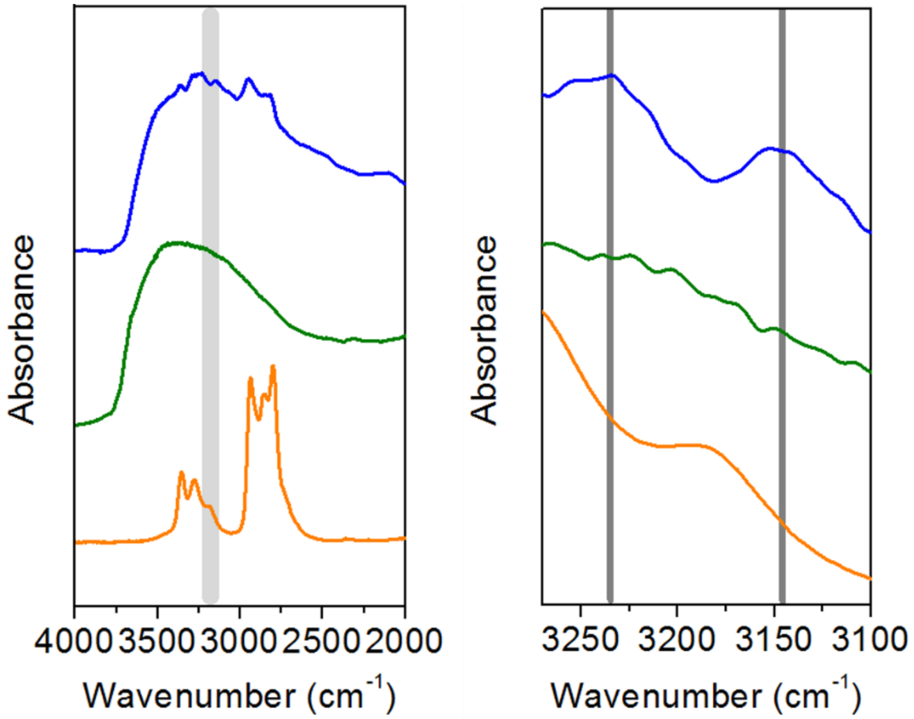

Figure 22. Comparison of the FTIR spectra of Cr-MIL-101-SO_3H-TAEA (blue), pristine Cr-MIL-101-SO_3H (green), and anhydrous TAEA (orange). (Left) The FTIR spectra in the range of stretching frequency with the region of interest highlighted in grey. (Right) The expanded region of interest with the characteristic peaks of Cr-MIL-101-SO_3H-TAEA marked at 3234 and 3147 cm^{-1}.

It is worth noting that the pore volume of the Cr-MIL-101-SO_3H modified by 2 equiv. TAEA is 0.32 cm^3/g and the mesopores still exist (**Figure 16**). This indicates that there is still extra room in the framework to accommodate more alkylamine for a higher CO_2 uptake. Therefore, attempt was further made by enhancing the quantity of TAEA in solution to be 4, 8, 12 and 16 equiv., while maintaining the other experimental factors (**Figure 23-25**). The order of CO_2 uptakes in terms of TAEA quantity is 2 equiv. (2.40 mmol/g) < 4 equiv. (2.56 mmol/g) < 8 equiv. (2.75 mmol/g) > 12 equiv. (2.56 mmol/g) > 16 equiv. (2.00 mmol/g) (**Figure 23**). When TAEA quantity is small, the amount of the

TAEA loaded into the MOF is the main limiting factor for CO_2 uptake. More TAEA molecules can be incorporated into Cr-MIL-101-SO_3H as TAEA quantity increases, which leads to a higher CO_2 uptake. As TAEA quantity continues to increase, TAEA molecules occupy more space inside the framework (**Table 8**), eventually making some amine grafting sites inapproachable for CO_2. In this situation, accessible pore volume becomes the determining factor for the CO_2 uptake of the adsorbent. Thus, a modest quantity of TAEA is crucial to guarantee sufficient amine groups in MOF as well as easy access to amine groups for CO_2 molecules. With limited experiments, we chose 8 equiv. TAEA to be the optimal amount for alkylamine tethering in Cr-MIL-101-SO_3H.

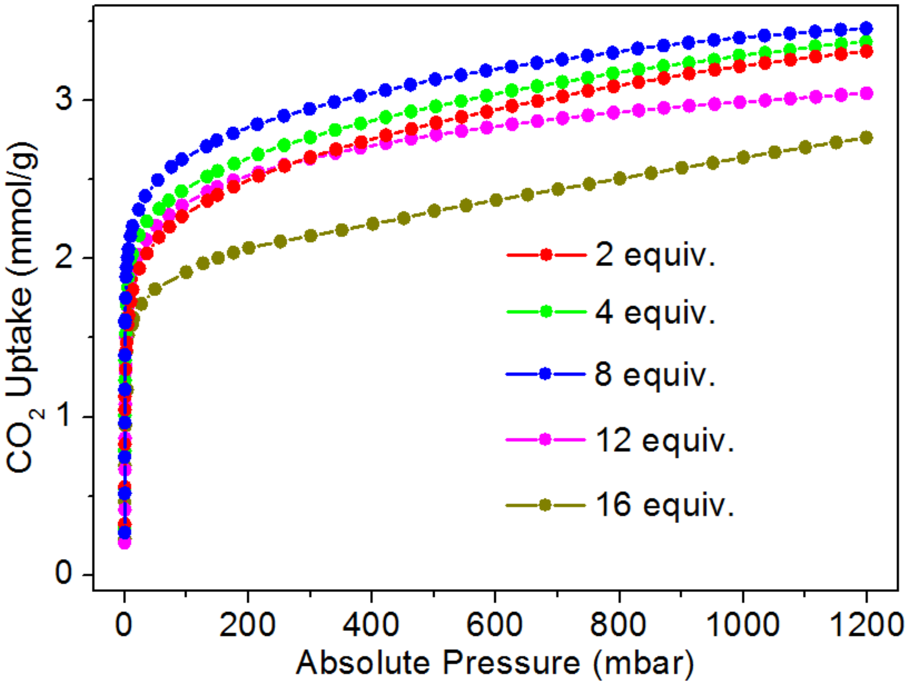

Figure 23. CO_2 uptakes at 20 °C of Cr-MIL-101-SO_3H modified by different amounts of TAEA. Control experiments were designed with alkylamine quantity as the only variable. The other experimental factors are as follows: alkylamine (TAEA), reaction time (5 min), reaction temperature (RT), and solvent (CH).

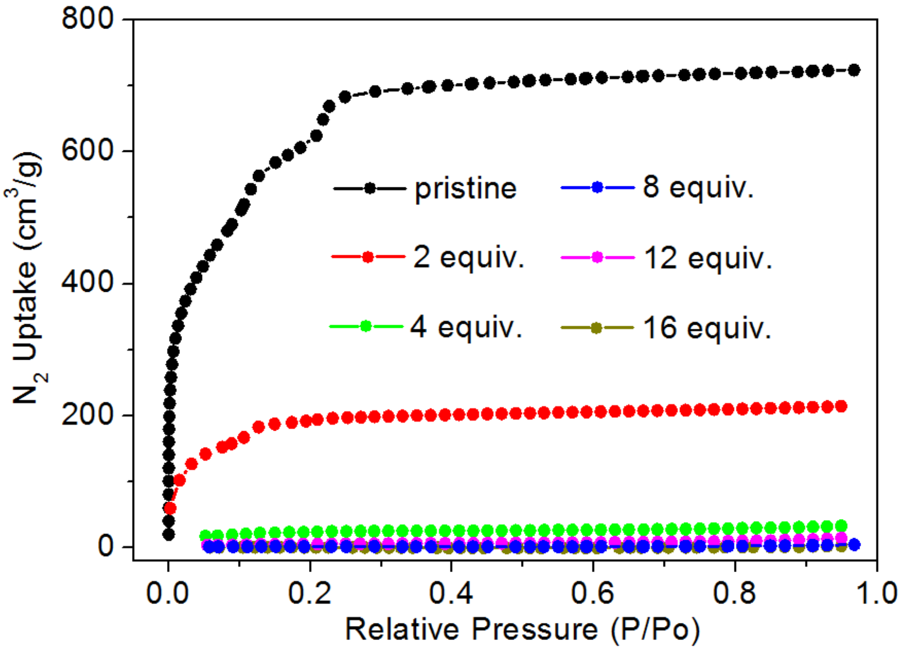

Figure 24. N_2 uptakes at 77 K of Cr-MIL-101-SO_3H modified by different amounts of TAEA. Control experiments were designed with alkylamine quantity as the only variable. The other experimental factors are as follows: alkylamine (TAEA), reaction time (5 min), reaction temperature (RT), and solvent (CH).

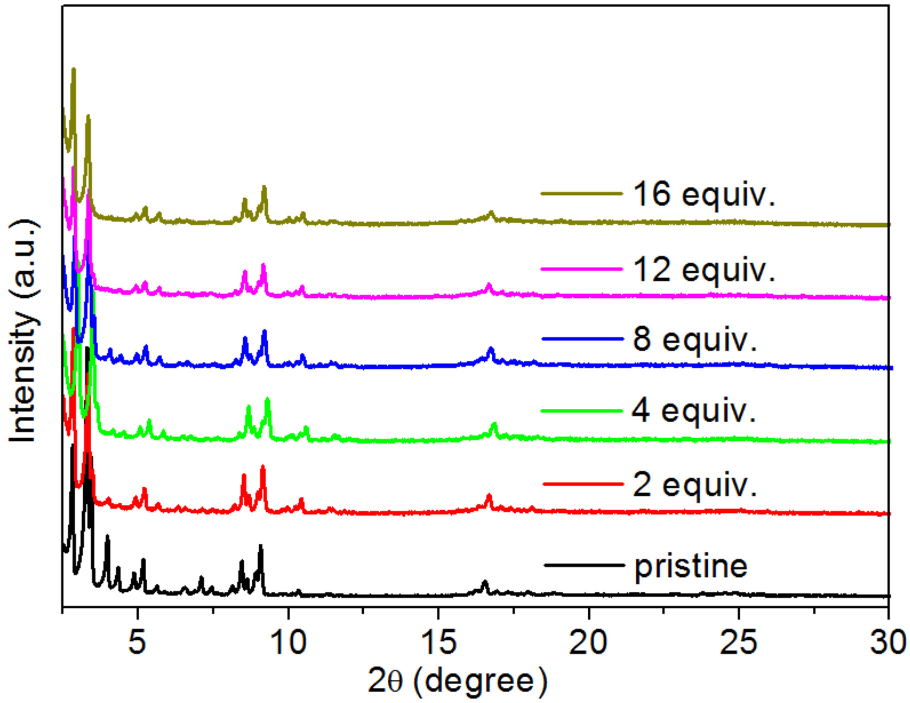

Figure 25. PXRD patterns of Cr-MIL-101-SO_3H modified by different amounts of TAEA. Control experiments were designed with alkylamine quantity as the only variable. The other experimental factors are as follows: alkylamine (TAEA), reaction time (5 min), reaction temperature (RT), and solvent (CH).

Table 8. Summary of the N/S ratios of Cr-MIL-101-SO_3H modified by different amounts of TAEA. Control experiments were designed with alkylamine quantity as the only variable. The other experimental factors are as follows: alkylamine (TAEA), reaction time (5 min), reaction temperature (RT), and solvent (CH). The data were obtained by EA.

Alkylamine quantity	N weight%	S weight%	N/S atomic ratio
2 equiv.	12.19	5.25	5.31
4 equiv.	13.42	4.78	6.42
8 equiv.	16.14	4.76	7.75
12 equiv.	16.20	4.65	7.96
16 equiv.	16.07	4.56	8.06

2.3.4 Time and Temperature

Although many examples of alkylamine functionalization in MOFs have been reported,[9, 12, 13, 65, 66] a comprehensive optimization of amine tethering process is still missing, which inspires us to think whether the maximum CO_2 uptakes have been achieved for certain MOFs. More importantly, it is unclear why a certain amine tethering condition is adopted for a MOF and whether it is still applicable to other MOFs. To determine the optimal experimental condition of our system for the maximum CO_2 uptake, as well as to reveal the key factors that influence the integration of alkylamine into MOFs, we further studied other experimental factors, namely the reaction time and temperature in amine tethering.

Two series of control experiments were designed with amine tethering time and temperature as the only variable respectively. In the first set of experiments, reaction time was tuned to be 10 min, 30 min, 1h and 12 h, while reaction temperature was maintained at RT (**Figure 26-28**). Compared with Cr-MIL-101-SO_3H-TAEA prepared in 5 min at RT (2.75 mmol/g), the adsorbent prepared in 10 min at RT exhibits almost the same high CO_2 uptake (2.65 mmol/g) (**Figure 26**). However, Cr-MIL-101-SO_3H-TAEA samples prepared for a longer time show a decline in CO_2 uptakes, which might be attributed to the gradual decomposition of the frameworks, as supported by the obvious attenuated peaks in the PXRD pattern of the sample prepared in 12 h. In the second set, the reaction time was kept to be 5 min but reaction temperatures were increased to 40 °C and 60 °C (**Figure 29-31**). The result shows that the samples prepared at RT (2.75 mmol/g), 40 °C

(2.78 mmol/g) and 60 °C (2.69 mmol/g) in 5 min possess almost the same amount of CO_2 uptake (**Figure 29**).

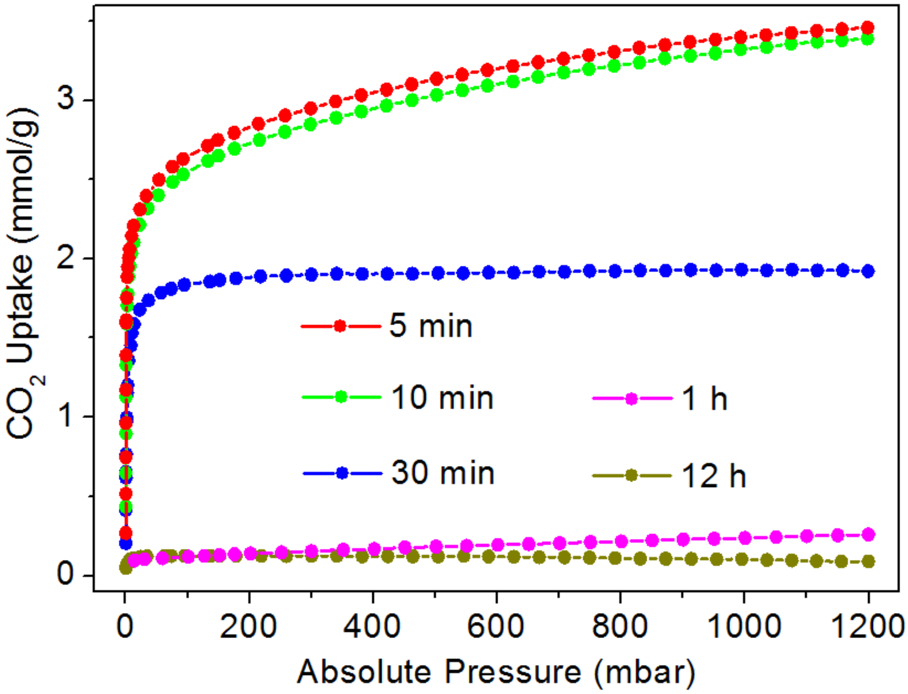

Figure 26. CO_2 uptakes at 20 °C of Cr-MIL-101-SO_3H-TAEA prepared in different periods of time. Control experiments were designed with reaction time as the only variable. The other experimental factors are as follows: alkylamine (TAEA), alkylamine quantity (8 equiv.), reaction temperature (RT), and solvent (CH).

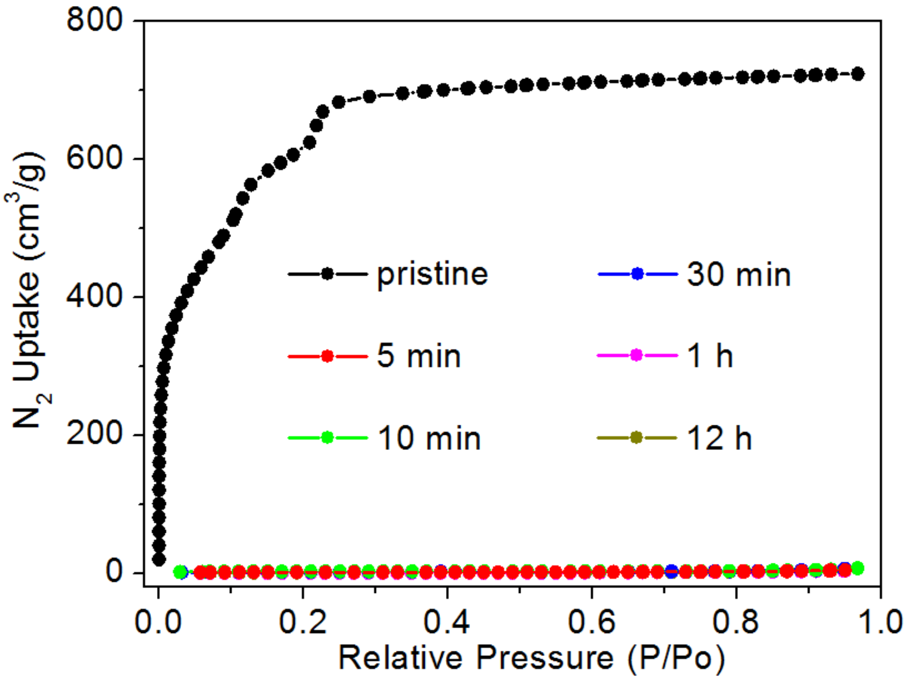

Figure 27. N_2 uptakes at 77 K of Cr-MIL-101-SO_3H-TAEA prepared in different periods of time. Control experiments were designed with reaction time as the only variable. The other experimental factors are as follows: alkylamine (TAEA), alkylamine quantity (8 equiv.), reaction temperature (RT), and solvent (CH).

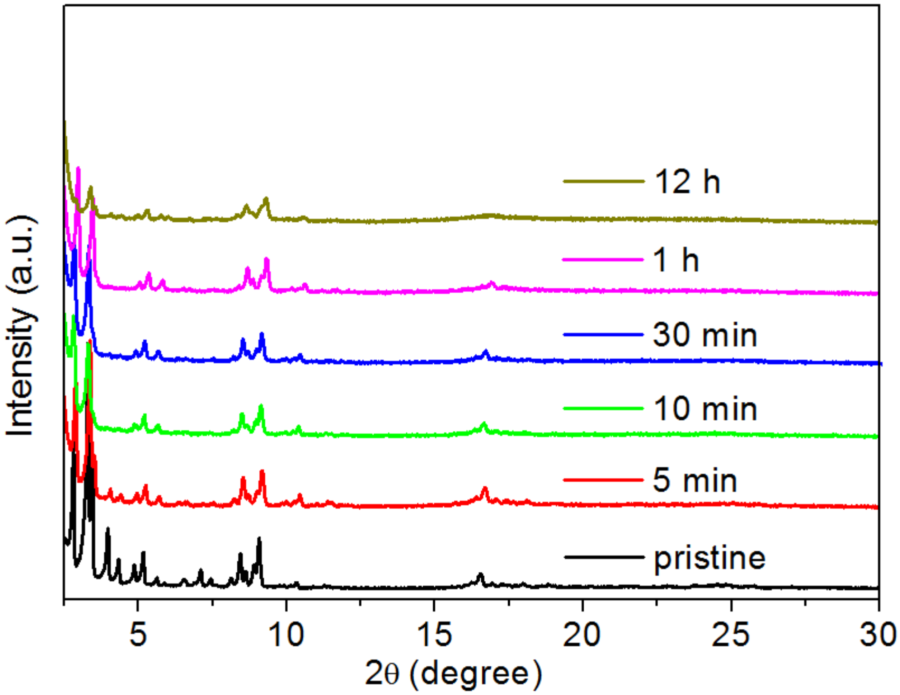

Figure 28. PXRD patterns of Cr-MIL-101-SO_3H-TAEA prepared in different periods of time. Control experiments were designed with reaction time as the only variable. The other experimental factors are as follows: alkylamine (TAEA), alkylamine quantity (8 equiv.), reaction temperature (RT), and solvent (CH).

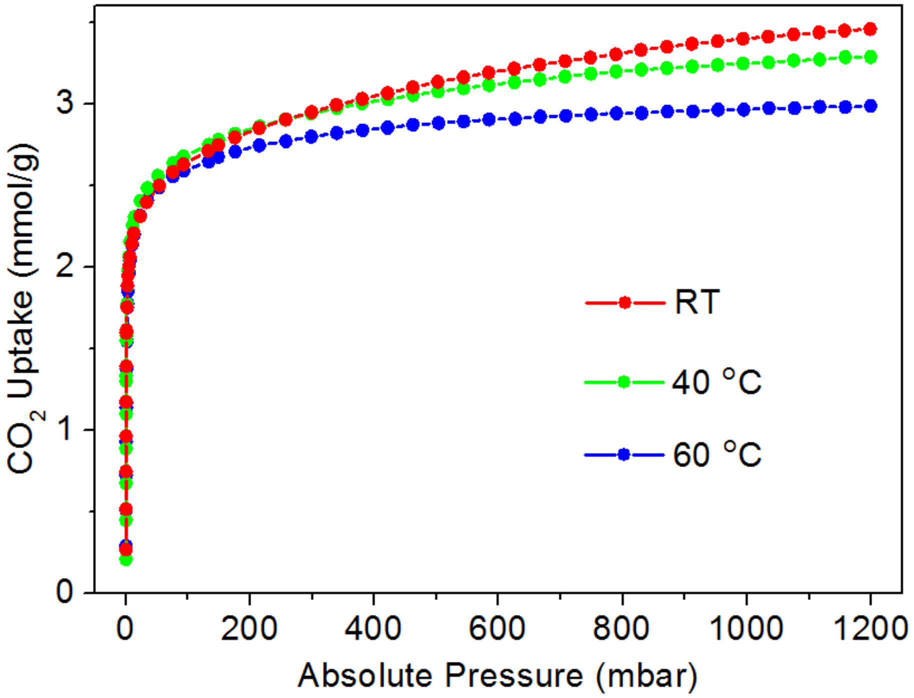

Figure 29. CO$_2$ uptakes at 20 °C of Cr-MIL-101-SO$_3$H-TAEA prepared under different temperatures. Control experiments were designed with reaction temperature as the only variable. The other experimental factors are as follows: alkylamine (TAEA), alkylamine quantity (8 equiv.), reaction time (5 min), and solvent (CH).

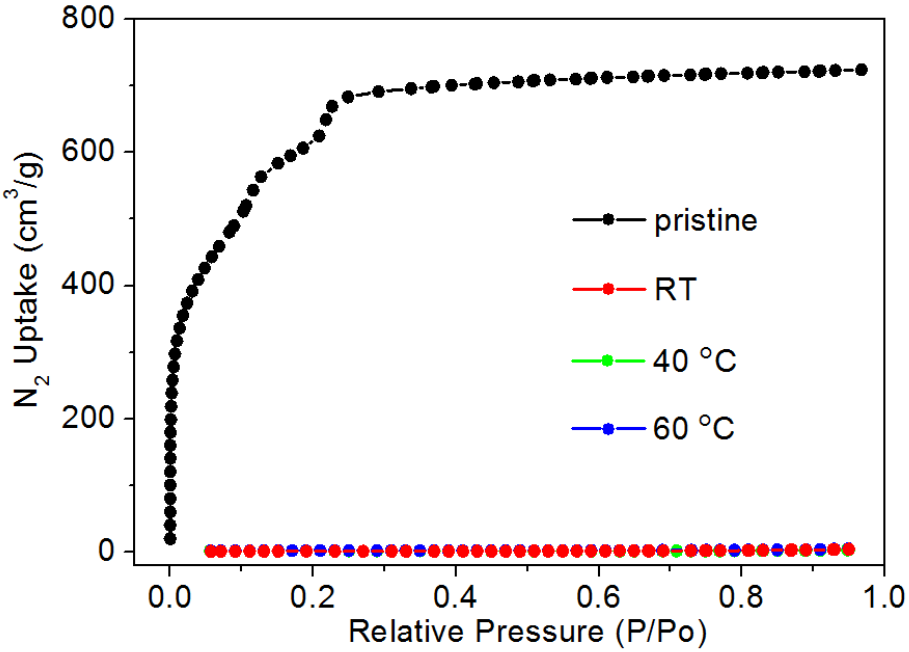

Figure 30. N_2 uptakes at 77 K of Cr-MIL-101-SO_3H-TAEA prepared under different temperatures. Control experiments were designed with reaction temperature as the only variable. The other experimental factors are as follows: alkylamine (TAEA), alkylamine quantity (8 equiv.), reaction time (5 min), and solvent (CH).

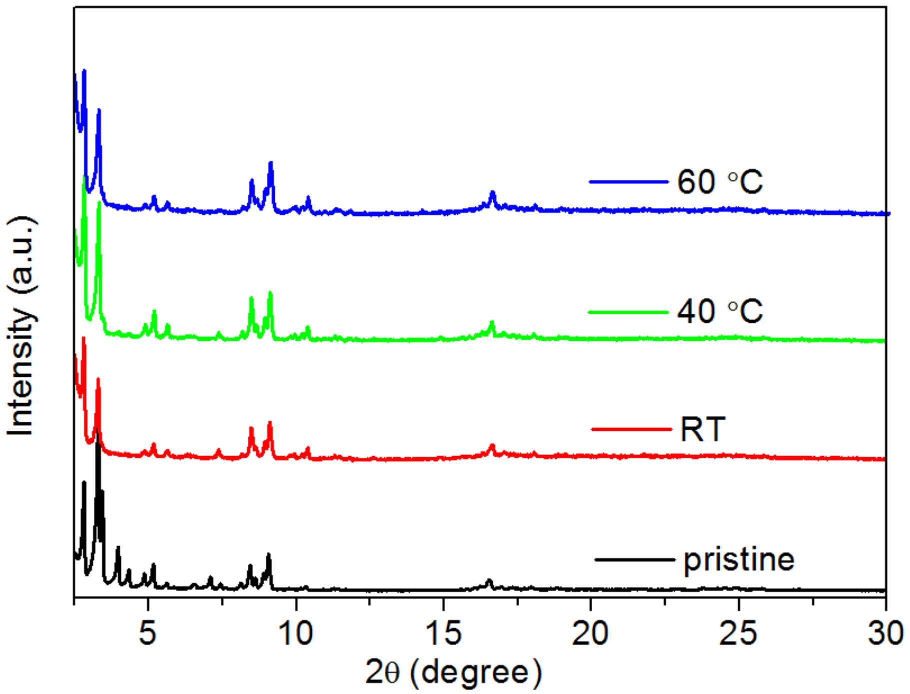

Figure 31. PXRD patterns of Cr-MIL-101-SO_3H-TAEA prepared under different temperatures. Control experiments were designed with reaction temperature as the only variable. The other experimental factors are as follows: alkylamine (TAEA), alkylamine quantity (8 equiv.), reaction time (5 min), and solvent (CH).

Both sets of the experiments reveal that the distribution equilibrium of TAEA between the solution phase and the MOF phase can be reached within 5 min at RT. It suggests that this amine tethering method is highly time and energy efficient compared with the precedent works in which the suspensions are usually refluxed or stirred under RT for more than 12 h.[9, 12, 13, 65, 66] We propose there are two main reasons accounting for the easy achievement of the distribution equilibrium. Firstly, the ionic bond between –SO_3^- and –NH_3^+ makes the alkylamine not so strongly localized to the amine grafting site as in a coordination bond, which facilitates the migration of alkylamine molecules deep into the framework. Secondly, Cr-MIL-101-SO_3H is a mesoporous structure with large cage windows,[76] making it facile for large alkylamine molecules to diffuse and reach the amine tethering sites located in the interior part of the framework. Therefore, based on the control experiments, the optimal amine tethering time and temperature for this system are 5 min and RT.

2.3.5 Solvent

As mentioned, the incorporation of TAEA into Cr-MIL-101-SO_3H can be regarded as the distribution of TAEA between solution phase and the MOF phase. Therefore, the nature of the solvent might also affect the amine loading process, which has been significantly overlooked in the previously reported works. To seek an optimal solvent for our system, we selected three other anhydrous solvents besides CH, namely tetrahydrofuran (THF), dichloromethane (DCM), and methanol (MeOH), to perform control experiments (**Figure 32-34**). The CO_2 uptakes of products prepared in different solvents are CH (2.75 mmol/g) > THF (2.43 mmol/g) > DCM (2.29 mmol/g) > MeOH (1.38 mmol/g) (**Figure 32**), and those of amine loading amount and porosity are exactly the reverse (**Table 9** and **Figure 32**). It again shows that the CO_2 uptake of Cr-MIL-101-SO_3H-TAEA is higher when a larger amount of TAEA is loaded into the MOF when the accessible pore volume is sufficient. In view of the previous discussion, the distribution equilibrium of TAEA between the solution phase and the MOF phase is reached within 5 min at RT in CH. Therefore, to explain the above sequence, efforts should first be devoted to clarifying whether equilibria were also achieved in the cases of THF, DCM and MeOH.

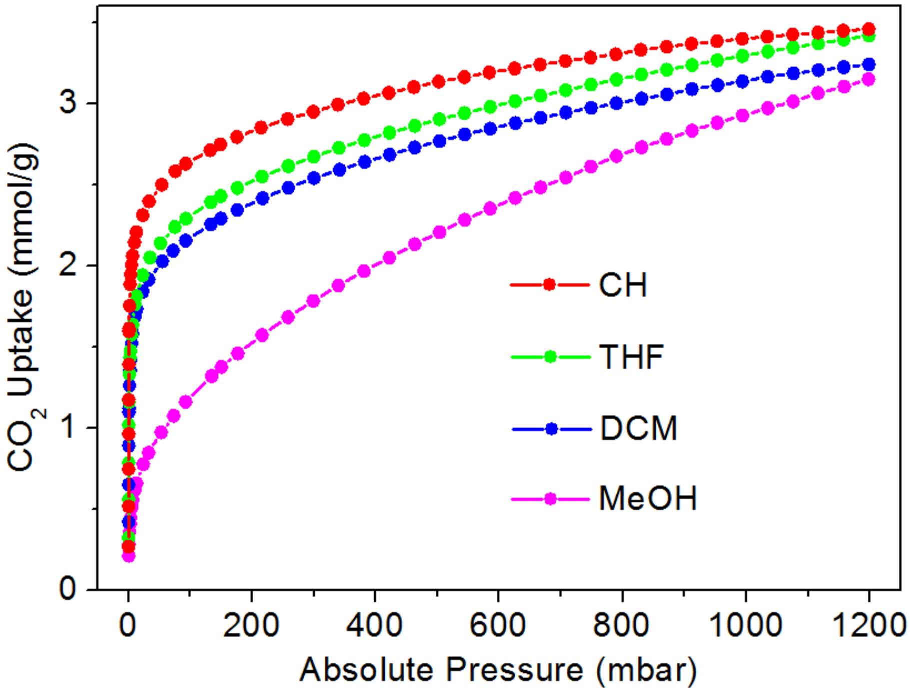

Figure 32. CO$_2$ uptakes at 20 °C of Cr-MIL-101-SO$_3$H-TAEA prepared in different solvents. Control experiments were designed with solvent as the only variable. The other experimental factors are as follows: alkylamine (TAEA), alkylamine quantity (8 equiv.), reaction time (5 min), and reaction temperature (RT).

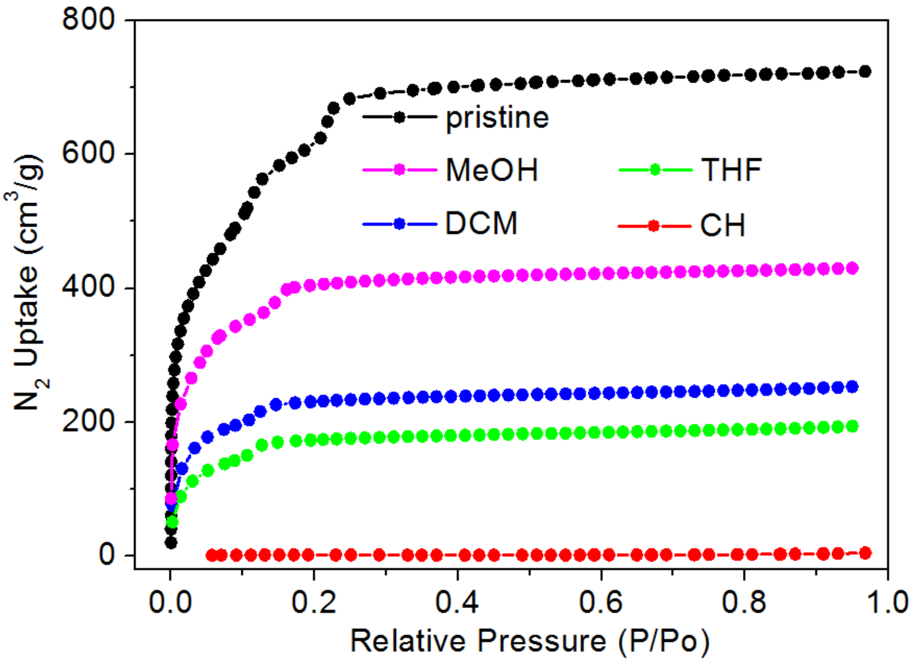

Figure 33. N_2 uptakes at 77 K of Cr-MIL-101-SO_3H-TAEA prepared in different solvents. Control experiments were designed with solvent as the only variable. The other experimental factors are as follows: alkylamine (TAEA), alkylamine quantity (8 equiv.), reaction time (5 min), and reaction temperature (RT).

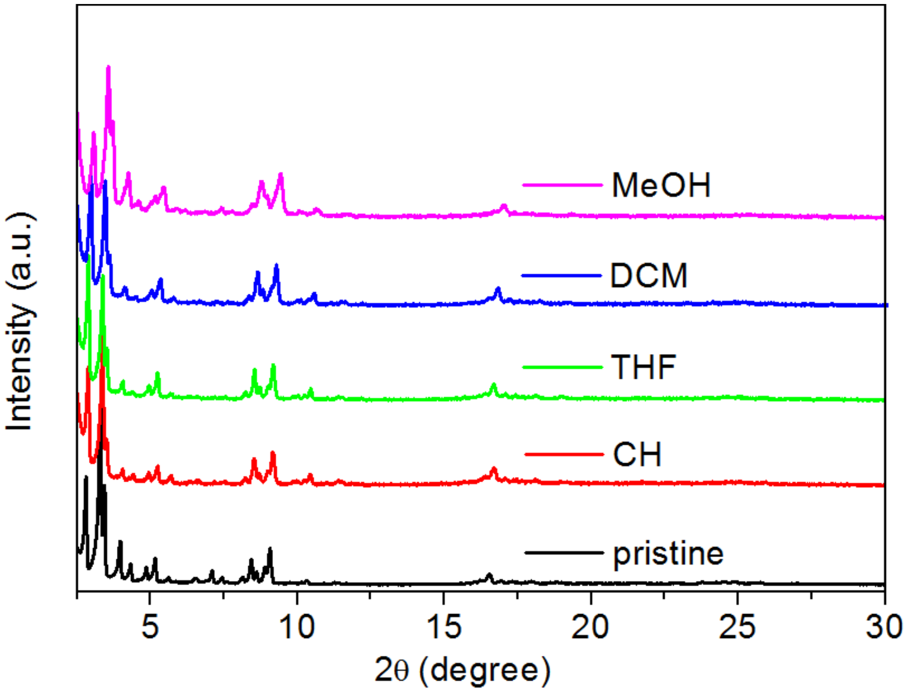

Figure 34. PXRD patterns of Cr-MIL-101-SO_3H-TAEA prepared in different solvents. Control experiments were designed with solvent as the only variable. The other experimental factors are as follows: alkylamine (TAEA), alkylamine quantity (8 equiv.), reaction time (5 min), and reaction temperature (RT).

Table 9. Summary of the N/S ratios of Cr-MIL-101-SO_3H-TAEA prepared in different solvents. Control experiments were designed with solvent as the only variable. The other experimental factors are as follows: alkylamine (TAEA), alkylamine quantity (8 equiv.), reaction time (5 min), and reaction temperature (RT).

Solvent	N weight%	S weight%	N/S atomic ratio
CH	16.14	4.76	7.75
THF	10.97	4.83	5.19
DCM	10.54	5.14	4.69
MeOH	9.79	6.26	3.57

The case of MeOH is selectively examined because it generates a sample with the lowest CO_2 uptake, which is as representative as the sample with the highest CO_2 uptake prepared in CH. Thus we conducted control experiments in MeOH with amine tethering time extended to 2h and 12h (**Figure 35-37**). Compared with Cr-MIL-101-SO_3H-TAEA prepared in 5 min in MeOH, neither the CO_2 uptakes nor the porosities of these two samples have apparent differences (**Figure 35-36**), which indicates the distribution equilibrium of TAEA between the solution phase and the MOF phase is reached within 5 min in MeOH at RT. Therefore, it is reasonable to assume the equilibria are also achieved in the cases of THF and DCM, and the aforementioned sequence should be explained from a thermodynamic perspective.

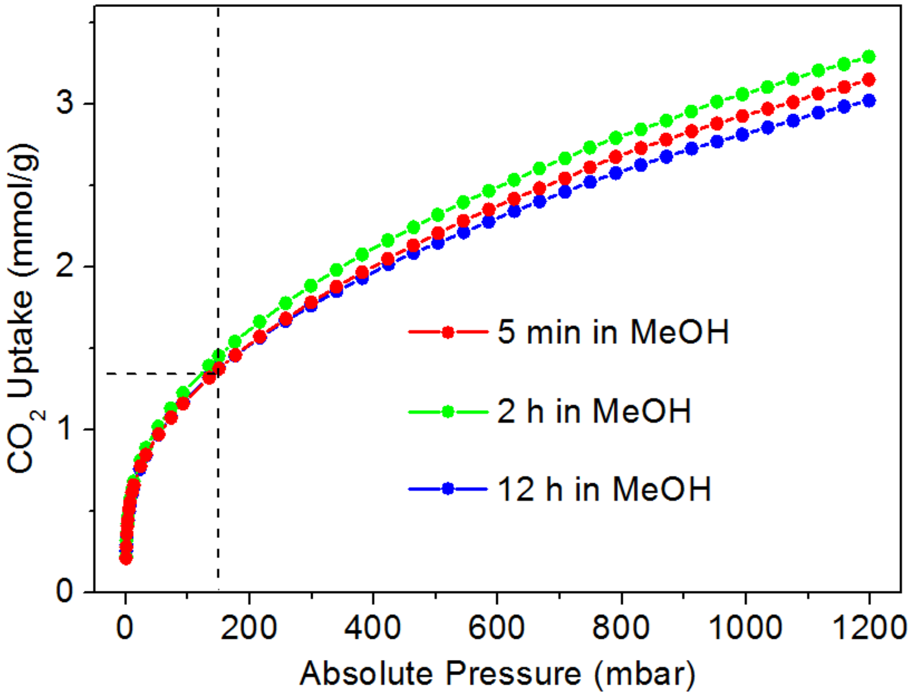

Figure 35. The CO_2 uptakes at 20 °C of Cr-MIL-101-SO_3H-TAEA prepared in different periods of time in MeOH. Control experiments were designed with reaction time as the only variable. The other experimental factors are as follows: alkylamine (TAEA), alkylamine quantity (8 equiv.), reaction temperature (RT), and solvent (MeOH).

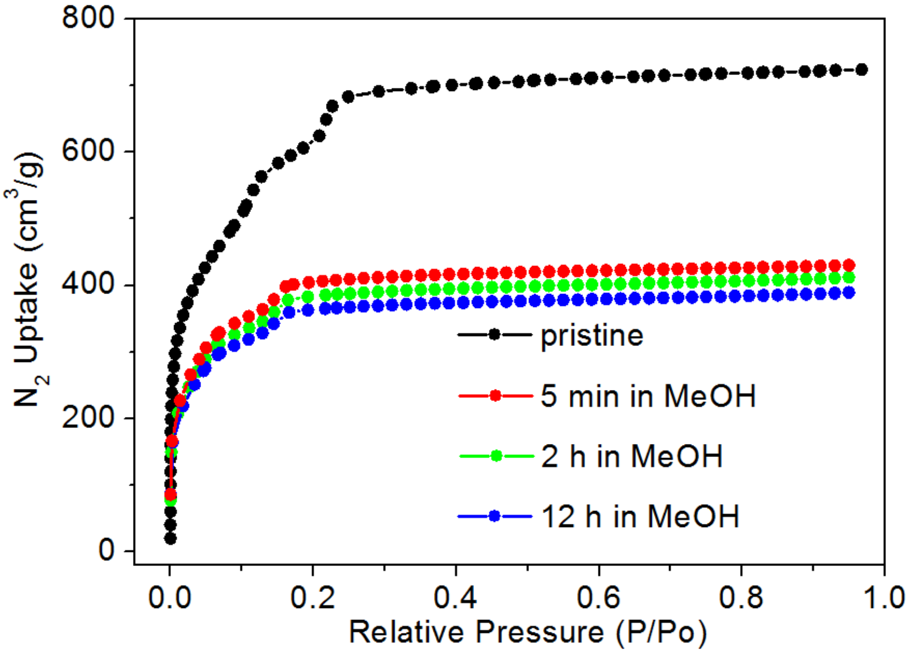

Figure 36. The N_2 uptakes at 77 K of Cr-MIL-101-SO_3H-TAEA prepared in different periods of time in MeOH. Control experiments were designed with reaction time as the only variable. The other experimental factors are as follows: alkylamine (TAEA), alkylamine quantity (8 equiv.), reaction temperature (RT), and solvent (MeOH).

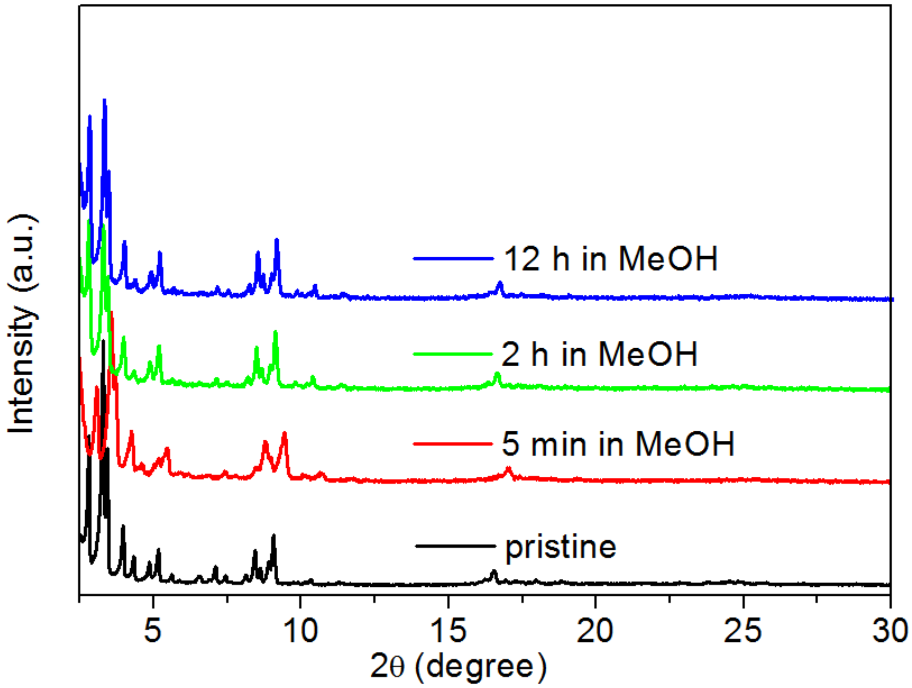

Figure 37. PXRD patterns of Cr-MIL-101-SO_3H-TAEA prepared in different periods of time in MeOH. Control experiments were designed with reaction time as the only variable. The other experimental factors are as follows: alkylamine (TAEA), alkylamine quantity (8 equiv.), reaction temperature (RT), and solvent (MeOH).

Since TAEA contains many polar amine groups, the interaction between TAEA and solvent would be stronger in more polar solvent than that in less polar solvent. As a result, TAEA dispersed in less polar or nonpolar solvents such as CH would have relatively higher chemical potential (**Figure 38**). It serves as a stronger driving force for TAEA molecules to migrate from the solution phase to the MOF phase, and makes the modified MOF have a higher amine group density and a higher CO_2 uptake. Therefore, there should be a reverse relationship between solvent polarity and TAEA loading amount. Our explanation is well supported by the order of solvent polarity (CH (0.006) < THF (0.207) < DCM (0.309) < MeOH (0.762)).[78] Based on the above thermodynamic rationalization, a nonpolar solvent, like CH, is the optimal solvent for the incorporation of alkylamine into Cr-MIL-101-SO_3H.

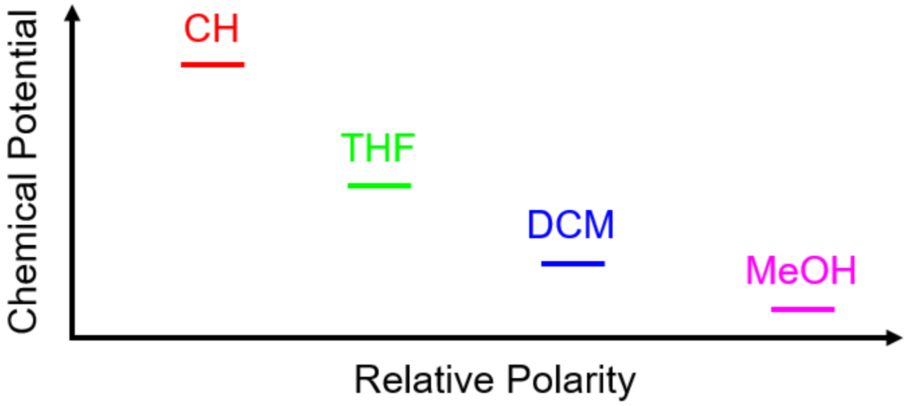

Figure 38. The illustration of the relative chemical potentials of the same alkylamine dispersed in four different solvents.

2.3.6 Optimal Amine Tethering Condition for Cr-MIL-101-SO_3H

According to the results of the above systematic study, the optimal condition to tether TAEA into Cr-MIL-101-SO_3H is to immerse the MOF in CH solution with 8 equiv. TAEA, and stir the suspension for 5 min at RT. The same procedure was also applied to other alkylamines and the gas uptakes of the resulting samples were measured (**Figure 39-41**). Cr-MIL-101-SO_3H-TAEA still excels among other alkylamine modified Cr-MIL-101-SO_3H in CO_2 uptake (**Figure 39**), which is the best CO_2 adsorbent we obtained in this systematic work so far.

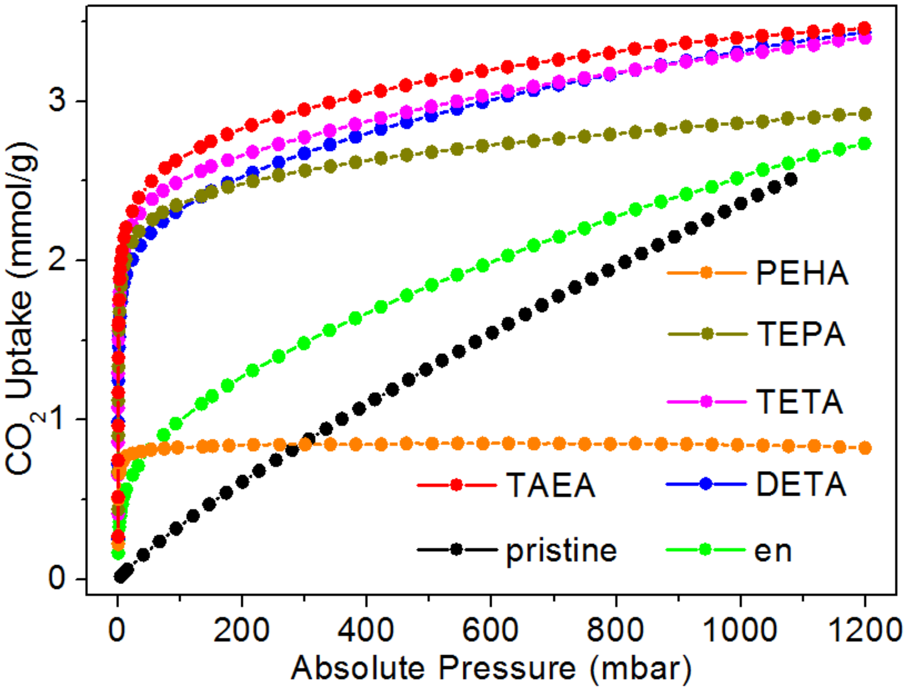

Figure 39. CO$_2$ uptakes at 20 °C of Cr-MIL-101-SO$_3$H modified with 8 equiv. different alkylamines. Control experiments were designed with alkylamine structure as the only variable. The other experimental factors are as follows: alkylamine quantity (8 equiv.), reaction time (5 min), reaction temperature (RT), and solvent (CH).

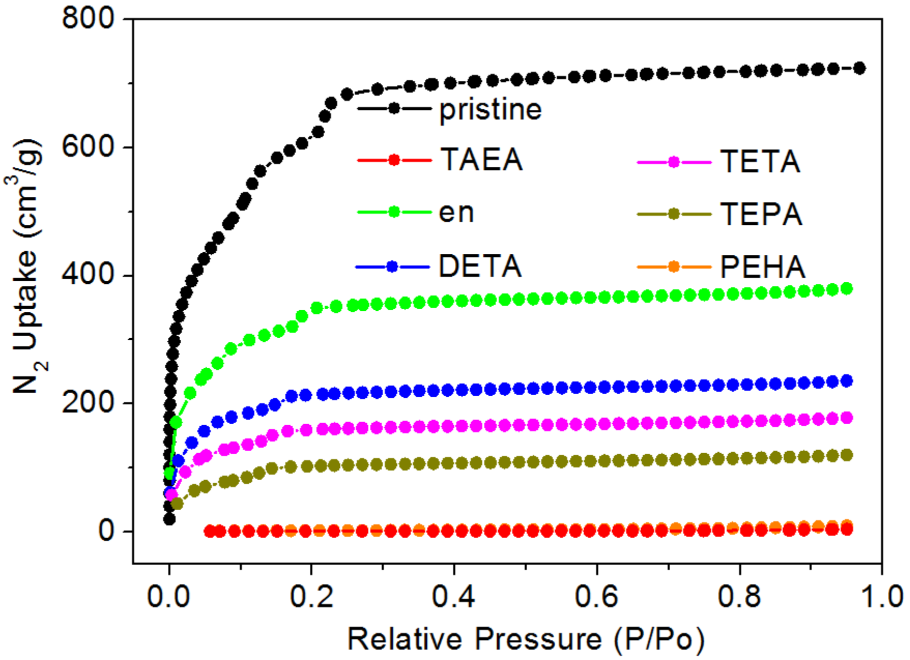

Figure 40. N_2 uptakes at 77 K of Cr-MIL-101-SO_3H modified with 8 equiv. different alkylamines. Control experiments were designed with alkylamine structure as the only variable. The other experimental factors are as follows: alkylamine quantity (8 equiv.), reaction time (5 min), reaction temperature (RT), and solvent (CH).

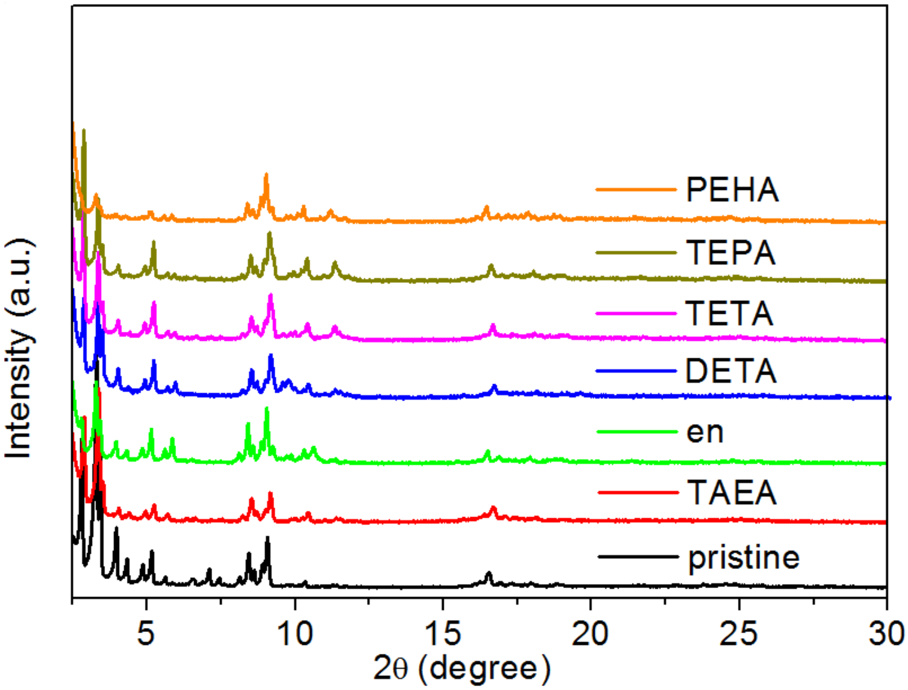

Figure 41. PXRD patterns of Cr-MIL-101-SO_3H modified with 8 equiv. different alkylamines. Control experiments were designed with alkylamine structure as the only variable. The other experimental factors are as follows: alkylamine quantity (8 equiv.), reaction time (5 min), reaction temperature (RT), and solvent (CH).

2.3.7 Isosteric Heat of Adsorption and Recyclability Test

Isosteric heat of CO_2 adsorption of Cr-MIL-101-SO_3H-TAEA was calculated based on the CO_2 uptake data collected at 0 °C, 20 °C and 40 °C (**Figure 42**) with a triple-site Langmuir model (**Equation 1-2**).

Langmuir parameters are listed as follows:

Adsorption site A:

$q_{sat,A}$ = 1.8754 mmol/g, $b_{0,A}$ = 1.8888e-17 pa^{-1}, E_A = 86.70 KJ/mol

Adsorption site B:

$q_{sat,B}$ = 0.7061 mmol/g, $b_{0,B}$ = 5,4666e-13 pa^{-1}, E_B = 48.73 KJ/mol

Adsorption site C:

$q_{sat,C}$ = 2.5056 mmol/g, $b_{0,C}$ = 1.2574e-10 pa^{-1}, E_C = 26.04 KJ/mol

The isosteric heat of CO_2 adsorption is 87 kJ/mol at zero coverage (**Figure 43**). It indicates a strong interaction between CO_2 and Cr-MIL-101-SO_3H-TAEA, which is likely to be the result of the fact that a CO_2 molecule interacts with multiple amine groups in the framework.[79] The high Q_{st} value is also consistent with its high CO_2 uptake at very low pressure. The N_2 uptakes of Cr-MIL-101-SO_3H-TAEA at 0 °C, 20 °C and 40 °C are all too low to be accurately measured, suggesting the CO_2/N_2 selectivity would be extremely high.

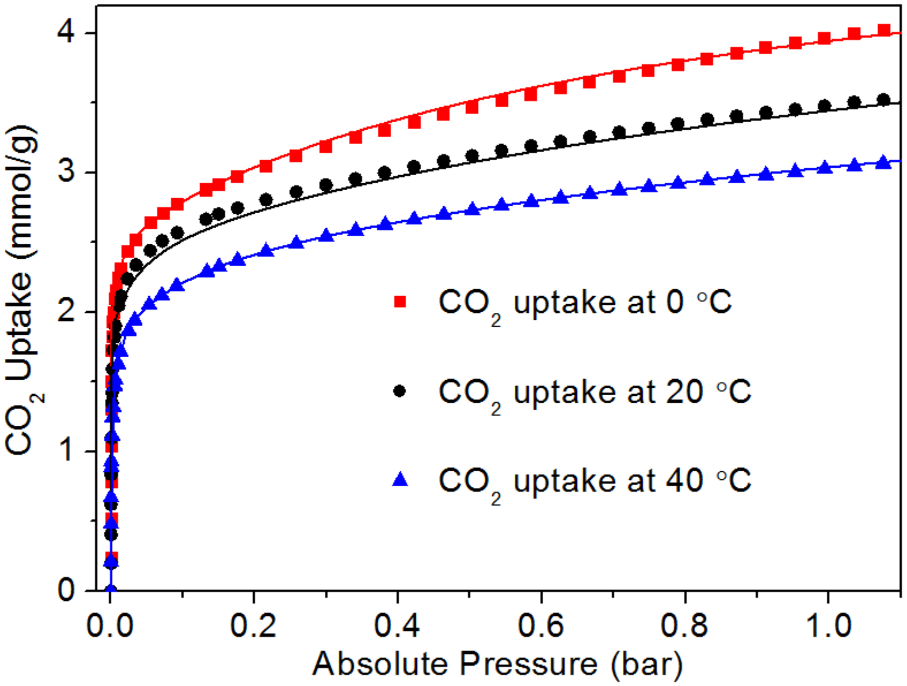

Figure 42. CO_2 adsorption isotherms at 0 °C, 20 °C and 40 °C of Cr-MIL-101-SO_3H-TAEA prepared at the optimal experimental conditions. Each isotherm has a triple-site Langmuir fitting curve.

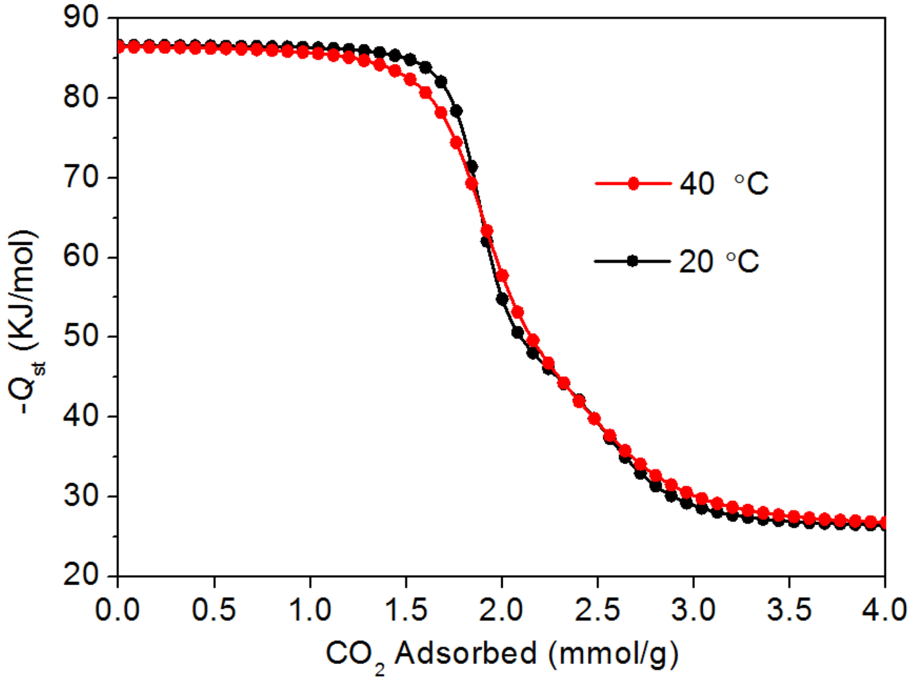

Figure 43. Isosteric heat of CO_2 adsorption at 20 °C and 40 °C of Cr-MIL-101-SO_3H-TAEA prepared at the optimal experimental conditions.

To assess Cr-MIL-101-SO_3H-TAEA as a regenerable adsorbent, we simulated temperature and vacuum swings by saturating the sample with CO_2 gas up to 150 mbar at 40 °C or 0.4 mbar at 20 °C, followed by a high vacuum for 60 min at 80 °C. After 15 cycles, there was no apparent loss in CO_2 uptake, with 2.28 mmol/g at 150 mbar and 40 °C (**Figure 44**, the condition related to CO_2 capture from flue gas), and 1.12 mmol/g at 0.4 mbar and 20 °C (**Figure 45**, the condition relevant to CO_2 capture directly from air). Therefore, it is evident that Cr-MIL-101-SO_3H-TAEA is an efficient and regenerable adsorbent with very strong affinity towards CO_2, suggesting the good potential of their applications in CO_2 capture.

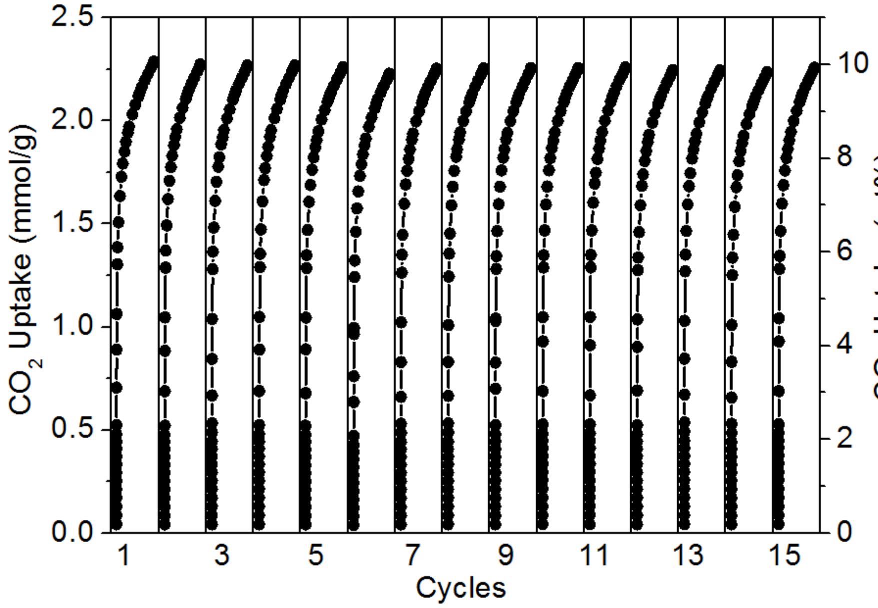

Figure 44. Fifteen cycles of CO_2 adsorption at 150 mbar and 40 °C of Cr-MIL-101-SO_3H-TAEA prepared at the optimal experimental conditions.

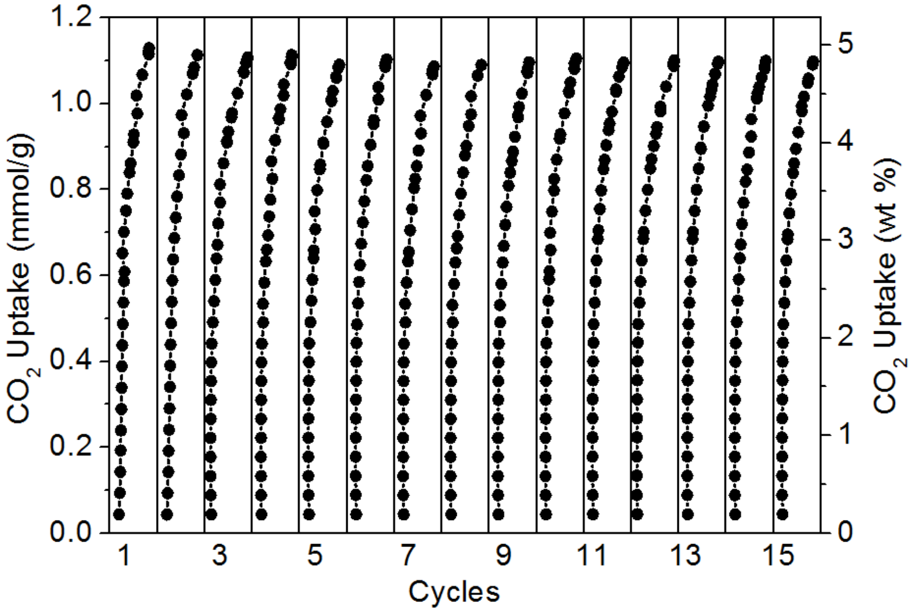

Figure 45. Fifteen cycles of CO_2 uptake at 0.4 mbar and 20 °C of Cr-MIL-101-SO_3H-TAEA prepared at the optimal experimental conditions.

2.4 Conclusion

Based on the acid-base reaction between sulfonic acid groups and amine groups, we successfully incorporated alkylamines into Cr-MIL-101-SO_3H through a fast and mild approach. We also systematically optimized the experimental factors in the amine tethering process to maximize the CO_2 uptake of the resulting adsorbent. The experimental outcomes in optimization were rationalized from a thermodynamic perspective. At the optimal amine tethering condition, the obtained Cr-MIL-101-SO_3H-TAEA has high cyclic CO_2 uptakes of 2.28 mmol/g at 150 mbar and 40 °C, and 1.12 mmol/g at 0.4 mbar and 20 °C. Beyond that, the inexpensive starting materials and simple synthetic procedure for Cr-MIL-101-SO_3H-TAEA all promise its superiority in large-scale production in real application.

CHAPTER III

THERMODYNAMICALLY DIRECTED METHOD TO TETHER ALKYLAMINE INTO METAL-ORGANIC FRAMEWORK FOR EXCEPTIONALLY HIGH CO_2 UPTAKE

3.1 Introduction

Global warming continues to be a severe environmental problem due to the increasing atmospheric CO_2 concentration,[4, 80, 81] which is mainly attributed to the combustion of fossil fuels.[1] To contain the CO_2 concentration in the atmosphere, researchers have been striving hard to develop solid adsorbents for CO_2 capture,[82-84] especially amine-functionalized solid materials.[85, 86] These materials have multiple advantages, such as strong and specific affinity towards CO_2 over other gas species, low regeneration energy for their solid nature, less corrosive effect on infrastructure, etc.[85, 86] Among them, metal-organic frameworks (MOFs), with high porosity, high surface area and tunable structure,[87, 88] stand out as a promising candidates for amine tethering. A lot of attempts have been made to explore their CO_2 capture capability.[5, 10-13, 15-20, 65, 89]

Cr-MIL-101 is a highly porous framework with two types of mesopores and large cage windows to allow the incorporation of functional species.[76] Furthermore, it can survive in many harsh chemical conditions,[72, 90-92] including highly basic alkylamine solution.[73] Therefore, Cr-MIL-101 is regarded as a good platform to conduct alkylamine tethering for CO_2 capture. In addition, the cheap starting reagents and easy synthetic procedure of Cr-MIL-101 make it facile to prepare the material in large quantities for industrial applications.[93-95] Preliminary attempts were made to tether alkylamine into Cr-

MIL-101, however, the CO_2 capacity of the obtained materials were not very impressive.[73, 96, 97] As we known, the experimental condition applied in amine-tethering procedure can significantly affect the performance of the resulting materials.[15] It encouraged us to develop a more efficient method to incorporate alkylamine into Cr-MIL-101 and improve its carbon capture capacity.

Herein, we report a thermodynamically directed method to tether alkylamine into a highly stable mesoporous MOF, Cr-MIL-101, aiming for an enhanced alkylamine loading amount and a significantly improved CO_2 uptake.

3.2 Experimental Section

3.2.1 Chemicals

Chromium (III) nitrate nonahydrate ($Cr(NO_3)_3\cdot 9H_2O$), terephthalic acid (H_2BDC), hydrofluoric acid 48-51 wt% (HF), ethanol (EtOH), ammonium fluoride (NH_4F), acetone, cyclohexane (CH), dichloromethane (DCM), diethylenetriamine (DETA), tris(2-aminoethyl)amine (TAEA), 40% w/w sodium deuteroxide (NaOD) solution in deuterium oxide (D_2O) solution(99.5%) were purchased from VWR. All commercial chemicals were used without further purification unless otherwise mentioned.

3.2.2 Instruments

Powder X-ray diffraction (PXRD) was carried out with a BRUKER D8-Focus Bragg-Brentano X-ray Powder Diffractometer equipped with a Cu sealed tube (λ = 1.54178 Å) at 40 kV and 40 mA. Images and analyses of SEM/EDX were taken by FEI Quanta 600 FE-SEM. The Quanta 600 FEG is a field emission scanning electron microscope capable of generating and collecting high-resolution and low-vacuum images.

It is equipped with a motorized x-y-z-tilt-rotate stage, providing the following movements: x = y = 150 mm (motorized); z = 65 mm (motorized); Tilt +70 degrees to –5 degrees (motorized); Source: Field emission gun assembly with Schottky emitter source. Voltage: 200 V to 30 kV. Beam Current: >100 nA. Equipment associated with the Quanta 600 includes: conventional Everhart-Thornley detector, back-scattered electron detector, IR-CCD chamber camera, Oxford EDX system equipped with X-ray mapping and digital imaging, HKL/Oxford EBSD system incl. geological phase database for phase ID, Gatan panchromatic cathodoluminescence detector with RGB filters and a Zyvex S100 nanomanipulator. N_2 and CO_2 adsorption-desorption isotherms were measured using a Micrometritics ASAP 2020 system at different temperatures. Nuclear magnetic resonance (NMR) analysis was taken by Mercury 300 (300 MHz routine walkup H/C system). Thermogravimetric analysis (TGA) were performed on Mettler Toledo TGA/DSC (DSC = Differential Scanning Calorimetry) 1 Star System. The TGA instrument is coupled with a mass spectrometer (OmniStar ThermoStar GSD320 Gas Analysis System) for the analysis of gas species.

3.2.3 Preparation of Cr-MIL-101

A mixture of $Cr(NO_3)_3.9H_2O$ (400 mg, 1.0 mmol), terephthalic acid (H_2BDC, 166 mg, 1.0 mmol), deionized water (4.75 mL), and HF (48-51 wt%, 20 µL) was added into a 5 mL autoclave and heated at 200 °C for 8 h.[72] After the mixture was cooled to room temperature (RT), the as-synthesized solid was washed successively with 100 mL 95:5 EtOH:H_2O (v/v) solution at 80 °C for 24 h, 90 mL 30 mmol/L NH_4F solution at 70 °C for 24 h, and 67 mL deionized water at 90 °C for 3h.. The resulting solid was further washed with acetone for three times and desiccated in air, before being activated at 160 °C for 12h under vacuum prior to further use.

3.2.4 Preparation of Alkylamine Modified Cr-MIL-101

Two different methods were employed to incorporate alkylamine into Cr-MIL-101 with solvent as the main discrepancy, detailed below.

Method A: Activated Cr-MIL-101 (100 mg, 0.146 mmol) was added to an alkylamine (1.11 mmol) solution in anhydrous dichloromethane (DCM, 8 mL). The suspension was stirred at RT for 24 h. The resulting solid was washed with anhydrous DCM for three times and desiccated under a Schlenk line.

Method B: Activated Cr-MIL-101 (100 mg, 0.146 mmol) was added to an alkylamine (1.11 mmol) solution in anhydrous cyclohexane (CH, 8 mL).The suspension was stirred at RT for 5 min. The resulting solid was washed with anhydrous CH for three times, and desiccated under a Schlenk line.

Sample 1 and **2** were prepared according to **Method A** using diethylenetriamine (DETA) and tris(2-aminoethyl)amine (TAEA) as alkylamine, respectively, and were activated at 60 °C. **Sample 3** and **4** were prepared according to **Method B** using DETA and TAEA as the alkylamine, respectively, and were activated at 55 °C.

3.2.5 Gas Sorption Measurement of Alkylamine-Modified Cr-MIL-101

The gas sorption isotherms were collected using Micrometritics ASAP 2020 system. N_2 uptakes were measured at 77 K, while CO_2 uptakes were measured at 0 °C, 25 °C, and 40 °C.

3.2.6 PXRD Measurement of Alkylamine-Modified Cr-MIL-101

The PXRD patterns of the samples were collected using a BRUKER D8-Focus Bragg-Brentano X-ray Powder Diffractometer equipped with a Cu sealed tube (λ = 1.54178 Å) at 40 kV and 40 mA. The ranges of 2θ are all set to be 2-35 degree.

3.2.7 EDX Measurement of Alkylamine-Modified Cr-MIL-101

The sample was first desiccated to remove moisture or solvent residues. After that, it is finely ground before being applied on a conductive tape which is adhered to the EDX sample holder. After the sample was placed into the SEM/EDX instrument, the inner pressure was decreased below 10^{-6} torr before measurements were conducted. The scanning areas were all set to be approximately 40×40 μm^2 to detect the element species.

3.2.8 Quantitative Analysis of the Organic Components in Alkylamine-Modified Cr-MIL-101 Using NMR

10 mg activated alkylamine-modified Cr-MIL-101 sample was added to a solution prepared from 200 μL 40% w/w NaOD solution in D_2O (99.5%) and 1200 μL D_2O for decomposition. After 24 h, the suspension became clear pale green solution, which was analyzed using NMR spectroscopy for the molar ratio between BDC and TAEA in the sample.

3.2.9 TGA Measurement of Alkylamine-Modified Cr-MIL-101

The sample (around 10 mg) was placed in an aluminum pan, and kept under helium at 30 °C for 15 min to remove solvent residues. After that, the TGA measurement was initiated with the increasing rate of temperature set as 5 °C/min. The emitted gas species were detected using an OmniStar ThermoStar GSD320 Gas Analysis System

The recyclability of the sample was also performed with TGA. About 13 mg sample was loaded into the aluminum pan. In the preparation step, the sample was maintained in a He flow at 40 °C for 10 min before being heated to 70 °C to remove the remaining solvent or moisture. After 10 min, the temperature was lowered back to 40 °C and also held for 10 min before the recyclability test. In each cycle, the adsorption condition was 40 °C with a gas flow of 15% CO_2 and 85% He, while the desorption condition was 90 °C with a pure He flow. The adsorption and desorption time were set to be 30 min and 10 min, respectively. After each cycle, the sample was maintained in a He flow at 40 °C for 10 min before the next cycle.

3.2.10 Dynamic Column Breakthrough Experiments*

Dynamic column breakthrough experiments (**Figure 46**) were carried out using a home-built setup coupled with a mass spectrometer (Hiden QGA).[98, 99] Dry MOF powders (0.2-0.4 g for 7 cm column) were packed into a stainless-steel column (diameter: 0.46 cm). The packed column was purged under a constant He flow (8± 0.5 mL min^{-1}) before experiments. CO_2/N_2 [(15±1)/(85±1)] binary mixture gas with a flow rate of 9.5 ± 0.5 cc min^{-1} was introduced through the by-pass line with a resistance (controlled by a needle valve) comparable to the pressure drop (0-0.2 bar) to calibrate the system dead volume. After that, a helium flow (8± 0.5 mL min^{-1}) was introduced to clean the whole system. Breakthrough experiments were initiated by switching the purge gas (He) to CO_2/N_2 binary mixture gas [(15±1)/(85±1) composition, 9.5 ± 0.5 cc min^{-1}, stabilized for 30 min

---

* The breakthrough experiment was performed by Dr. Zhigang Hu and Prof. Dr. Dan Zhao of the Department of Chemical and Biomolecular Engineering in National University of Singapore.

in advance]. An argon flow was kept at 5 cc min^{-1} during the experiments as an internal reference gas to calibrate the flow rate of exit gas. The upstream and downstream pressures were recorded by pressure gauges. The original breakthrough curves were obtained as a relative $CO_2/N_2/Ar$ composition versus elapse time and then converted to molar faction ratio versus elapse time.[10, 16, 100]

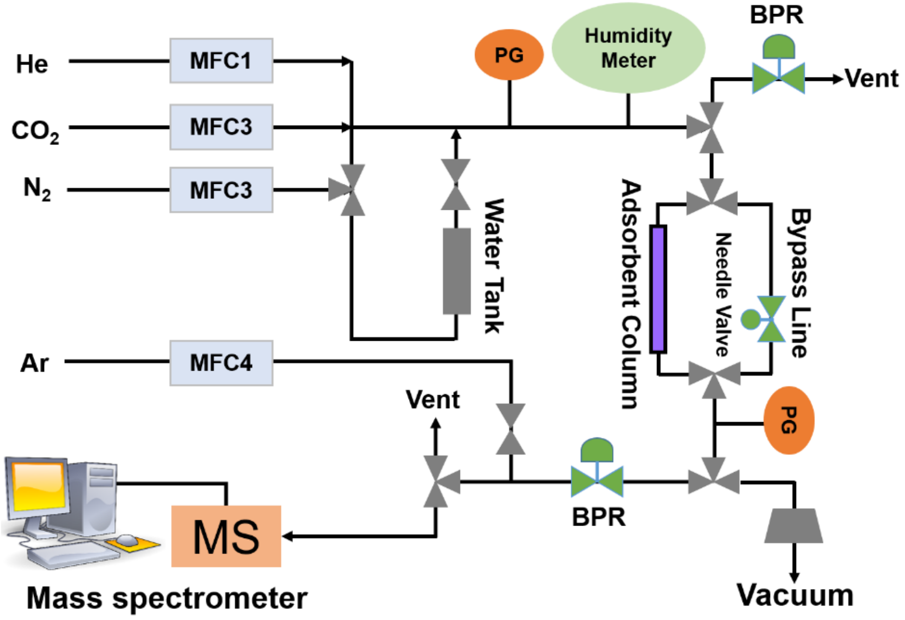

Figure 46. The layout of the home-built breakthrough equipment.

3.2.11 Selectivity Calculation Based on Breakthrough Experiment Data*

The simplified model for breakthrough related calculations is presented in **Figure 47**.

---

* The selectivity calculation based on breakthrough experiment data was performed by Dr. Zhigang Hu and Prof. Dr. Dan Zhao of the Department of Chemical and Biomolecular Engineering in National University of Singapore.

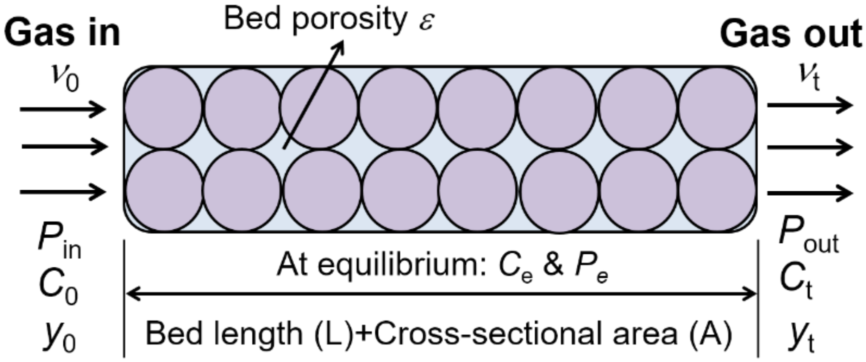

Figure 47. Model and parameters for adsorptive separation calculations.

From the mass balance across the whole packed column ($In\text{-}Out = Accumulation$), the following equations can be obtained:

$$\varepsilon v_0 C_0 A t_c - \int_0^{t_c} \varepsilon v_t C_t A dt = LA\varepsilon C_e + LA(1-\varepsilon)q_e$$

(Equation 4)

$$C_0 = \frac{P_{in}}{R \times T}; C_t = \frac{P_{out}}{R \times T}$$

(Equation 5)

Where ε is the bed porosity, v_o is the interstitial feed gas velocity (cm s^{-1}), C_0 is the inlet gas concentration (mmol cm^{-3}), A is the cross sectional area of column (cm^2), t_c is the elution time (s), v_t is the interstitial outlet gas velocity (cm s^{-1}), C_t is the outlet gas concentration (mmol cm^{-3}), C_e is the average gas concentration at adsorption equilibrium (mmol cm^{-3}), P_{in} and P_{out}, and P_e are the inlet (upstream), outlet (downstream), and equilibrium pressure (assume an average value of upstream and downstream pressure), respectively, L is the column length (cm), r_p is the radius of crystal size; q_e is the equilibrium concentration of adsorbate in the adsorbent (mmol cm^{-3}).[98, 101, 102]

According to Darcy's Law, the cross-column pressure drop is related to the viscosity of gas phase (μ), interstitial gas velocity and column length:

$$\frac{\Delta P}{L}=\frac{150}{4r_p^2}(\frac{1\text{-}\varepsilon}{\varepsilon})^2\mu v_{\mathrm{t}}$$

(Equation 6)

Since the product of viscosity of gas phase (μ), interstitial gas velocity (v_t) can be deemed as a constant, it is reasonable to assume the equilibrium pressure (P_e) equals to:

$$P_e \approx \frac{P_{in}+P_{out}}{2};\ C_e \approx \frac{P_{in}+P_{out}}{2R\times T}$$

(Equation 7)

After rearrangement, the **Equation 4** for mean residence time $\bar{t}$ is obtained:

$$\int_0^{t_C}\left(1-\frac{v_tC_t}{v_0C_0}\right)dt=\bar{t}=\frac{L}{v_0}\left[\frac{P_{in}+P_{out}}{2P_{in}}+\frac{1-\varepsilon}{\varepsilon}\left(\frac{q_e}{C_0}\right)\right]$$

(Equation 8)

For each component, y_0 and y_t represent the inlet and outlet molar faction:

$$y_0=y_t^{\infty};\ v_0=v_t^{\infty}\times\frac{P_{out}}{P_{in}};\ \frac{v_t}{v_0}=\frac{v_t}{v_t^{\infty}}\times\frac{P_{in}}{P_{out}}$$
$$\frac{C_t}{C_0}=(\frac{y_tP_{out}}{R\times T})/(\frac{y_0P_{in}}{R\times T})=\frac{y_t}{y_0}\times\frac{P_{out}}{P_{in}};$$
$$\frac{C_t}{C_0}\times\frac{v_t}{v_0}=\frac{v_ty_t}{v_t^{\infty}y_t^{\infty}}$$

(Equation 9)

The following equation can be obtained:

$$\int_0^{t_C}\left(1-\frac{v_ty_t}{v_t^{\infty}y_t^{\infty}}\right)dt=\bar{t}=\frac{L}{v_0}\left[\frac{P_{in}+P_{out}}{2P_{in}}+\frac{1-\varepsilon}{\varepsilon}\left(\frac{q_e}{C_0}\right)\right]$$

(Equation 10)

The mean residence time obtained from the experimentally measured breakthrough responses after subtracting blank residence time (dead volume calibration) can be used to calculated q_e/C_0. The adsorption selectivity (S_{ads}) at equilibrium pressure can be calculated:

$$S_{\text{ads}} = \frac{(q_e / C_0)_{CO_2}}{(q_e / C_0)_{N_2}}$$

(Equation 11)

3.3 Results and Discussion

3.3.1 CO_2 Uptakes and Pore Volumes of the Alkylamine-Modified MOFs

The CO_2 uptakes of **Sample 1, 2, 3** and **4** were measured at 25 °C to evaluate their CO_2 capture abilities. (**Figure 48**) Their significantly different performance reveals the chemistry involved in the amine tethering process. Compare the samples prepared with the same method (**Sample 1, 2** and **Sample 3, 4**), the CO_2 uptake of TAEA-modified Cr-MIL-101 at 150 mbar is approximately 10% higher than that of DETA-tethered one in both sets of the data. (**Table 29**) This suggests that TAEA is able to endow Cr-MIL-101 with a stronger affinity towards CO_2 than DETA, which might be ascribed to the higher number of amine groups in a TAEA molecule. By contrast, the samples prepared with the same alkylamine but different methods (**Sample 1, 3** and **Sample 2, 4**) display remarkably distinct CO_2 adsorption behaviors. The CO_2 uptakes of **Sample 3** and **4** at 150 mbar are more than twice as much as those of **Sample 1** and **2**, respectively. This strongly indicates that solvent is a more crucial experimental factor in determining the CO_2 capture performance of the alkylamine-modified MOFs.

Judging from the pore size distribution diagrams of the four samples derived from their N_2 adsorption isotherms at 77 K (**Figure 49-53**), the size and population of mesopores in the frameworks considerably decrease after alkylamine incorporation. Since their PXRD patterns remain unchanged compared with that of the pristine Cr-MIL-101 (**Figure 54**), the possibility of phase change or structural collapse of the MOFs is eliminated. Therefore, the reduction in mesopores is mainly attributed to the incorporation of alkylamine into the frameworks.

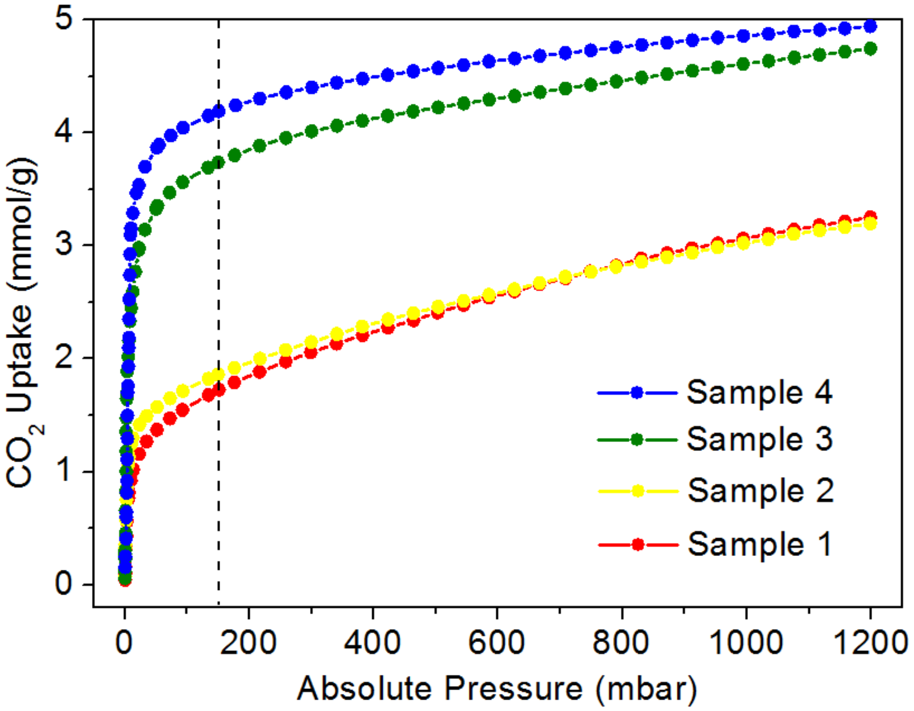

Figure 48. CO_2 uptakes at 25 °C of **Sample 1-4**.

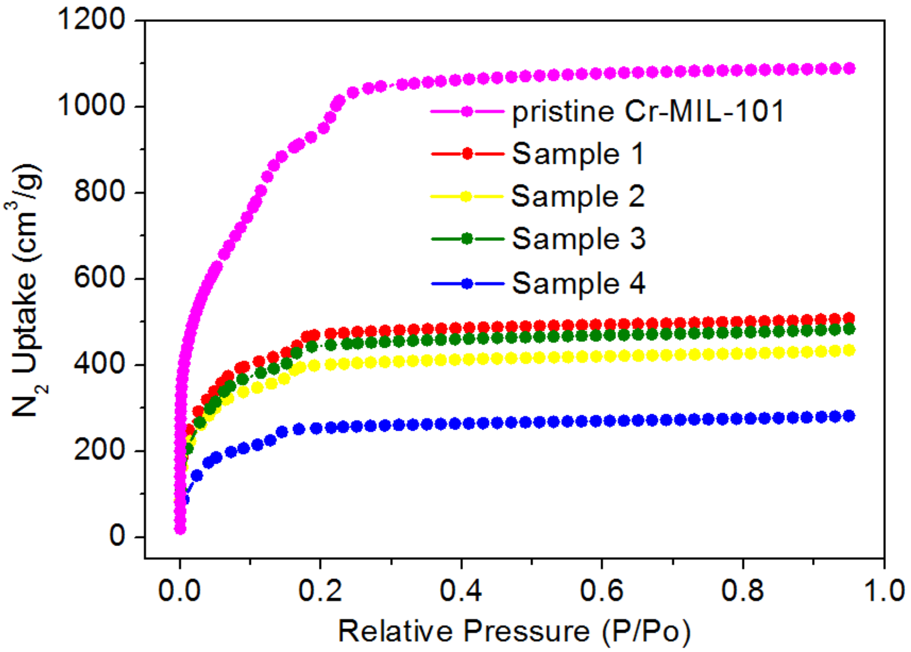

Figure 49. N_2 uptakes at 77 K of **Sample 1-4** in comparison with that of the pristine Cr-MIL-101.

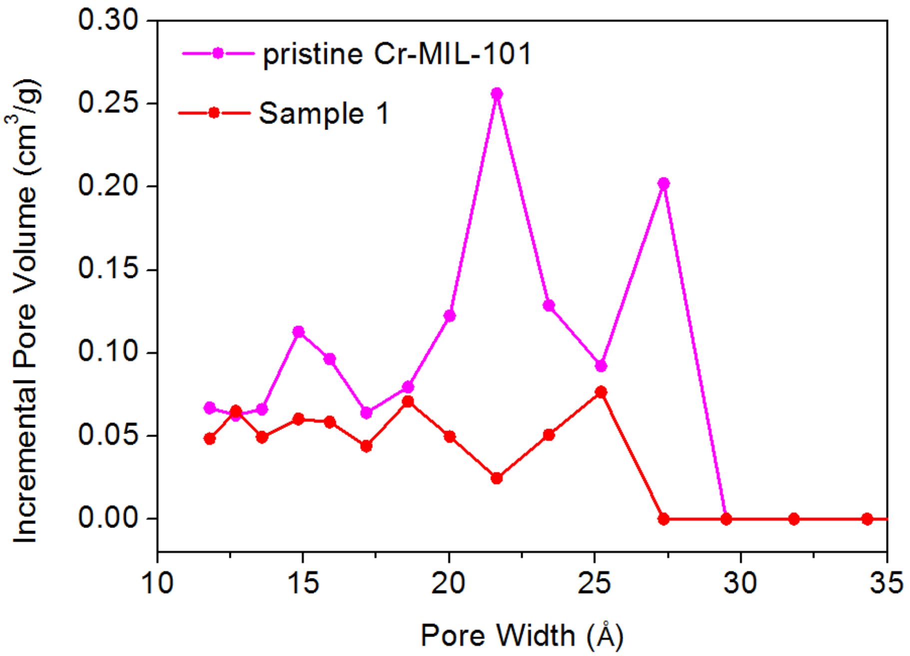

Figure 50. Pore size distribution of **Sample 1** in comparison with that of the pristine Cr-MIL-101.The total pore volume in **Sample 1** (<= 272.71 Å) is determined to be 0.67651 cm^3/g.

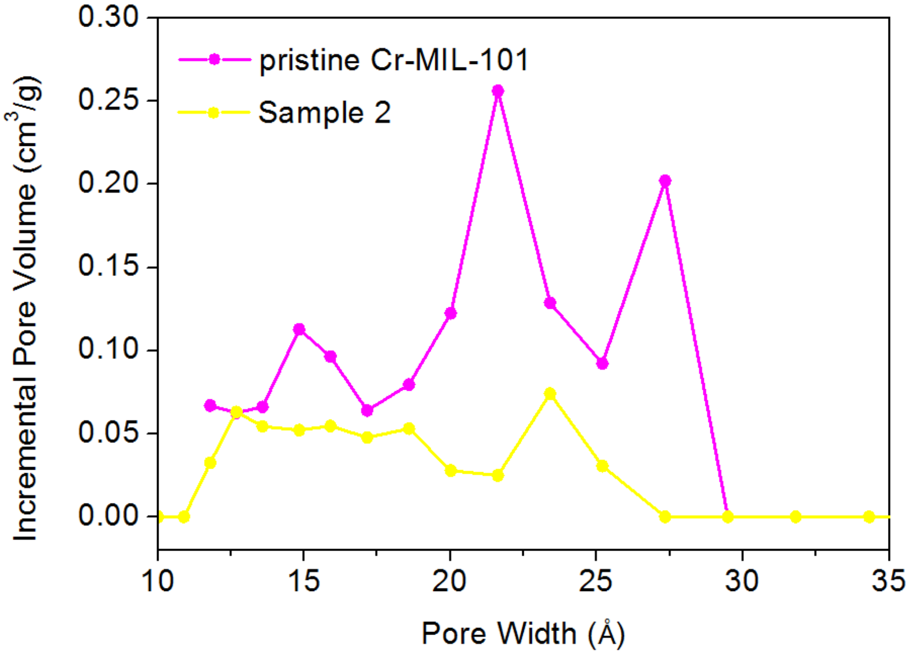

Figure 51. Pore size distribution of **Sample 2** in comparison with that of the pristine Cr-MIL-101.The total pore volume in **Sample 2** (<= 272.71 Å) is determined to be 0.57573 cm^3/g.

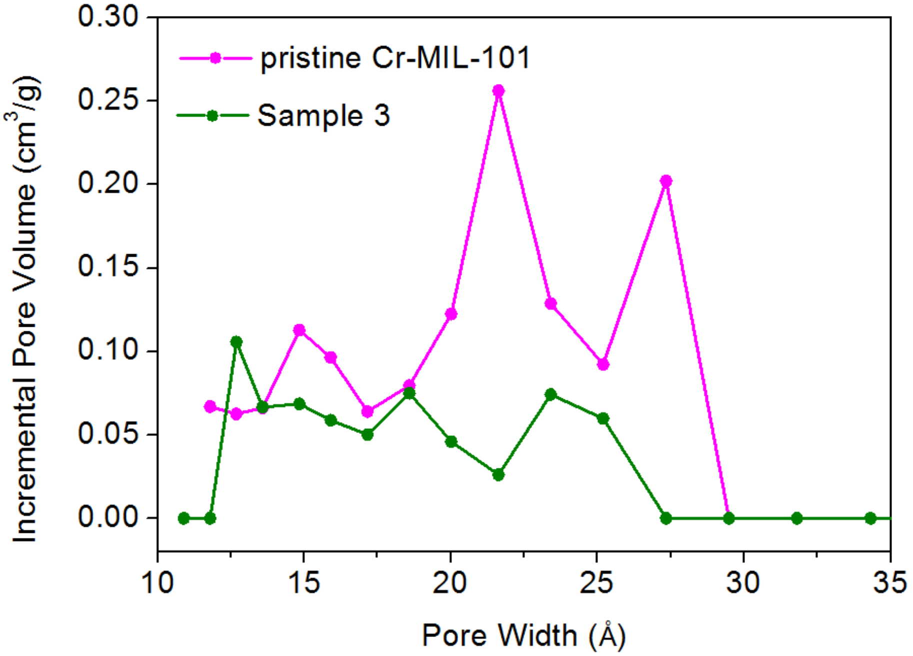

Figure 52. Pore size distribution of **Sample 3** in comparison with that of the pristine Cr-MIL-101.The total pore volume in **Sample 3** (<= 272.71 Å) is determined to be 0.64595 cm^3/g.

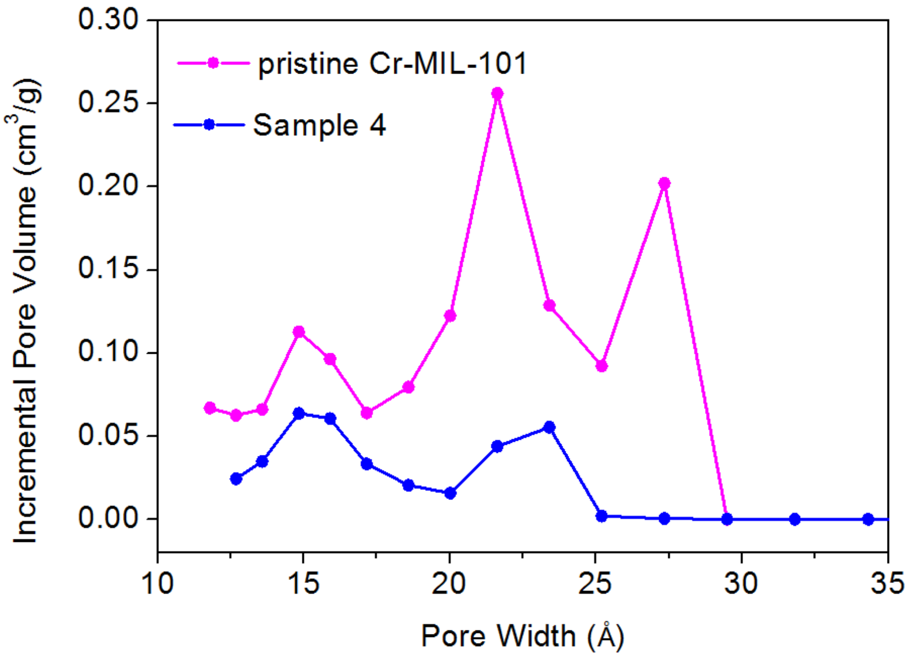

Figure 53. Pore size distribution of **Sample 4** in comparison with that of the pristine Cr-MIL-101.The total pore volume in **Sample 4** (<= 272.71 Å) is determined to be 0.35535 cm^3/g.

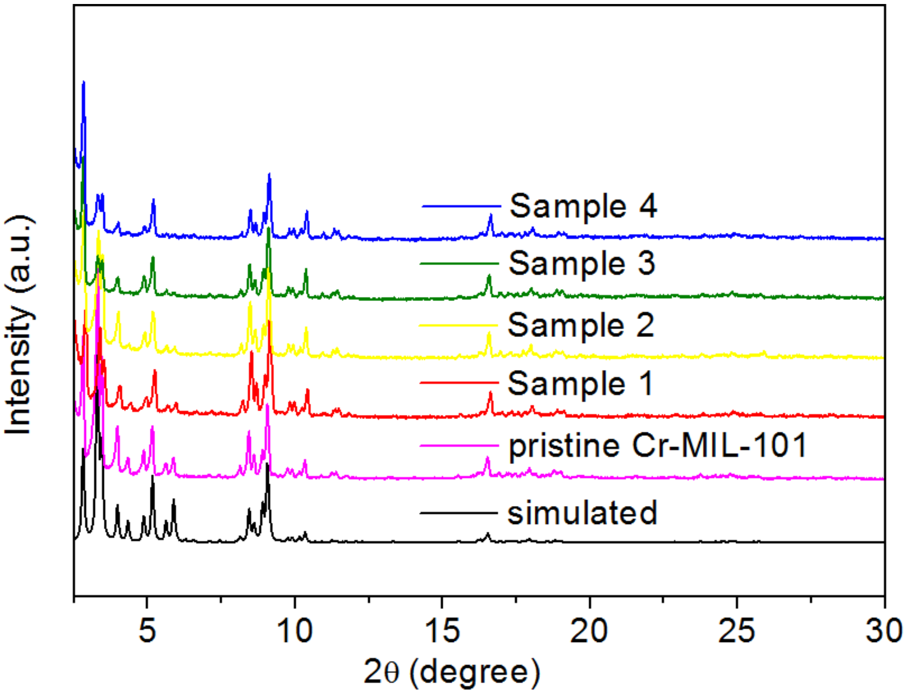

Figure 54. Comparison of the PXRD patterns of **Sample 1-4** with that of pristine Cr-MIL-101 and the simulated pattern.

3.3.2 Thermodynamic Equilibrium in Alkylamine Incorporation

To investigate why solvent is remarkably influential in the CO_2 capture behaviors of the generated samples, it is essential to discern whether the question is thermodynamic- or kinetic-related.

In **Method A**, the reaction time is 24 h, which is sufficiently long for the system to reach its equilibrium. By contrast, the reaction time in **Method B** is 5 min, which is comparatively inadequate to arrive at a similar solid conclusion. To clarify this point, control experiments were conducted by extending the reaction time in **Method B** to 30 min while still utilizing DETA (**Sample 5**) and TAEA (**Sample 6**) as the integrating alkylamines. It turns out that both the CO_2 and N_2 adsorption isotherms of **Sample 5** nearly overlap those of **Sample 3**. The same result also occurs in the comparison of **Sample 6** and **Sample 4** (**Figure 55-59**). The above outcomes strongly demonstrate that the equilibria of the corresponding systems were also attained when the samples were produced with **Method B**. As a result, the effect of solvent should be rationalized from a thermodynamic prospective.

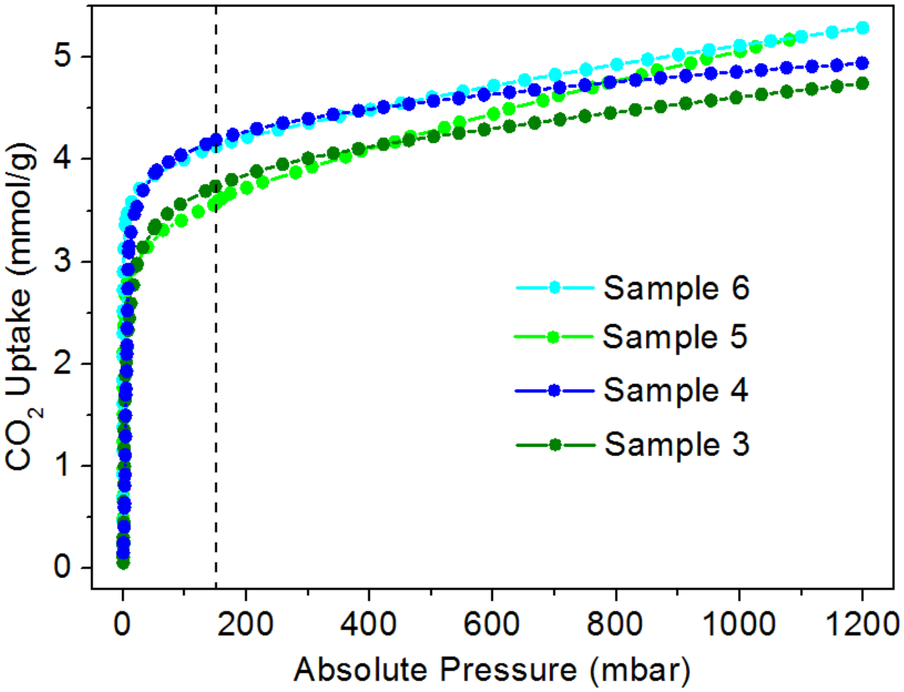

Figure 55. CO_2 uptakes at 25 °C of **Sample 3-6**.

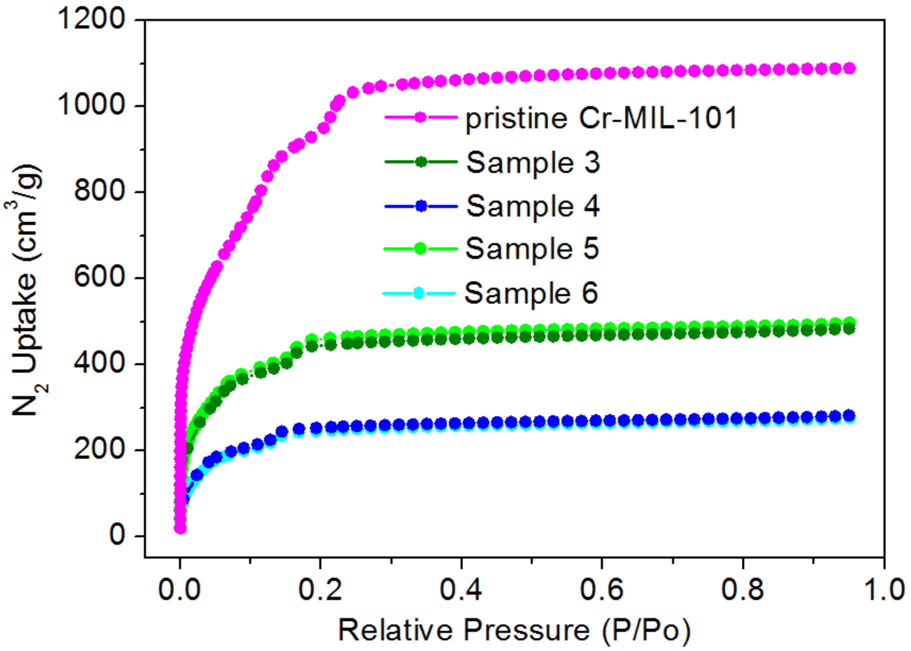

Figure 56. N_2 uptakes at 77 K of **Sample 3-6** in comparison with that of the pristine Cr-MIL-101.

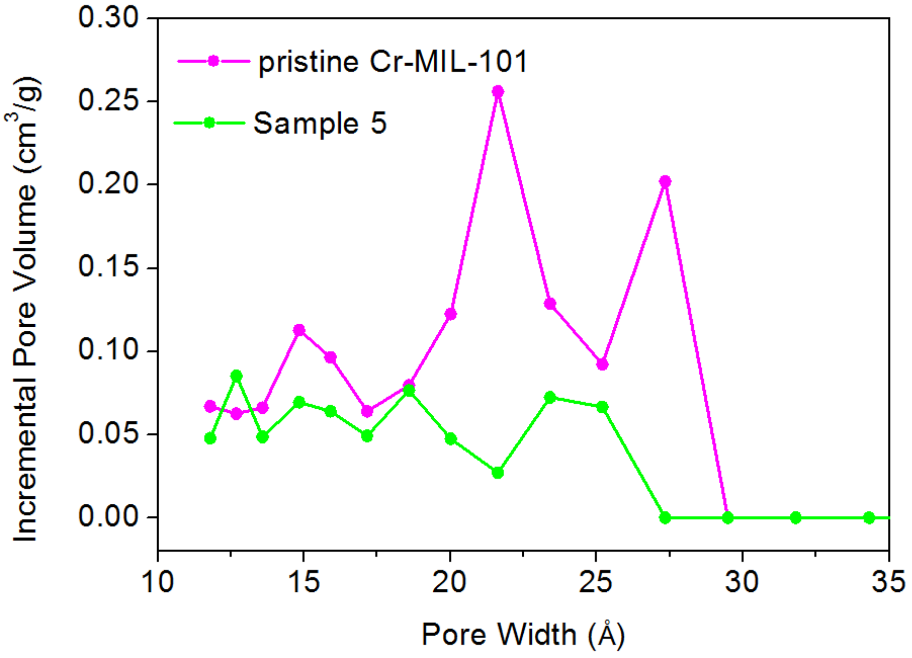

Figure 57. Pore size distribution of **Sample 5** in comparison with that of the pristine Cr-MIL-101.The total pore volume in **Sample 5** (<= 272.71 Å) is determined to be 0.66322 cm^3/g.

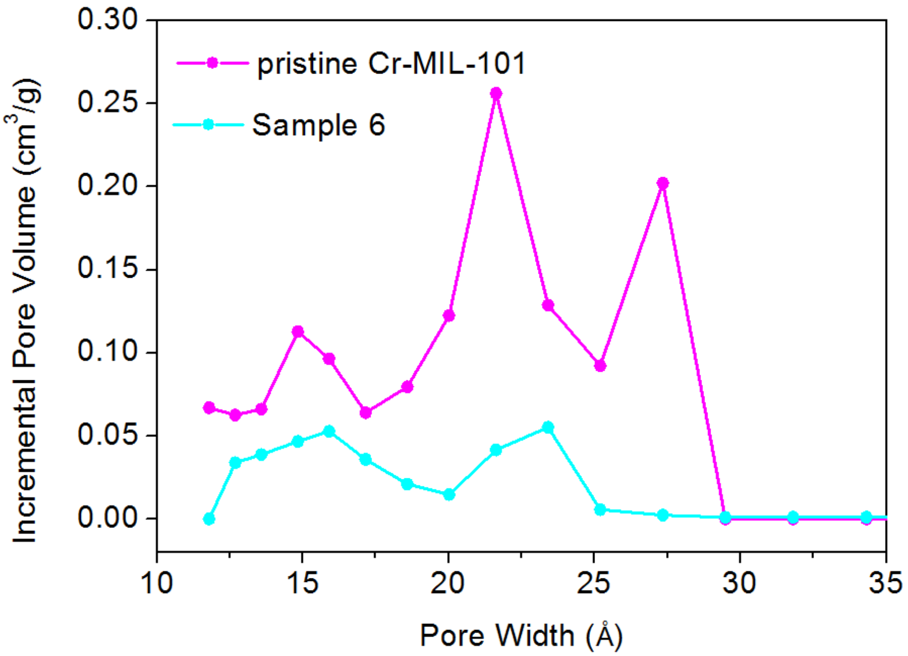

Figure 58. Pore size distribution of **Sample 6** in comparison with that of the pristine Cr-MIL-101.The total pore volume in **Sample 6** (<= 216.60 Å) is determined to be 0.36741 cm^3/g.

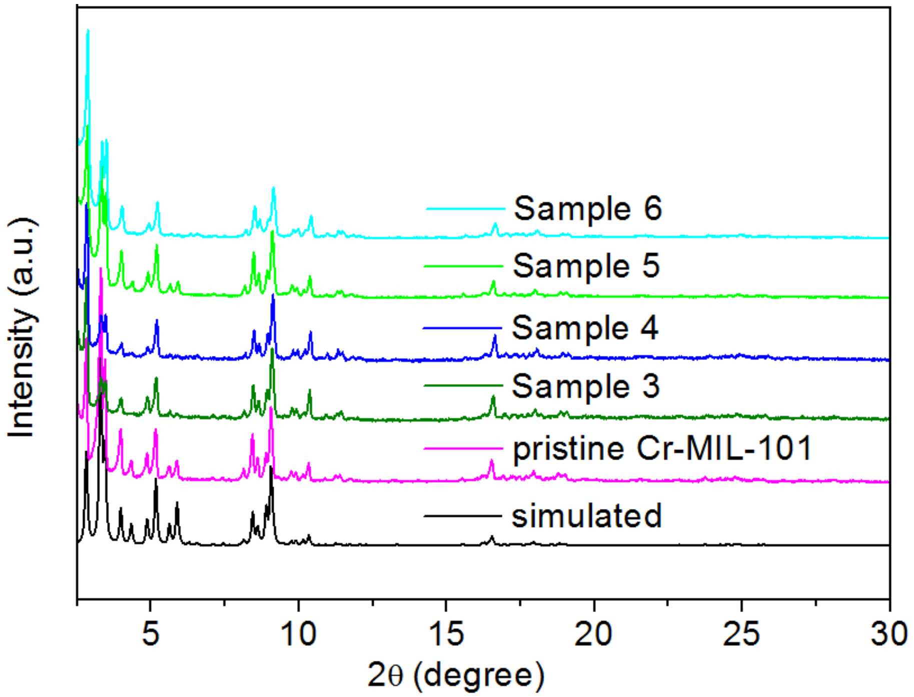

Figure 59. Comparison of the PXRD patterns of **Sample 3-6** with that of pristine Cr-MIL-101 and the simulated pattern.

We propose the polarity of solvent is the essential property that affects the loading amount of alkylamine and consequently the CO_2 uptake of the modified MOF. Compared with DCM, CH is far less polar. Accordingly it has relatively weaker interaction with the alkylamine molecules dispersed in it. This gives rise to a higher chemical potential of the alkylamine in CH than that in DCM. Thermodynamically speaking, the higher chemical potential acts as a stronger driving force for more alkylamine molecules to migrate into the framework from the solution.

The point stated above can also be reasoned in the following way. Assume there are two Cr-MIL-101 samples with equal mass. Alkylamine incorporation are conducted with these two samples using CH and DCM as the solvent, respectively. For easy comparison, we suppose there are equal amounts of a certain alkylamine molecule integrated into these two sample. Thus, the chemical potentials of alkylamine in the both MOFs are the same, denoted as μ_{MOF}. When a thermodynamic equilibrium is reached between the solution phase and the MOF phase, the chemical potential of alkylamine in the solution $\mu_{c,\,solvent}$ should be equal to that in the MOF μ_{MOF}.

$\mu_{c,\,CH} = \mu_{c,\,CH}° + RTln(c_{CH}/c°) = \mu_{MOF}$ **(Equation 12)**

$\mu_{c,\,DCM} = \mu_{c,\,DCM}° + RTln(c_{DCM}/c°) = \mu_{MOF}$ **(Equation 13)**

$\mu_{c,\,solvent}°$ is the standard chemical potential of alkylamine in the solvent. $c_{solvent}$ is the molar concentration of alkylamine in the solvent. c° is the standard molar concentration.

Therefore we have,

$\mu_{c,\,CH}° + RT°ln(c_{CH}/c°) = \mu_{c,\,DCM}° + RT°ln(c_{DCM}/c°)$

So we have,

$c_{CH}/c_{DCM} = exp[(\mu_{c,\,DCM}° - \mu_{c,\,CH}°)/RT]$ **(Equation 14)**

Since $\mu_{c,\,DCM}° - \mu_{c,\,CH}° < 0$,

Thus, $c_{CH}/c_{DCM} < 1$.

This indicates that the c_{CH} required to incorporate a certain amount of alkylamine into Cr-MIL-101 is less than c_{DCM}. Considering the premise that equal quantity of alkylamine is put into the two MOFs, it is obvious that a higher percentage of alkylamine migrate into the framework, suggesting the beneficial role of the less polar CH in driving more alkylamine molecules into the MOF.

Due to the fact that mesopores still exist in **Sample 1-4** after alkylamine incorporation in Cr-MIL-101, internal space is not a limiting factor in their CO_2 adsorption amounts. Instead, the quantity of the integrated alkylamine determines their CO_2 affinities and thus CO_2 uptakes. Therefore, solvents with smaller polarities are more favorable for the inclusion of alkylamine into MOFs and contribute to MOFs with higher CO_2 capacities (**Figure 60**).

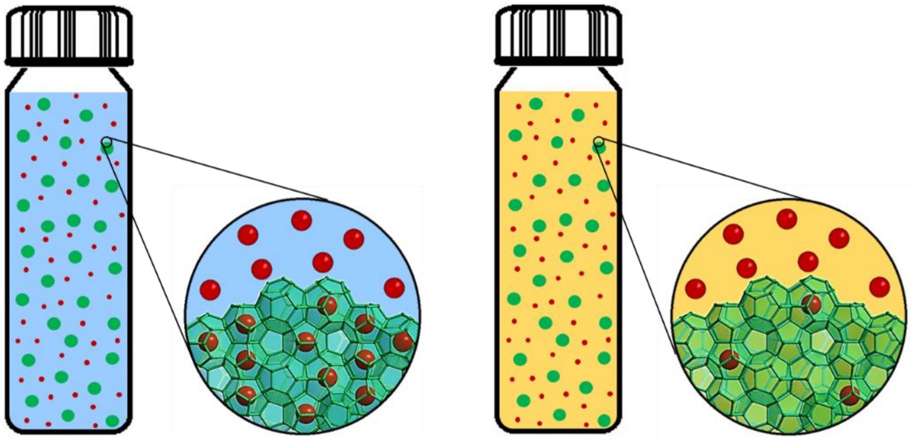

Figure 60. Illustration of the different alkylamine loading amounts in the MOF samples prepared in CH (left) and DCM (right). Cr-MIL-101 is represented with green balls and green networks. Red balls represent alkylamine molecules. Blue and yellow liquids stand for CH and DCM, respectively.

Our explanation is well supported by two classes of experimental evidences. First, the amount of integrated alkylamines is quantified by combining the results from elemental analysis (N/F ratio, **Table 10-11**) and energy dispersive X-ray spectroscopy (F/Cr ratio, **Figure 61-84** and **Table 12-27**), as indicated by N/Cr ratio (**Table 28**). It turns out that MOFs prepared in CH have higher N/Cr values than that in DCM. Moreover, the CO_2 uptakes of these materials are positively correlated to their N/Cr ratios (**Table 29**), well substantiating our rationalization. Second, the quantity of incorporated alkylamine can also be represented the pore volume of the modified MOFs. Because the framework remain robust during the modification, a low value in pore volume suggests a high loading amount. As shown in **Table 29**, the CO_2 adsorption amounts of these MOFs are negatively correlated to their pore volumes, which is harmoniously consistent with our reasoning as well.

Table 10. EA data of **Sample 1-4**. Each sample was measured twice.

Sample	C weight%	H weight%	N weight%	F weight%
Sample 1	37.35	5.61	8.93	1.68
	37.54	5.61	9.01	1.59
Sample 2	38.27	6.29	10.84	1.30
	38.15	6.18	10.75	1.21
Sample 3	40.22	5.77	11.78	1.28
	40.03	5.77	11.72	1.22
Sample 4	40.64	6.22	14.56	1.10
	40.46	6.16	14.49	1.07

Table 11. Average N weight%, average F weight% and the calculated N/F atomic ratios of **Sample 1-4**.

Sample	Average N weight%	Average F weight%	N/F atomic ratio
Sample 1	8.97	1.64	7.42
Sample 2	10.80	1.26	11.63
Sample 3	11.75	1.25	12.76
Sample 4	14.52	1.08	18.25

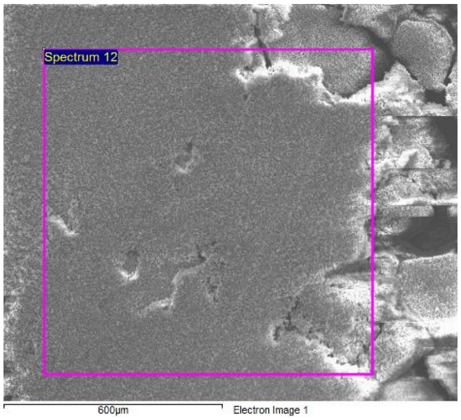

Figure 61. SEM image of **Sample 1** (1st measurement).

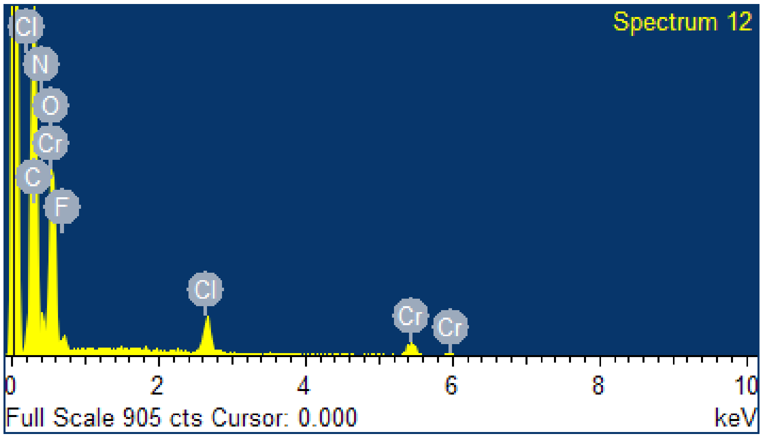

Figure 62. EDX spectrum of **Sample 1** (1st measurement).

Table 12. EDX data for **Sample 1** (1st measurement).

Element	Weight%	Atomic%
C K	40.05	56.55
N K	8.15	9.87
O K	19.55	20.72
F K	3.12	2.78
Cl K	3.83	1.83
Cr L	25.31	8.26
Totals	100.00	

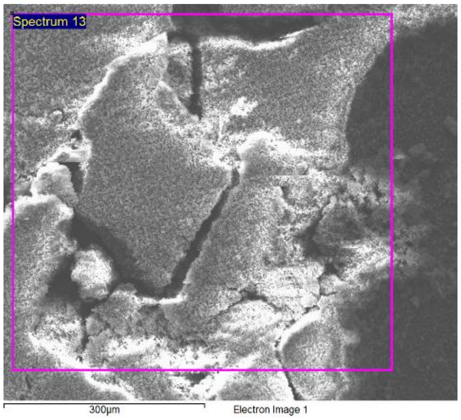

Figure 63. SEM image of **Sample 1** (2nd measurement).

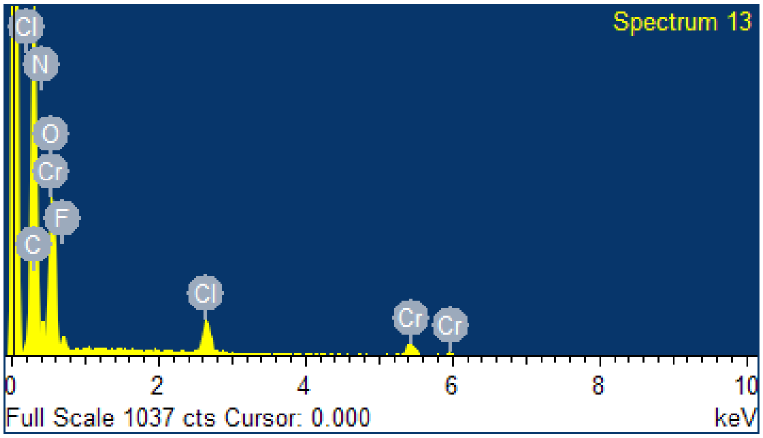

Figure 64. EDX spectrum of **Sample 1** (2nd measurement).

Table 13. EDX data for **Sample 1** (2nd measurement).

Element	Weight%	Atomic%
C K	41.97	57.99
N K	8.10	9.60
O K	20.05	20.80
F K	2.69	2.35
Cl K	3.97	1.86
Cr L	23.22	7.41
Totals	100.00	

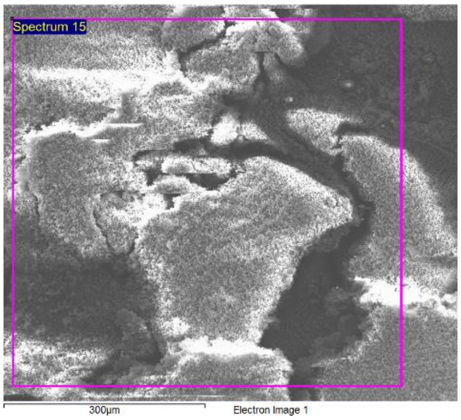

Figure 65. SEM image of **Sample 1** (3rd measurement).

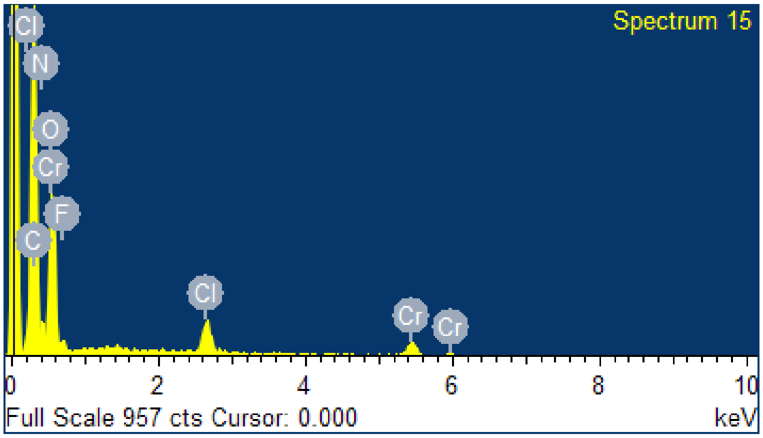

Figure 66. EDX spectrum of **Sample 1** (3rd measurement).

Table 14. EDX data for **Sample 1** (3rd measurement).

Element	Weight%	Atomic%
C K	43.34	58.61
N K	7.73	8.96
O K	21.39	21.71
F K	2.80	2.39
Cl K	4.09	1.87
Cr L	20.65	6.45
Totals	100.00	

Table 15. Summary of the EDX data of **Sample 1**.

	F atomic%	Cr atomic%
1st measurement	2.78	8.26
2nd measurement	2.35	7.41
3rd measurement	2.39	6.45
Average	2.51	7.37

F/Cr molar ratio = F Atomic% / Cr Atomic% = 2.51% / 7.37% = 0.340

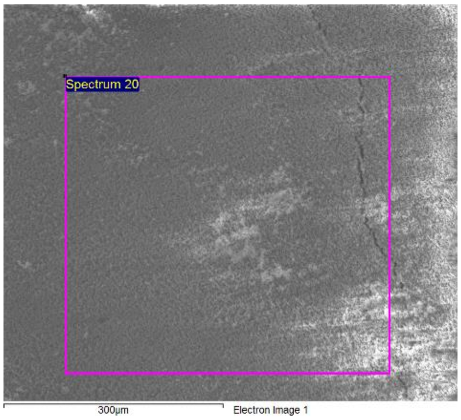

Figure 67. SEM image of **Sample 2** (1st measurement).

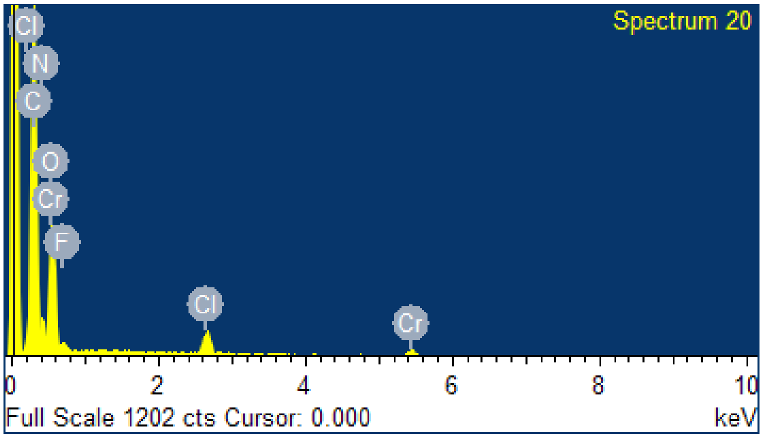

Figure 68. EDX spectrum of **Sample 2** (1st measurement).

Table 16. EDX data for **Sample 2** (1st measurement).

Element	Weight%	Atomic%
C K	43.37	58.72
N K	10.50	12.19
O K	18.30	18.60
F K	2.47	2.11
Cl K	3.03	1.39
Cr L	22.33	6.98
Totals	100.00	

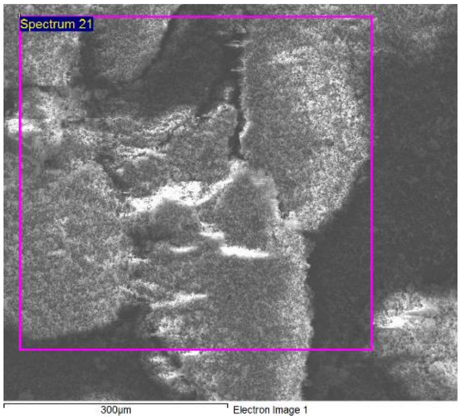

Figure 69. SEM image of **Sample 2** (2nd measurement).

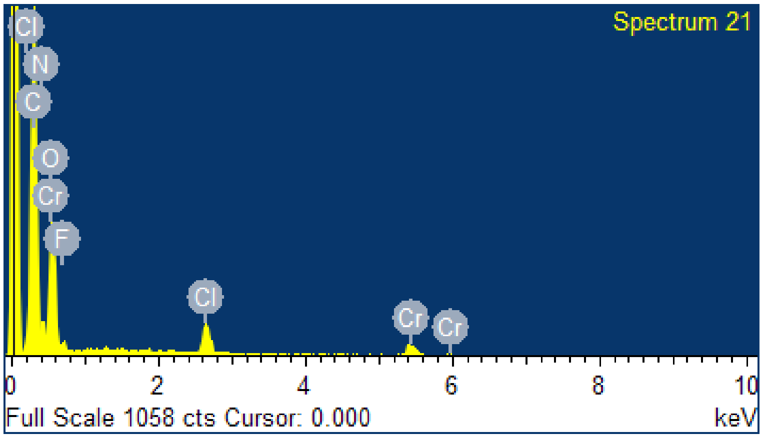

Figure 70. EDX spectrum of **Sample 2** (2nd measurement).

Table 17. EDX data for **Sample 2** (2nd measurement).

Element	Weight%	Atomic%
C K	46.61	60.60
N K	9.71	10.83
O K	20.56	20.07
F K	1.84	1.52
Cl K	4.23	1.86
Cr L	17.04	5.12
Totals	100.00	

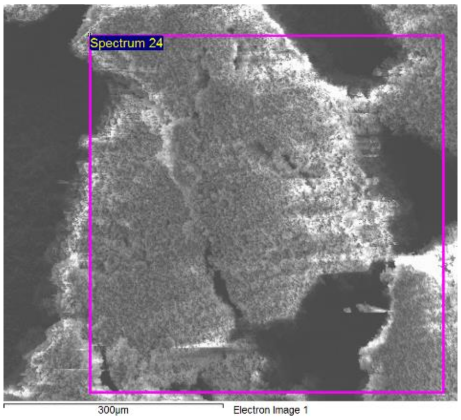

Figure 71. SEM image of **Sample 2** (3rd measurement).

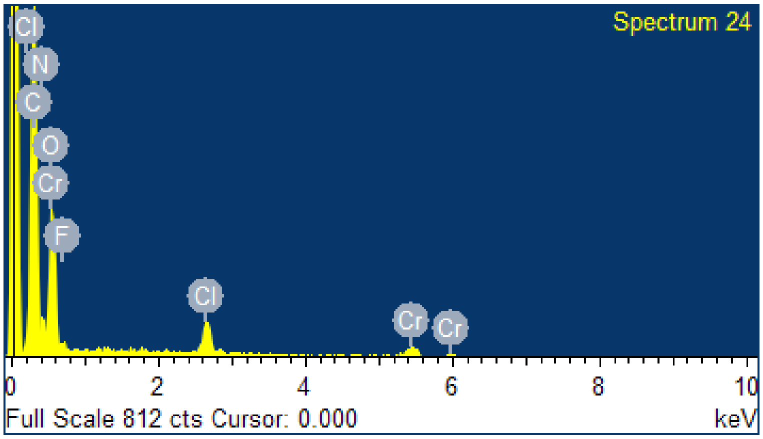

Figure 72. EDX spectrum of **Sample 2** (3rd measurement).

Table 18. EDX data for **Sample 2** (3rd measurement).

Element	Weight%	Atomic%
C K	46.11	60.02
N K	10.05	11.22
O K	20.59	20.12
F K	1.89	1.55
Cl K	4.69	2.07
Cr L	16.66	5.01
Totals	100.00	

Table 19. Summary of the EDX data of **Sample 2**.

	F atomic%	Cr atomic%
1st measurement	2.11	6.98
2nd measurement	1.52	5.12
3rd measurement	1.55	5.01
Average	1.73	5.70

F/Cr molar ratio = F Atomic% / Cr Atomic% = 1.73% / 5.70% = 0.304

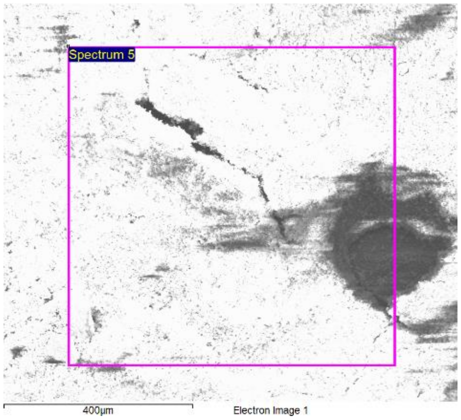

Figure 73. SEM image of **Sample 3** (1st measurement).

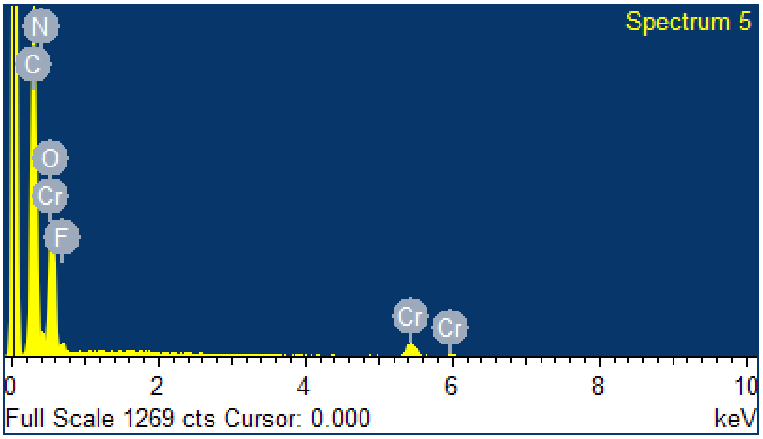

Figure 74. EDX spectrum of **Sample 3** (1st measurement).

Table 20. EDX data for **Sample 3** (1st measurement).

Element	Weight%	Atomic%
C K	44.70	59.80
N K	5.60	6.43
O K	23.89	23.99
F K	3.36	2.84
Cr L	22.46	6.94
Totals	100.00	

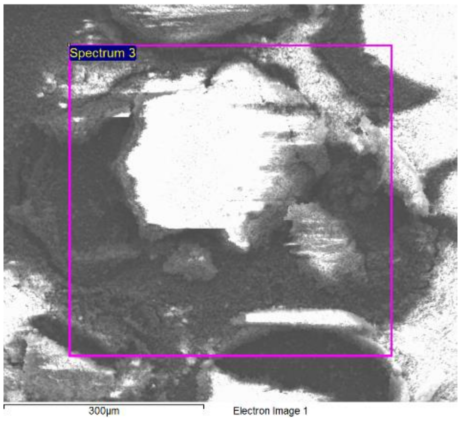

Figure 75. SEM image of **Sample 3** (2nd measurement).

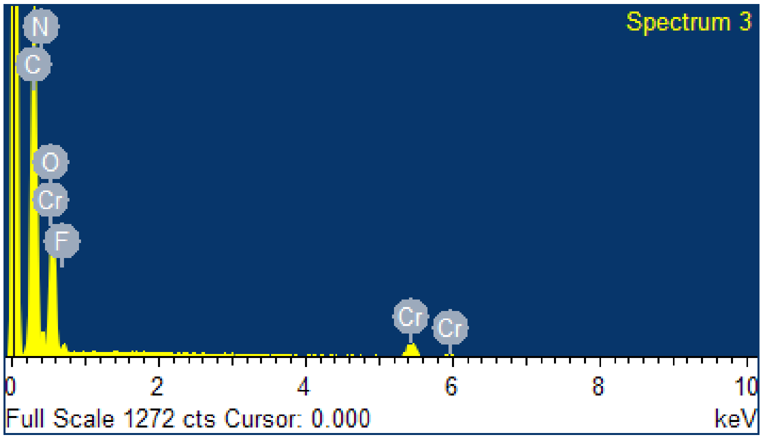

Figure 76. EDX spectrum of **Sample 3** (2nd measurement).

Table 21. EDX data for **Sample 3** (2nd measurement).

Element	Weight%	Atomic%
C K	42.88	59.28
N K	6.38	7.56
O K	21.04	21.84
F K	3.29	2.88
Cr L	26.42	8.44
Totals	100.00	

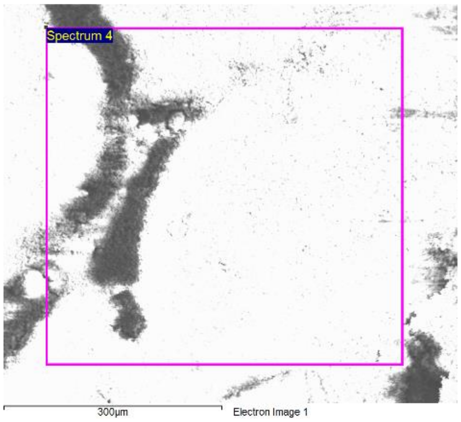

Figure 77. SEM image of **Sample 3** (3rd measurement).

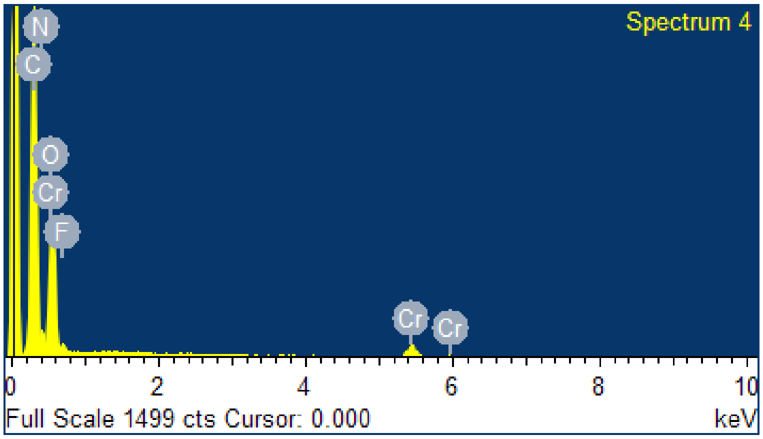

Figure 78. EDX spectrum of **Sample 3** (3rd measurement).

Table 22. EDX data for **Sample 3** (3rd measurement).

Element	Weight%	Atomic%
C K	43.43	59.86
N K	5.20	6.15
O K	22.47	23.25
F K	2.78	2.42
Cr L	26.13	8.32
Totals	100.00	

Table 23. Summary of the EDX data of **Sample 3**.

	F atomic%	Cr atomic%
1st measurement	2.06	6.92
2nd measurement	2.88	8.44
3rd measurement	2.42	8.32
Average	2.45	7.89

F/Cr molar ratio = F Atomic% / Cr Atomic% = 2.45% / 7.89% = 0.310

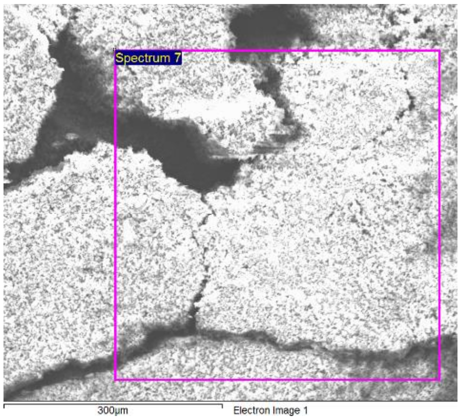

Figure 79. SEM image of **Sample 4** (1st measurement).

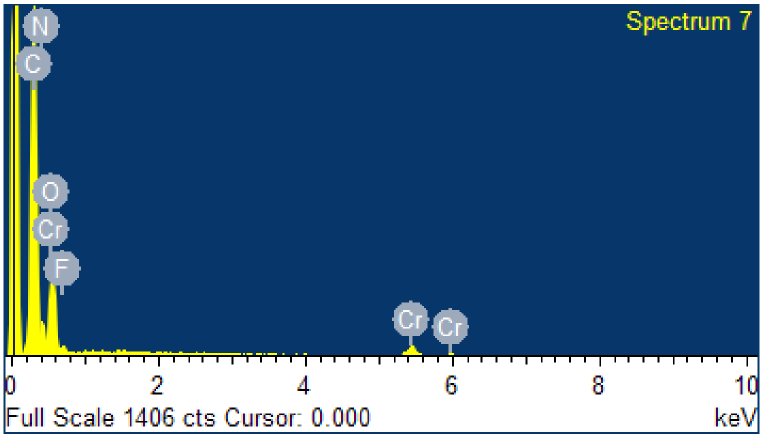

Figure 80. EDX spectrum of **Sample 4** (1st measurement).

Table 24. EDX data for **Sample 4** (1st measurement).

Element	Weight%	Atomic%
C K	46.01	60.10
N K	13.38	14.99
O K	16.87	16.54
F K	2.29	1.89
Cr L	21.46	6.47
Totals	100.00	

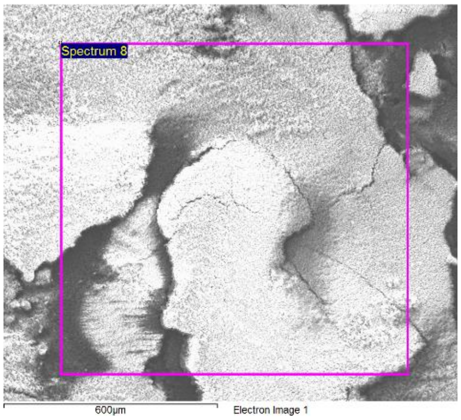

Figure 81. SEM image of **Sample 4** (2nd measurement).

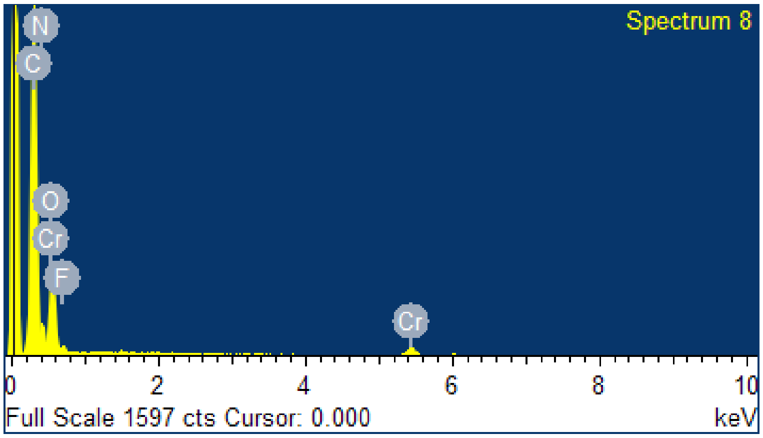

Figure 82. EDX spectrum of **Sample 4** (2nd measurement).

Table 25. EDX data for **Sample 4** (2nd measurement).

Element	Weight%	Atomic%
C K	46.83	60.93
N K	12.84	14.33
O K	17.05	16.65
F K	2.11	1.73
Cr L	21.18	6.36
Totals	100.00	

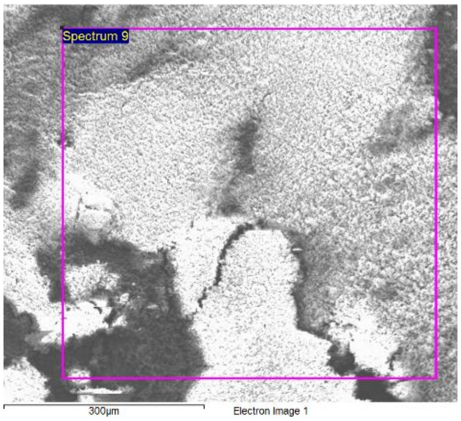

Figure 83. SEM image of **Sample 4** (3rd measurement).

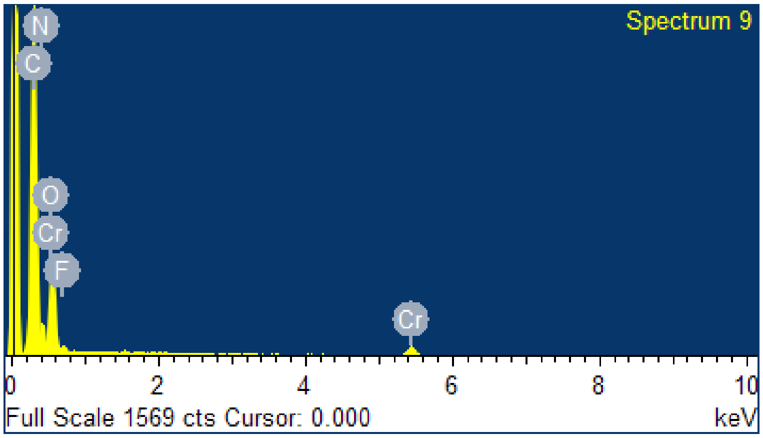

Figure 84. EDX spectrum of **Sample 4** (3rd measurement).

Table 26. EDX data for **Sample 4** (3rd measurement).

Element	Weight%	Atomic%
C K	45.04	59.73
N K	12.22	13.90
O K	17.33	17.25
F K	2.51	2.11
Cr L	22.90	7.02
Totals	100.00	

Table 27. Summary of the EDX data of **Sample 4**.

	F Atomic%	Cr Atomic%
1st measurement	1.89	6.47
2nd measurement	1.73	6.36
3rd measurement	2.11	7.02
Average	1.91	6.62

F/Cr molar ratio = F Atomic% / Cr Atomic% = 1.91% / 6.62% = 0.288

Table 28. Summary of the N/F and F/Cr molar ratios of **Sample 1-4**, and their consequent N/Cr molar ratios.

Sample	n(N)/n(F)	n(F)/n(Cr)	n(N)/n(Cr)
Sample 1	7.42	0.34	2.52
Sample 2	11.63	0.30	3.49
Sample 3	12.76	0.31	3.96
Sample 4	18.25	0.29	5.29

Table 29. Summary of the CO_2 uptakes, the total pore volumes, and the molar ratios between alkylamine and Cr in the amine-modified samples.

Sample	CO_2 uptake (mmol/g)[a]	Total pore volume (cm^3/g)	n(N)/n(Cr)	n(alkylamine)/n(Cr)
Sample 1	1.70	0.68	2.52	0.84
Sample 2	1.88	0.58	3.49	0.87
Sample 3	3.75	0.64	3.96	1.32
Sample 4	4.20	0.36	5.29	1.32
Sample 5	3.58	0.66	N/A	N/A
Sample 6	4.13	0.37	N/A	N/A

[a]. The CO_2 uptakes are the values at 150 mbar on the adsorption isotherms at 25 °C.

The molar ratio between alkylamine and Cr in **Sample 4** was further confirmed by the NMR spectrum of the degraded **Sample 4** in NaOD/D_2O solution (**Figure 85**). The protons on BDC and TAEA were integrated to be 4 and 17.11, respectively. Therefore, n(TAEA)/n(BDC) = (17.11/12)/(4/4) = 1.43/1. Since in Cr-MIL-101, n(Cr)/n(BDC) = 1/1, it is reasonable to arrive at the conclusion that in **Sample 4**, n(TAEA)/n(Cr) = 1.43/1. This result is comparable to the value obtained by EDX and EA.

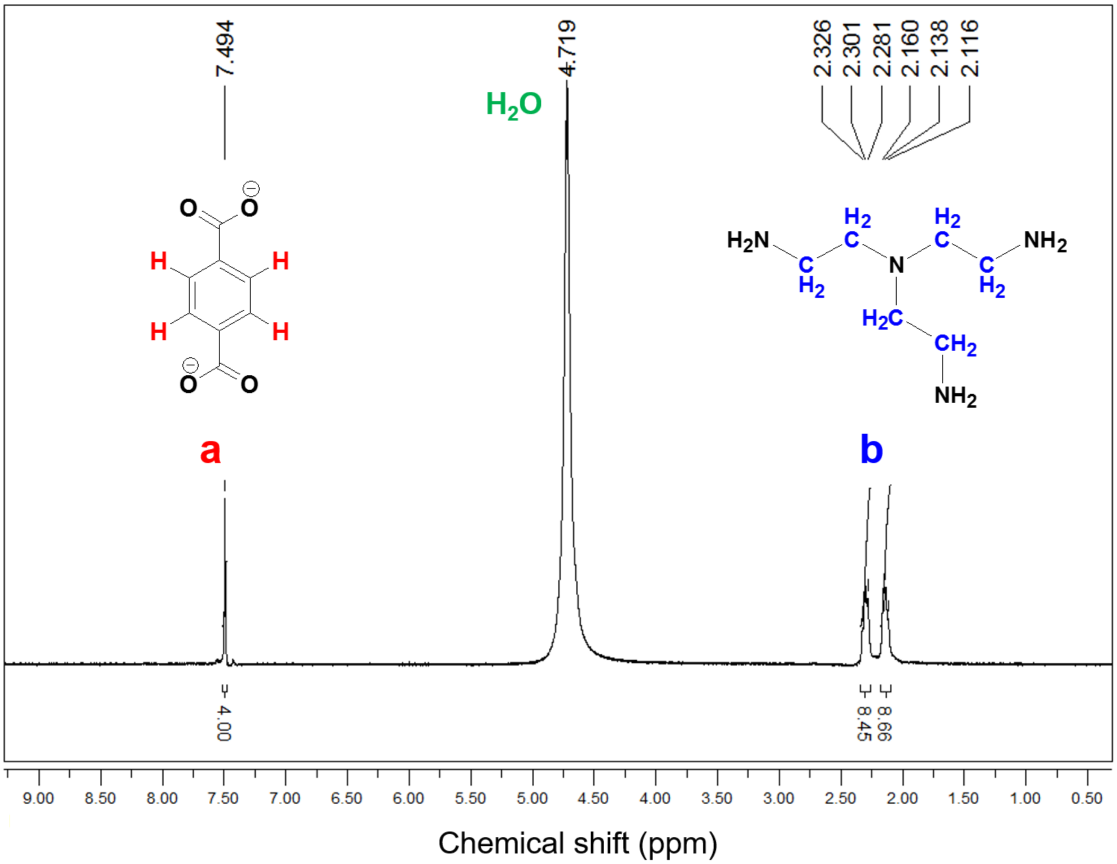

Figure 85. NMR spectrum of the decomposed **Sample 4** in a NaOD solution in D_2O.

3.3.3 Alkylamine Binding Interaction

It is worth noting that for samples prepared in CH, the ratio between alkylamine and Cr is higher than 1 (**Table 29** and **Figure 85**). This implies not all alkylamine molecules are bound onto Cr-MIL-101 through the coordination bonds formed between Cr open metal sites (OMSs) and amine groups. Considering the chemistry environment around incorporated alkylamines, there are two types of alkylamine binding interaction in these MOFs. One type is the aforementioned coordination bonds generated between Cr and alkylamine (**Type I**), while the other is the hydrogen bonds between the amine groups from two different alkylamine molecules. (**Type II**). As the temperature increases, the amount of the CO_2 adsorbed through the chemical bonds with amine groups will decrease as normal. On the other side, a higher temperature can also break the hydrogen bonds in **Type II** interactions and generate some free amine groups that are ready to capture CO_2. It can lead to an increment in the amount of CO_2 adsorbed at high temperatures.[103] The net result from these two aspects is that CO_2 uptake has no apparent decrease as the temperature increases, which is likely to result in an overestimated isosteric heat of adsorption $-Q_{st}$. These inferred features in CO_2 adsorption isotherms truly occur in the case of **Sample 4** (**Figure 86**), with CO_2 uptakes as high as 4.21 mmol/g at 25 °C and 150 mbar, and 4.05 mmolg/g at 40 °C and 150 mbar. The data provide additional experimental evidence to corroborate the existence of the two types of alkylamine binding interaction in **Sample 4**.

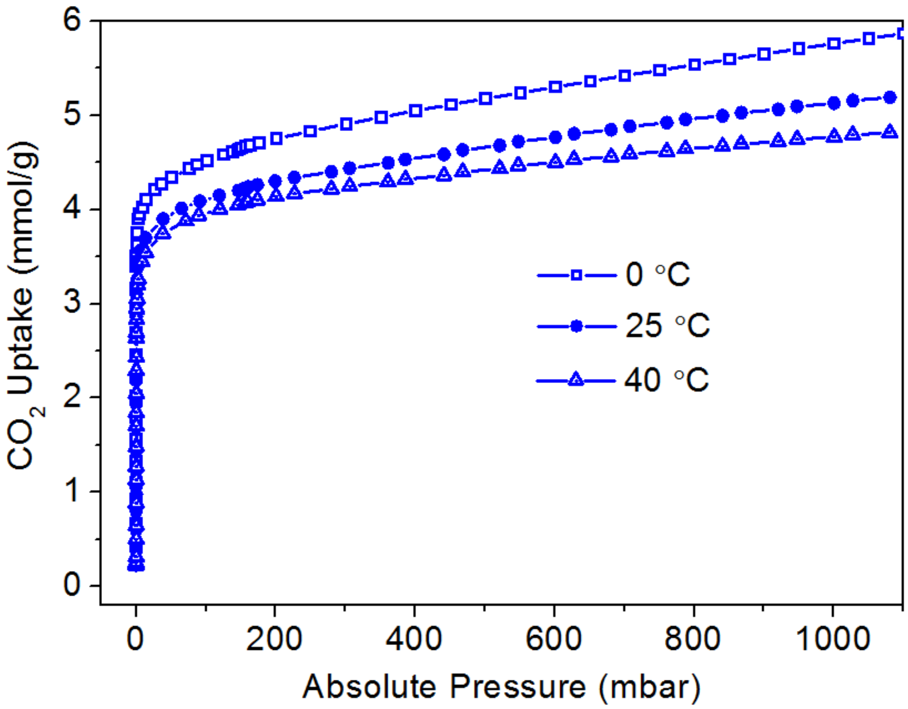

Figure 86. CO$_2$ adsorption isotherms of **Sample 4** at 0°C, 25 °C and 40 °C.

3.3.4 Thermal Stability of Sample 4 Assessed by TGA-MS

As stated previously, the hydrogen bonds between alkylamines can be relieved as these materials usually suffer from alkylamine leaching problem during desorption procedure. To clarify whether there is alkylamine leaching from **Sample 4** under the CO$_2$ desorption condition, its thermal stability was evaluated by TGA-MS. The results show that there are no apparent mass peaks of alkylamine before the temperature reaches 150 °C (**Figure 87**). This temperature is higher than the usual CO$_2$ desorption temperature. It demonstrates even **Type II** binding interaction is firm enough to fixate the alkylamines anchored in Cr-MIL-101 and there will be no leaching of alkylamine during recovery of the material. Moreover, because of the structural confinement in the framework, it is very likely that the alkylamine molecules have multiple hydrogen bonds with their surrounding molecules. This would endow the amine-modified MOFs with higher thermal stability as well.

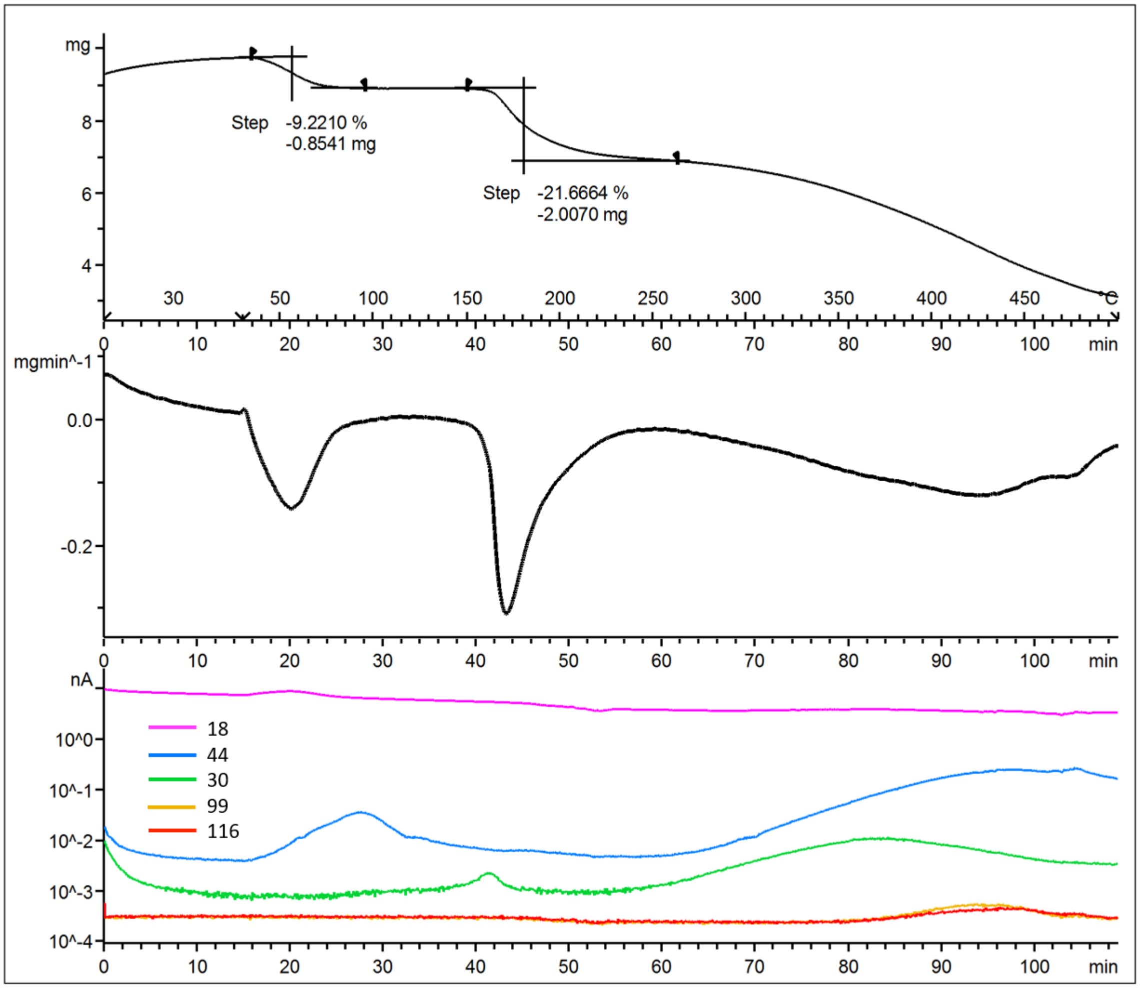

Figure 87. The TGA curve (upper), the first derivative of the TGA curve (middle) and the mass spectrum of the released species (lower) of **Sample 4** as the temperature rises from 30 °C to 500 °C.

3.3.5 Recyclability Test and Breakthrough Measurements

To evaluate the CO_2 capture performance of **Sample 4**, the recyclability of **Sample 4** was tested by exposing the material under a mixed gas flow (15% CO_2 and 85% He) at 1 bar and 40 °C for 30 min and activated at 90 °C under a flow of pure He for 10 min. There are no apparent changes of CO_2 uptake during the recyclability test (**Figure 88**), suggesting that the material is a regenerable adsorbent.

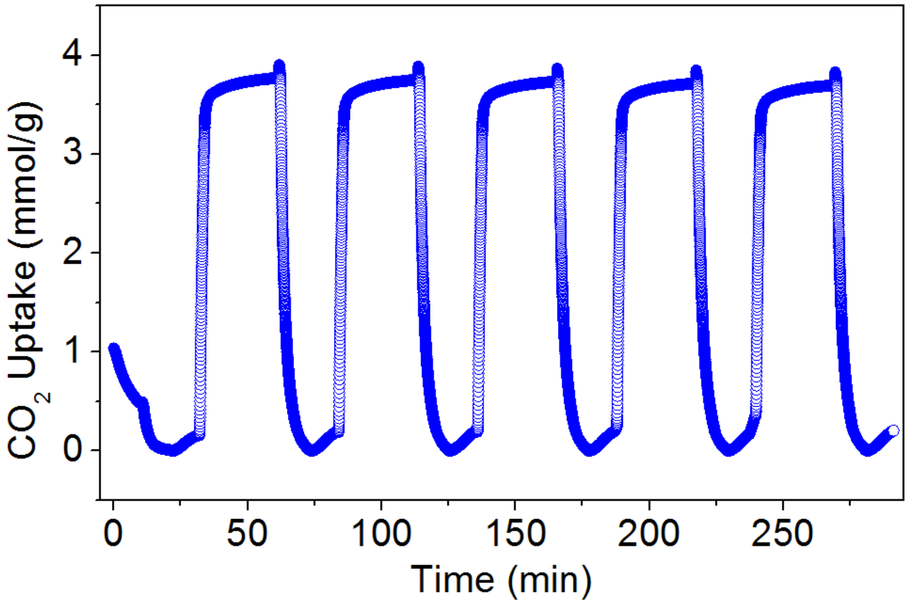

Figure 88. Recycling test of **Sample 4** on TGA equipment with the adsorption and desorption conditions set as a 15:85 CO_2/He (v/v) flow at 40 °C and 1 bar, and a pure He flow at 90 °C and 1 bar, respectively.

To further assess the CO_2 capture capability of the material in mixed gas scenarios, we conducted dynamic column breakthrough experiments on **Sample 4** with a binary gas mixture composed of 15% CO_2 and 85% N_2. The breakthrough curves indicate that CO_2 would not be detected as the end of the column until the CO_2 injection amounts were 5 mmol/g at 25 °C and 4.3 mmol/g at 40 °C. By contrast, N_2 would break through at much earlier stages at both temperatures (**Figure 89-92**). This suggests the highly selective adsorption of CO_2 over N_2 in **Sample 4**. Based on the data from breakthrough experiments, the CO_2 capacities of **Sample 4** were calculated to be 4.42 mmol/g at 25 °C and 4.28 mmol/g at 40 °C, which are comparable to the results attained in its CO_2 isotherms.

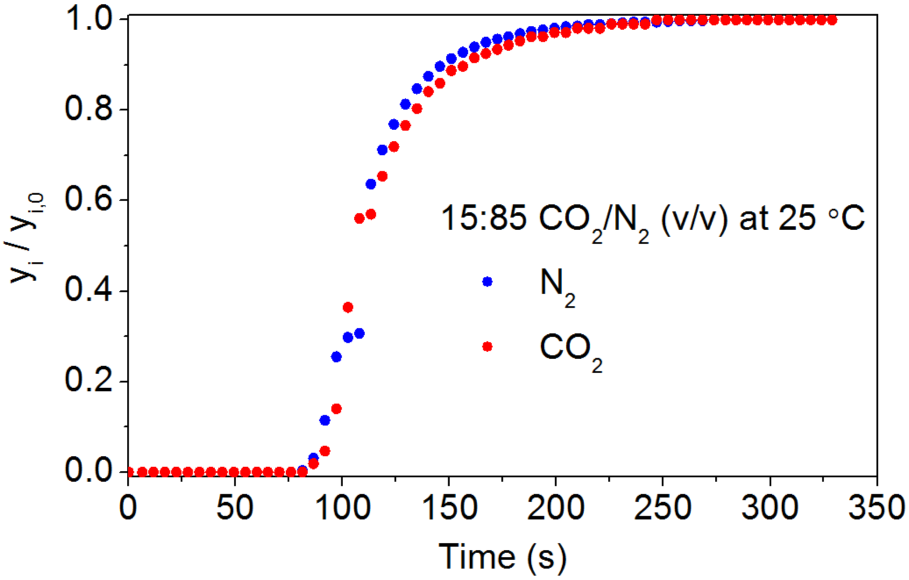

Figure 89. Breakthrough curves of an empty column for dead volume calibration at 25 °C. The gas flow is a 15:85 CO_2/N_2 (v/v) flow at 25 °C with an inlet pressure of 1.2 bar and an outlet pressure of 1 bar. y_i and $y_{i,0}$ are the molar fractions of a gas species at the inlet and outlet, respectively.

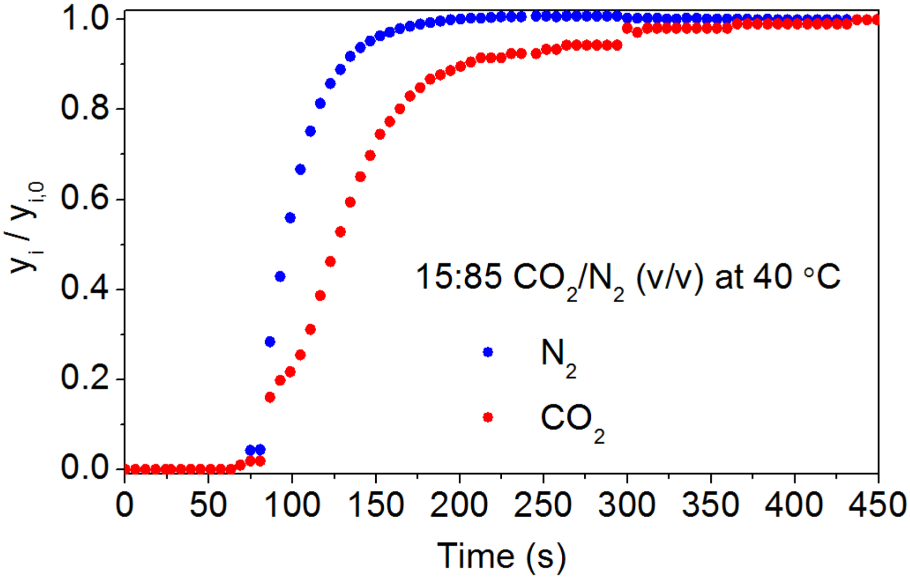

Figure 90. Breakthrough curves of an empty column for dead volume calibration at 40 °C. The gas flow is a 15:85 CO_2/N_2 (v/v) flow at 40 °C with an inlet pressure of 1.2 bar and an outlet pressure of 1 bar. y_i and $y_{i,0}$ are the molar fractions of a gas species at the inlet and outlet, respectively.

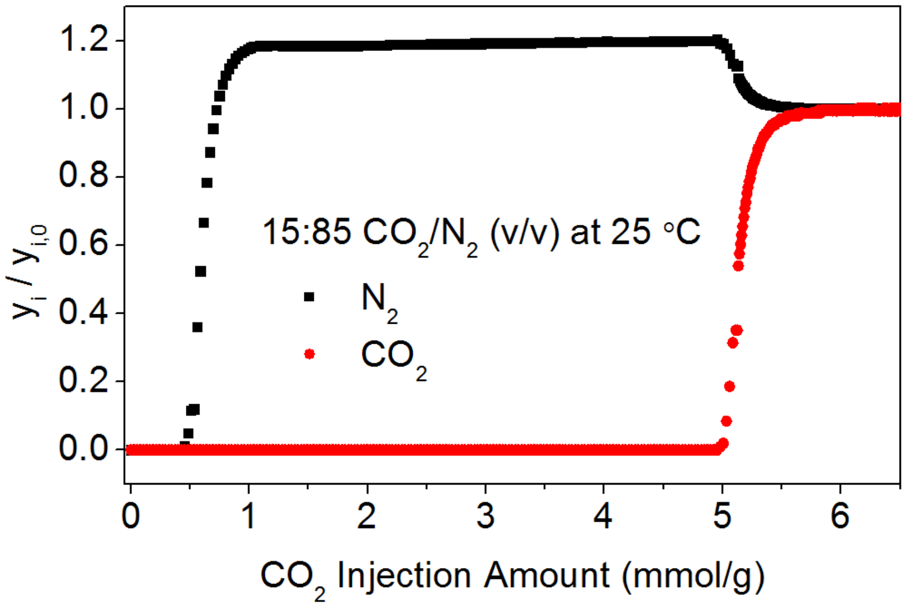

Figure 91. Breakthrough curves of a column packed with **Sample 4**. The gas flow is a 15:85 CO_2/N_2 (v/v) flow at 25 °C with an inlet pressure of 1.2 bar and an outlet pressure of 1 bar. y_i and $y_{i,0}$ are the molar fractions of a gas species at the inlet and outlet, respectively.

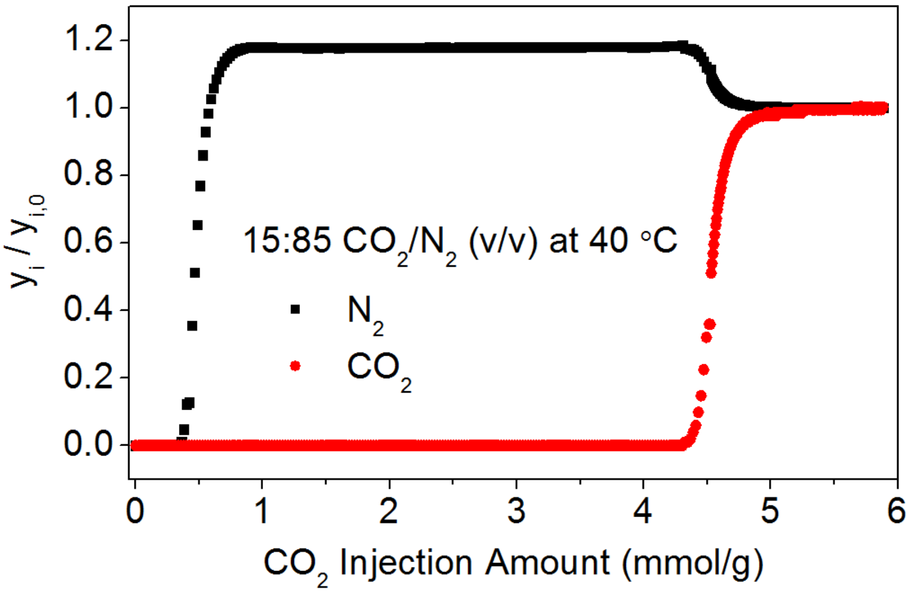

Figure 92. Breakthrough curves of a column packed with **Sample 4**. The gas flow is a 15:85 CO_2/N_2 (v/v) flow at 40 °C with an inlet pressure of 1.2 bar and an outlet pressure of 1 bar. y_i and $y_{i,0}$ are the molar fractions of a gas species at the inlet and outlet, respectively.

3.4 Conclusion

With rationally selected alkylamine and solvent species, a high loading amount of alkylamine was successfully achieved in the mesoporous and chemically stable Cr-MIL-101. This result indicates that nonpolar or less polar solvents are more favorable for the migration of alkylamine from alkylamine solutions to MOFs, because the alkylamine dispersed in less polar solvents are endowed with a higher chemical potential that drives more alkylamine molecules to be incorporated into the frameworks. The obtained material displays pure-component CO_2 uptakes as high as 4.21 mmol/g at 25 °C and 150 mbar, and 4.05 mmol/g at 40 °C and 150 mbar. No apparent decline can be discerned in its CO_2

capacity after multiple adsorption-desorption cycles. Its performance was also characterized by dynamic column breakthrough experiments, which demonstrate that the material exhibits good CO_2/N_2 selectivity in the case of binary gas mixtures.

CHAPTER IV

SUMMARY

Alkylamine-functionalized metal-organic frameworks (MOFs) are regarded as promising candidates to selectively capture CO_2 from flue gas, air, or other forms of gas mixtures, because the incorporated alkylamine molecules endow MOFs with strong CO_2 affinity, which is essential for selective CO_2 adsorption at low pressure. To date most alkylamine grafting experiments in MOFs are conducted using the coordination bonds between open metal sites (OMSs) and amine groups. This inevitably would set an upper limit on alkylamine density in MOFs and the corresponding CO_2 uptakes that can be achieved.

To overcome this obstacle, a new approach to integrating alkylamine into MOFs is explored, which exploits the Brønsted acid-base reaction between MOFs and alkylamine. In this work, the pristine MOF utilized is Cr-MIL-101-SO_3H, which has a high density of inherent sulfonic acid groups. Cr-MIL-101-SO_3H was modified with a series of alkylamines with different structures. The FTIR spectrum of the amine-modified Cr-MIL-101 with the highest CO_2 uptake was collected. The peaks at 3234 cm^{-1} and 3147 cm^{-1} are characteristic of the stretching vibrations of $-NH_3^+$, which serve as a good evidence for the proton transfer and subsequent ionic interaction between $-SO_3H$ and $-NH_2$. Moreover, experimental factors, such as alkylamine structure, alkylamine quantity, reaction time, reaction temperature, and solvent, are systematically optimized by control experiments to maximize the CO_2 uptake of the obtained material. The results reveal that apart from the alkylamine structure, the solvent species used to conduct alkylamine incorporation is also crucial in determining the CO_2 capture performance of the generated adsorbent. This point is rationalized thoroughly from the perspective of chemical potential. Specifically, alkylamine has weaker interaction with less polar solvents than with more polar ones. This makes the alkylamine dispersed in less polar solvents comparatively unstable and have a higher chemical potential than in more polar ones. The higher chemical potential serves as a stronger driving force to push more alkylamine molecules into the frameworks and result in a higher CO_2 capture amount of the material.

Under the optimal alkylamine tethering condition, the obtained TAEA-functionalized Cr-MIL-101-SO_3H (Cr-MIL-101-SO_3H-TAEA, TAEA = Tris(2-aminoethyl)amine) has cyclic CO_2 uptakes of 2.28 mmol/g at 150 mbar and 40 °C, and 1.12 mmol/g at 0.4 mbar and 20 °C. Its isosteric heat of CO_2 adsorption calculated from the CO_2 uptake data at 0 °C, 20 °C and 40 °C is 87 kJ/mol at zero coverage. This indicates a strong interaction between CO_2 and Cr-MIL-101-SO_3H-TAEA. The low-cost starting materials and simple synthetic procedure of Cr-MIL-101-SO_3H-TAEA all suggest its advantages in large-scale production for practical applications.

The aforementioned conclusion that alkylamine structure and solvent species are very influential in the alkylamine loading amount in MOFs and their CO_2 uptakes was further applied in another mesoporous and highly stable MOF, Cr-MIL-101. With cyclohexane (CH) and TAEA as the judiciously selected solvent and alkylamine, respectively, the obtained material displays pure-component CO_2 uptakes as high as 4.21 mmol/g at 25 °C and 150 mbar, and 4.05 mmol/g at 40 °C and 150 mbar. No apparent decline can be observed in its CO_2 capacity after multiple adsorption-desorption cycles. It also exhibits a comparable CO_2 adsorption amount in the dynamic column breakthrough experiment, in which the adsorbent was exposed to a binary gas mixture of 15% CO_2 and 85% N_2. Thus, a good CO_2/N_2 selectivity of the material was also demonstrated with this breakthrough experiment. As indicated by the atomic ratio between N and Cr of the resulting adsorbent, the integrated alkylamine molecules outnumber the OMSs in Cr-MIL-101. This implies that a portion of alkylamine is tethered through the hydrogen bonds between alkylamine molecules. Thermal stability of the adsorbent is assessed with thermogravimetric analysis (TGA), suggesting that there is no alkylamine leaching before the temperature is higher than 150 °C. Therefore, the material is confirmed to be sufficiently robust at adsorption and desorption temperatures, which indicates its good eligibility as adsorbents in real CO_2 capture scenarios.

REFERENCES

1 K. Sumida, D. L. Rogow, J. A. Mason, T. M. McDonald, E. D. Bloch, Z. R. Herm, T.-H. Bae and J. R. Long, *Chemical Reviews*, 2012, **112**, 724-781.

2 T.-H. Bae and J. R. Long, *Energy & Environmental Science*, 2013, **6**, 3565-3569.

3 Y. Peng, Y. Li, Y. Ban, H. Jin, W. Jiao, X. Liu and W. Yang, *Science*, 2014, **346**, 1356-1359.

4 E. S. Sanz-Pérez, C. R. Murdock, S. A. Didas and C. W. Jones, *Chemical Reviews*, 2016, **116**, 11840-11876.

5 S. R. Caskey, A. G. Wong-Foy and A. J. Matzger, *Journal of the American Chemical Society*, 2008, **130**, 10870-10871.

6 J. A. Mason, K. Sumida, Z. R. Herm, R. Krishna and J. R. Long, *Energy & Environmental Science*, 2011, **4**, 3030-3040.

7 Z. Bao, L. Yu, Q. Ren, X. Lu and S. Deng, *Journal of Colloid and Interface Science*, 2011, **353**, 549-556.

8 T. M. McDonald, D. M. D'Alessandro, R. Krishna and J. R. Long, *Chemical Science*, 2011, **2**, 2022-2028.

9 T. M. McDonald, W. R. Lee, J. A. Mason, B. M. Wiers, C. S. Hong and J. R. Long, *Journal of the American Chemical Society*, 2012, **134**, 7056-7065.

10 A. M. Fracaroli, H. Furukawa, M. Suzuki, M. Dodd, S. Okajima, F. Gándara, J. A. Reimer and O. M. Yaghi, *Journal of the American Chemical Society*, 2014, **136**, 8863-8866.

11 T. M. McDonald, J. A. Mason, X. Kong, E. D. Bloch, D. Gygi, A. Dani, V. Crocella, F. Giordanino, S. O. Odoh, W. S. Drisdell, B. Vlaisavljevich, A. L. Dzubak, R. Poloni, S. K. Schnell, N. Planas, K. Lee, T. Pascal, L. F. Wan, D. Prendergast, J. B. Neaton, B. Smit, J. B. Kortright, L. Gagliardi, S. Bordiga, J. A. Reimer and J. R. Long, *Nature*, 2015, **519**, 303-308.

12 W. R. Lee, H. Jo, L.-M. Yang, H. Lee, D. W. Ryu, K. S. Lim, J. H. Song, D. Y. Min, S. S. Han, J. G. Seo, Y. K. Park, D. Moon and C. S. Hong, *Chemical Science*, 2015, **6**, 3697-3705.

13 W. R. Lee, S. Y. Hwang, D. W. Ryu, K. S. Lim, S. S. Han, D. Moon, J. Choi and C. S. Hong, *Energy & Environmental Science*, 2014, **7**, 744-751.

14 H. Jo, W. R. Lee, N. W. Kim, H. Jung, K. S. Lim, J. E. Kim, D. W. Kang, H. Lee, V. Hiremath, J. G. Seo, H. Jin, D. Moon, S. S. Han and C. S. Hong, *ChemSusChem*, 2017, **10**, 541-550.

15 H. Li, K. Wang, D. Feng, Y.-P. Chen, W. Verdegaal and H.-C. Zhou, *ChemSusChem*, 2016, **9**, 2832-2840.

16 P.-Q. Liao, X.-W. Chen, S.-Y. Liu, X.-Y. Li, Y.-T. Xu, M. Tang, Z. Rui, H. Ji, J.-P. Zhang and X.-M. Chen, *Chemical Science*, 2016, **7**, 6528-6533.

17 P. Nugent, Y. Belmabkhout, S. D. Burd, A. J. Cairns, R. Luebke, K. Forrest, T. Pham, S. Ma, B. Space, L. Wojtas, M. Eddaoudi and M. J. Zaworotko, *Nature*, 2013, **495**, 80-84.

18 O. Shekhah, Y. Belmabkhout, Z. Chen, V. Guillerm, A. Cairns, K. Adil and M. Eddaoudi, *Nature Communications*, 2014, **5**.

19 O. Shekhah, Y. Belmabkhout, K. Adil, P. M. Bhatt, A. J. Cairns and M. Eddaoudi, *Chemical Communications*, 2015, **51**, 13595-13598.

20 P.-Q. Liao, H. Chen, D.-D. Zhou, S.-Y. Liu, C.-T. He, Z. Rui, H. Ji, J.-P. Zhang and X.-M. Chen, *Energy & Environmental Science*, 2015, **8**, 1011-1016.

21 S. Basu, A. Cano-Odena and I. F. J. Vankelecom, *Separation and Purification Technology*, 2011, **81**, 31-40.

22 J. Shen, G. Liu, K. Huang, Q. Li, K. Guan, Y. Li and W. Jin, *Journal of Membrane Science*, 2016, **513**, 155-165.

23 H. Yin, J. Wang, Z. Xie, J. Yang, J. Bai, J. Lu, Y. Zhang, D. Yin and J. Y. S. Lin, *Chemical Communications*, 2014, **50**, 3699-3701.

24 S. Zhao, X. Cao, Z. Ma, Z. Wang, Z. Qiao, J. Wang and S. Wang, *Industrial & Engineering Chemistry Research*, 2015, **54**, 5139-5148.

25 L. M. Robeson, *Journal of Membrane Science*, 2008, **320**, 390-400.

26 S. Friebe, A. Mundstock, D. Unruh, F. Renz and J. Caro, *Journal of Membrane Science*, 2016, **516**, 185-193.

27 Z. X. Kang, Y. W. Peng, Z. G. Hu, Y. H. Qian, C. L. Chi, L. Y. Yeo, L. Tee and D. Zhao, *Journal of Materials Chemistry A*, 2015, **3**, 20801-20810.

28 J. Sanchez-Lainez, B. Zornoza, S. Friebe, J. Caro, S. Cao, A. Sabetghadam, B. Seoane, J. Gascon, F. Kapteijn, C. Le Guillouzer, G. Clet, M. Daturi, C. Tellez and J. Coronas, *Journal of Membrane Science*, 2016, **515**, 45-53.

29 N. Casas, J. Schell, R. Blom and M. Mazzotti, *Separation and Purification Technology*, 2013, **112**, 34-48.

30 Z. R. Herm, J. A. Swisher, B. Smit, R. Krishna and J. R. Long, *Journal of the American Chemical Society*, 2011, **133**, 5664-5667.

31 D. Kim, H. K. Lim, H. Ro, H. Kim and H. Lee, *Chemistry - A European Journal*, 2015, **21**, 1125-1129.

32 J. Schell, N. Casas, R. Blom, A. I. Spjelkavik, A. Andersen, J. H. Cavka and M. Mazzotti, *Adsorption - Journal of the International Adsorption Society*, 2012, **18**, 213-227.

33 E. D. Bloch, L. J. Murray, W. L. Queen, S. Chavan, S. N. Maximoff, J. P. Bigi, R. Krishna, V. K. Peterson, F. Grandjean, G. J. Long, B. Smit, S. Bordiga, C. M. Brown and J. R. Long, *Journal of the American Chemical Society*, 2011, **133**, 14814-14822.

34 E. D. Bloch, W. L. Queen, M. R. Hudson, J. A. Mason, D. J. Xiao, L. J. Murray, R. Flacau, C. M. Brown and J. R. Long, *Angewandte Chemie International Edition*, 2016, **55**, 8605-8609.

35 L. J. Murray, M. Dinca, J. Yano, S. Chavan, S. Bordiga, C. M. Brown and J. R. Long, *Journal of the American Chemical Society*, 2010, **132**, 7856-7857.

36 D. J. Xiao, M. I. Gonzalez, L. E. Darago, K. D. Vogiatzis, E. Haldoupis, L. Gagliardi and J. R. Long, *Journal of the American Chemical Society*, 2016, **138**, 7161-7170.

37 R. Quadrelli and S. Peterson, *Energy Policy*, 2007, **35**, 5938-5952.

38 R. S. Haszeldine, *Science*, 2009, **325**, 1647-1652.

39 D. M. D'Alessandro, B. Smit and J. R. Long, *Angewandte Chemie International Edition*, 2010, **49**, 6058-6082.

40 A. Goeppert, M. Czaun, G. K. Surya Prakash and G. A. Olah, *Energy & Environmental Science*, 2012, **5**, 7833-7853.

41 A. Kumar, D. G. Madden, M. Lusi, K.-J. Chen, E. A. Daniels, T. Curtin, J. J. Perry and M. J. Zaworotko, *Angewandte Chemie International Edition*, 2015, **54**, 14372-14377.

42 W. Lu, J. P. Sculley, D. Yuan, R. Krishna, Z. Wei and H.-C. Zhou, *Angewandte Chemie International Edition*, 2012, **51**, 7480-7484.

43 E. De Canck, I. Ascoop, A. Sayari and P. Van Der Voort, *Physical Chemistry Chemical Physics*, 2013, **15**, 9792-9799.

44 J.-S. Lee, J.-H. Kim, J.-T. Kim, J.-K. Suh, J.-M. Lee and C.-H. Lee, *Journal of Chemical & Engineering Data*, 2002, **47**, 1237-1242.

45 Y. Wang and M. D. LeVan, *Journal of Chemical & Engineering Data*, 2009, **54**, 2839-2844.

46 C. F. Martín, M. G. Plaza, J. J. Pis, F. Rubiera, C. Pevida and T. A. Centeno, *Separation and Purification Technology*, 2010, **74**, 225-229.

47 J. C. Hicks, J. H. Drese, D. J. Fauth, M. L. Gray, G. Qi and C. W. Jones, *Journal of the American Chemical Society*, 2008, **130**, 2902-2903.

48 D. P. Bezerra, R. S. Oliveira, R. S. Vieira, C. L. Cavalcante and D. C. S. Azevedo, *Adsorption*, 2011, **17**, 235-246.

49 S. Xiang, Y. He, Z. Zhang, H. Wu, W. Zhou, R. Krishna and B. Chen, *Nature Communications*, 2012, **3**, 954.

50 P. Deria, J. E. Mondloch, E. Tylianakis, P. Ghosh, W. Bury, R. Q. Snurr, J. T. Hupp and O. K. Farha, *Journal of the American Chemical Society*, 2013, **135**, 16801-16804.

51 P. Deria, S. Li, H. Zhang, R. Q. Snurr, J. T. Hupp and O. K. Farha, *Chemical Communications*, 2015, **51**, 12478-12481.

52 A. Phan, C. J. Doonan, F. J. Uribe-Romo, C. B. Knobler, M. O'Keeffe and O. M. Yaghi, *Accounts of Chemical Research*, 2010, **43**, 58-67.

53 A. R. Millward and O. M. Yaghi, *Journal of the American Chemical Society*, 2005, **127**, 17998-17999.

54 R. Banerjee, A. Phan, B. Wang, C. Knobler, H. Furukawa, M. O'Keeffe and O. M. Yaghi, *Science*, 2008, **319**, 939-943.

55 Q. Yang, S. Vaesen, F. Ragon, A. D. Wiersum, D. Wu, A. Lago, T. Devic, C. Martineau, F. Taulelle, P. L. Llewellyn, H. Jobic, C. Zhong, C. Serre, G. De Weireld and G. Maurin, *Angewandte Chemie International Edition*, 2013, **52**, 10316-10320.

56 Z. Zhang, H. T. H. Nguyen, S. A. Miller, A. M. Ploskonka, J. B. DeCoste and S. M. Cohen, *Journal of the American Chemical Society*, 2016, **138**, 920-925.

57 B. Zheng, J. Bai, J. Duan, L. Wojtas and M. J. Zaworotko, *Journal of the American Chemical Society*, 2011, **133**, 748-751.

58 J. An, S. J. Geib and N. L. Rosi, *Journal of the American Chemical Society*, 2010, **132**, 38-39.

59 Q.-G. Zhai, N. Bai, S. n. Li, X. Bu and P. Feng, *Inorganic Chemistry*, 2015, **54**, 9862-9868.

60 L.-C. Lin, J. Kim, X. Kong, E. Scott, T. M. McDonald, J. R. Long, J. A. Reimer and B. Smit, *Angewandte Chemie International Edition*, 2013, **52**, 4410-4413.

61 X. Kong, E. Scott, W. Ding, J. A. Mason, J. R. Long and J. A. Reimer, *Journal of the American Chemical Society*, 2012, **134**, 14341-14344.

62 C. R. Wade and M. Dinca, *Dalton Transactions*, 2012, **41**, 7931-7938.

63 A. C. Kizzie, A. G. Wong-Foy and A. J. Matzger, *Langmuir*, 2011, **27**, 6368-6373.

64 J. Liu, Y. Wang, A. I. Benin, P. Jakubczak, R. R. Willis and M. D. LeVan, *Langmuir*, 2010, **26**, 14301-14307.

65 T. M. McDonald, D. M. D'Alessandro, R. Krishna and J. R. Long, *Chemical Science*, 2011, **2**, 2022-2028.

66 Y. Hu, W. M. Verdegaal, S.-H. Yu and H.-L. Jiang, *ChemSusChem*, 2014, **7**, 734-737.

67 K. Wang, X.-L. Lv, D. Feng, J. Li, S. Chen, J. Sun, L. Song, Y. Xie, J.-R. Li and H.-C. Zhou, *Journal of the American Chemical Society*, 2016, **138**, 914-919.

68 F. Millange, C. Serre and G. Ferey, *Chemical Communications*, 2002, 822-823.

69 J. H. Cavka, S. Jakobsen, U. Olsbye, N. Guillou, C. Lamberti, S. Bordiga and K. P. Lillerud, *Journal of the American Chemical Society*, 2008, **130**, 13850-13851.

70 P. J. Waller, F. Gándara and O. M. Yaghi, *Accounts of Chemical Research*, 2015, **48**, 3053-3063.

71 T. Ben, H. Ren, S. Ma, D. Cao, J. Lan, X. Jing, W. Wang, J. Xu, F. Deng, J. M. Simmons, S. Qiu and G. Zhu, *Angewandte Chemie International Edition*, 2009, **48**, 9457-9460.

72 J. Juan-Alcaniz, R. Gielisse, A. B. Lago, E. V. Ramos-Fernandez, P. Serra-Crespo, T. Devic, N. Guillou, C. Serre, F. Kapteijn and J. Gascon, *Catalysis Science & Technology*, 2013, **3**, 2311-2318.

73 Y.-X. Zhou, Y.-Z. Chen, Y. Hu, G. Huang, S.-H. Yu and H.-L. Jiang, *Chemistry - A European Journal*, 2014, **20**, 14976-14980.

74 J. Jiang and O. M. Yaghi, *Chemical Reviews*, 2015, **115**, 6966-6997.

75 V. Colombo, C. Montoro, A. Maspero, G. Palmisano, N. Masciocchi, S. Galli, E. Barea and J. A. R. Navarro, *Journal of the American Chemical Society*, 2012, **134**, 12830-12843.

76 G. Férey, C. Mellot-Draznieks, C. Serre, F. Millange, J. Dutour, S. Surblé and I. Margiolaki, *Science*, 2005, **309**, 2040-2042.

77 N. P. G. Roeges, in *A Guide to the Complete Interpretation of Infrared Spectra of Organic Structures*, Wiley-VCH, Weinheim, 1994, ch. 3, pp. 80-87.

78 C. Reichardt, in *Solvents and Solvent Effects in Organic Chemistry*, Wiley-VCH, Weinheim, Third edn., 2003, ch. 7, pp. 418-424.

79 D. Thirion, V. Rozyyev, J. Park, J. Byun, Y. Jung, M. Atilhan and C. T. Yavuz, *Physical Chemistry Chemical Physics*, 2016, **18**, 14177-14181.

80 D. Y. C. Leung, G. Caramanna and M. M. Maroto-Valer, *Renewable and Sustainable Energy Reviews*, 2014, **39**, 426-443.

81 N. MacDowell, N. Florin, A. Buchard, J. Hallett, A. Galindo, G. Jackson, C. S. Adjiman, C. K. Williams, N. Shah and P. Fennell, *Energy & Environmental Science*, 2010, **3**, 1645-1669.

82 Q. Wang, J. Luo, Z. Zhong and A. Borgna, *Energy & Environmental Science*, 2011, **4**, 42-55.

83 S.-Y. Lee and S.-J. Park, *Journal of Industrial and Engineering Chemistry*, 2015, **23**, 1-11.

84 J. Wang, L. Huang, R. Yang, Z. Zhang, J. Wu, Y. Gao, Q. Wang, D. O'Hare and Z. Zhong, *Energy & Environmental Science*, 2014, **7**, 3478-3518.

85 E. E. Ünveren, B. Ö. Monkul, Ş. Sarıoğlan, N. Karademir and E. Alper, *Petroleum*, 2017, **3**, 37-50.

86 S. J. J. Titinchi, M. Piet, H. S. Abbo, O. Bolland and W. Schwieger, *Energy Procedia*, 2014, **63**, 8153-8160.

87 M. O'Keeffe and O. M. Yaghi, *Chemical Reviews*, 2012, **112**, 675-702.

88 R. B. Getman, Y.-S. Bae, C. E. Wilmer and R. Q. Snurr, *Chemical Reviews*, 2012, **112**, 703-723.

89 H. Jo, W. R. Lee, N. W. Kim, H. Jung, K. S. Lim, J. E. Kim, D. W. Kang, H. Lee, V. Hiremath, J. G. Seo, H. Jin, D. Moon, S. S. Han and C. S. Hong, *ChemSusChem*, 2017, **10**, 541-550.

90 D.-Y. Hong, Y. K. Hwang, C. Serre, G. Férey and J.-S. Chang, *Advanced Functional Materials*, 2009, **19**, 1537-1552.

91 Y.-K. Seo, J. W. Yoon, J. S. Lee, Y. K. Hwang, C.-H. Jun, J.-S. Chang, S. Wuttke, P. Bazin, A. Vimont, M. Daturi, S. Bourrelly, P. L. Llewellyn, P. Horcajada, C. Serre and G. Férey, *Advanced Materials*, 2012, **24**, 806-810.

92 A. Khutia, H. U. Rammelberg, T. Schmidt, S. Henninger and C. Janiak, *Chemistry of Materials*, 2013, **25**, 790-798.

93 K. Leng, Y. Sun, X. Li, S. Sun and W. Xu, *Crystal Growth & Design*, 2016, **16**, 1168-1171.

94 L. Bromberg, Y. Diao, H. Wu, S. A. Speakman and T. A. Hatton, *Chemistry of Materials*, 2012, **24**, 1664-1675.

95 P. B. S. Rallapalli, M. C. Raj, S. Senthilkumar, R. S. Somani and H. C. Bajaj, *Environmental Progress & Sustainable Energy*, 2016, **35**, 461-468.

96 Y. K. Hwang, D.-Y. Hong, J.-S. Chang, S. H. Jhung, Y.-K. Seo, J. Kim, A. Vimont, M. Daturi, C. Serre and G. Férey, *Angewandte Chemie International Edition*, 2008, **47**, 4144-4148.

97 L. A. Darunte, A. D. Oetomo, K. S. Walton, D. S. Sholl and C. W. Jones, *ACS Sustainable Chemistry & Engineering*, 2016, **4**, 5761-5768.

98 Z. Hu, M. Khurana, Y. H. Seah, M. Zhang, Z. Guo and D. Zhao, *Chemical Engineering Science*, 2015, **124**, 61-69.

99 D. M. Ruthven, S. Farooq and K. S. Knaebel, *Pressure Swing Adsorption*, Wiley-VCH, Weinheim, 1993.

100 N. T. T. Nguyen, H. Furukawa, F. Gándara, H. T. Nguyen, K. E. Cordova and O. M. Yaghi, *Angewandte Chemie International Edition*, 2014, **53**, 10645-10648.

101 S. Farooq and D. M. Ruthven, *AIChE Journal*, 1991, **37**, 299-301.

102 A. Malek and S. Farooq, *AIChE Journal*, 1997, **43**, 761-776.

103 Y. K. Kim, S.-m. Hyun, J. H. Lee, T. K. Kim, D. Moon and H. R. Moon, *Scientific Reports*, 2016, **6**, 19337.